

Low Voltage Electrowetting-on-Dielectric for Microfluidic Systems

A Dissertation
Presented to
the faculty of the School of Engineering and Applied Science
University of Virginia

In partial fulfillment
of the requirements for the degree
Doctor of Philosophy

By

Marcel Mibus

May, 2016

Approval Sheet

The dissertation
is submitted in partial fulfillment of the requirements for the degree of
Doctor of Philosophy

Marcel Mibus
AUTHOR

The dissertation has been read and proved by the examining committee:

Giovanni Zangari
Advisor

Robert Kelly
Chair

David Green

Michael L. Reed

Carl Knospe

Accepted for the School of Engineering and Applied Science



Craig H. Benson, Dean, School of Engineering and Applied Science

May, 201

Abstract

Manipulating fluids in micro to nano-liter volumes poses significant challenges, due to the dominance of surface forces with increasingly large surface to volume ratios. Commonly, external pumps or precisely micromachined on-chip pumps were used to generate pressure gradients to induce fluid motion. Alternatively, the wettability of a surface can be manipulated by an applied electric field. This phenomenon, known as electrowetting, consists in the spread of a liquid drop placed on an electrode upon application of a voltage. Electrowetting based devices flourished upon the discovery that an added dielectric layer between the drop and a conductive electrode would tolerate the application of large voltages, allowing for significant contact angle change. Several current commercial devices exploiting this effect include electro-optic displays, electronic paper, and variable focus lenses. Additionally, electrowetting has achieved particular prominence in lab-on-a-chip applications, controlling drop transport across patterned electrode structures.

Initially, polymers were utilized as the dielectric layer preventing current flow between the fluid and electrode, while providing a hydrophobic surface to minimize the resistance of drop movement. However, these layers were typically in excess of one micron thickness. As a consequence, these layers required over 100 Volts to achieve appreciable contact angle change. This dissertation aims to reduce the voltage dependence for contact angle change by optimization of a dual layer structure utilizing a dielectric and hydrophobic layer. The dielectric layer uses aluminum and tantalum oxides (15-44 nm thick) formed by electrochemical anodization. The electronic and ionic conduction, breakdown characteristics, and dielectric properties of these films were studied in detail, achieving a comprehensive understanding of the charge transport and failure mechanisms. Three hydrophobic layers were investigated: a commercial fluoropolymer Cytop, and two self-assembled monolayers (SAMs), phosphonic acid and silane. Each layer was seen to form reproducible surfaces, with high initial water contact angles and limited hysteresis, favoring contact line movement during electrowetting testing.

The electrowetting response of these bilayer structures was characterized by concurrently measuring contact angle and leakage current during stepped voltage measurements up to failure, showing three electrowetting response regimes: ideal Lippmann-Young behavior, contact angle saturation, and dielectric breakdown. The onset of ionic conduction in the metal oxide layer and the resulting breakdown determine when the layer would ultimately fail, but the thickness of the

hydrophobic layer determined the achievable contact angle vs. voltage characteristics. The study successfully showed ideally modeled electrowetting of greater than 25° under applied voltages of 12 V for Cytop, 6 V for phosphonic acid, and 5 V for silane. Cyclic wetting measurements using an “on” voltage above or below the voltage drop needed for polymer breakdown found that the decay rate of the contact angle decreases significantly over time only above this voltage threshold. The leakage current and charge injected in the polymer cannot comprehensively assess the stability of the system during operation. The contact potential difference measured with a Kelvin probe provides an alternative means to assess the extent of damage.

Acknowledgments

The research discussed within this dissertation was funded primarily by the NSF grant CMMI - 1030868. I would additionally like to gratefully acknowledge the Virginia Space Grant Consortium (VSGC) for support through their graduate fellowship and the University of Virginia engineering school for support through the John Bell McGaughy fellowship and several teaching assistant positions. I would like to thank my adviser, Giovanni Zangari, for helping me every step of the way during my time here and the regular council of Carl Knospe and Michael Reed, with weekly meetings to further the cause. None of this work would have been possible without their guidance and enthusiasm.

I would like to thank all of my friends I have made here during my 5 year adventure. The day to day interaction and nonsense help the long hours of grad school pass by. Specifically, Greg Pioszak, Brad Richards, and Amber Lass for the early years and getting through classes. Ryan Donahue and Zach Hoffman for general silliness. Also, I must recognize all the students that have helped me learn how to use new techniques and equipment; I would have been lost without you.

I also greatly appreciate my time at the University of Virginia and the city of Charlottesville. I have loved living here and will really miss it. Thanks to Dr. Gwathmey for giving me two new functional shoulders, hopefully I won't break myself again. Finally, I would be remiss if I did show my gratitude to the men's basketball team for countless hours of entertainment these last couple years. Thanks to Megan and Anne for going to all the basketball games that first year and Colin and Lucas for dragging me to volleyball games my last year. There are many more people that I have failed to mention, but your friendship was not overlooked.

Table of Contents

Abstract	1
Acknowledgments.....	3
List of Figures.....	6
Chapter 1 – Overview	11
Chapter 2 – Essential Background Theory	16
2.1 Wetting Basics.....	16
2.2 Electrowetting.....	17
2.3 Anodization of Valve Metals	22
2.4 Conduction Phenomena in Dielectrics	24
2.4.1 Electrode-Limited Conduction Processes	26
2.4.2 Bulk-Limited Conduction Processes	27
2.5 Breakdown.....	28
Chapter 3 – Experimental Methods.....	30
3.1 Anodization.....	30
3.2 Current – Voltage and Capacitance Measurements	31
3.3 X-ray Reflectivity (XRR)	32
3.4 Scanning Kelvin Probe	35
3.5 Static Contact Angle.....	36
3.6 Dynamic Contact Angle	37
3.7 Scanning Electron Microscopy and Energy Dispersive X-ray spectroscopy	39
3.8 Atomic Force microscopy.....	40
3.9 Mott-Schottky	41
Chapter 4 – Dielectric Oxide Properties	43
4.1 Aluminum Oxide.....	43
4.1.1 Oxide Growth	43
4.1.2 Metal-Oxide-Metal Contacts	44
4.1.3 Electronic conduction processes in MOM contacts.....	47
4.1.4 Mott-Schottky Analysis	49
4.1.5 Electrolyte-Oxide-Metal Contacts	50
4.2 Tantalum Oxide.....	55

4.2.1 Oxide Growth	55
4.2.2 Metal-Oxide-Metal Contacts	57
4.2.3 Electronic Processes	59
4.2.4 Mott-Schottky Analysis	60
4.2.5 Electrolyte-Oxide-Metal Contacts	61
4.3 Dielectric Constant Determination	63
4.4 Conclusions	64
Chapter 5 – Hydrophobic Layer Formation.....	66
5.1 Overview	66
5.2 Cytop.....	69
5.2.1 Synthesis	69
5.2.2 Contact Angle.....	70
5.2.3 Contact Angle Hysteresis.....	70
5.3 Self-Assembled Monolayers.....	71
5.3.1 Phosphonic acid SAMs	72
5.3.2 Silane SAMs	80
5.4 Conclusions	87
Chapter 6 – Electrowetting	88
6.1 Aluminum Oxide + Cytop.....	88
6.1.1 Static Electrowetting.....	88
6.1.2 Cyclic Electrowetting.....	97
6.1.3 Scanning Kelvin Probe.....	103
6.2 Tantalum Oxide + Cytop.....	106
6.2.1 Static Electrowetting.....	106
6.2.2 Cyclic Electrowetting.....	109
6.3 Oxides + ODPA	117
6.3.1 Static Electrowetting.....	117
6.3.2 Cyclic Electrowetting.....	120
6.4 Tantalum Oxide + Silane	121
6.4.1 Static Electrowetting.....	121
6.4.2 Cyclic Electrowetting.....	123
6.5 Dynamic Electrowetting.....	127
Chapter 7 – Conclusions and Future Work	130

7.1 Conclusions	130
7.2 Suggestions for Future Work.....	132
References.....	136

List of Figures

Figure 1: Minimum voltage and dielectric layer thickness requirements for 30o of EWOD operation for 1MV/cm – ϵ_r -2.1 (solid) and 3MV/cm – ϵ_r -7 (dotted)	13
Figure 2: Dielectric constant and bandgap for various oxides. Image reproduced from Ref. [23].....	14
Figure 3: (a) basic EWOD schematic showing the change in contact angle with applied voltage (b) a close up view of the contact line showing the actual deformation of the drop with electric field.	20
Figure 4: Close up of contact line with dielectric thicknesses of (a) 10 μm , (b) 50 μm , and (c) 150 μm . The white bars show the characteristics thickness (d/ϵ_{diel}). Image reproduced from [40].....	21
Figure 5: Schematic of the high-field model (a) the adjacent lattice planes in the oxide (b) the effect of electric field on activation energy (W). Images from Ref. [45].....	23
Figure 6: Schematic of a p-i-n structure in as-grown anodic Al_2O_3 for (a) thin films and (b) thick films. Image from Ref. [56]	24
Figure 7: Energy diagram of an insulator (a) crystalline (b) amorphous. Image from Ref. [60]	25
Figure 8: Overview of possible conduction mechanisms in metal-insulator-metal systems. Image from Ref. [61]	26
Figure 9: (a) Anodization Setup with using an aluminum bar and a platinum counter-electrode (b) current density vs. time for aluminum oxide anodization at 20 V.....	31
Figure 10: Set up for I-V and C-V measurements	32
Figure 11: Basic XRR measurement beam alignment	33
Figure 12: (a) XRR data for tantalum (purple) and tantalum oxide (gold) layers, with XRR features highlighted in the plot and (b) Kiessig fringes.....	34
Figure 13: Schematic of SKP operation (a)-(c) process of measuring the contact potential difference between two metals and (d) the actual measurement configuration used.	36
Figure 14: (a) Static EWOD measurement system (b) DROPIImage Standard Software for contact angle determination	37
Figure 15: (a) schematic of a hydrophobic coated substrate being dipped into a liquid bath showing advancing and receding contact angles. (b) Corresponding force-immersion depth data for the process in (a). Data from a 21 nm Cytop surface (from Chapter 5)	39
Figure 16: Schematic of AFM operation. Image from Ref [80].....	40

Figure 17: Thickness of anodized aluminum oxide films vs. anodization voltage. Thickness measurements by ellipsometry are in close agreement with calculations from the charge density.....44

Figure 18: (a) I-V characteristics for aluminum oxide films of various thickness in a metal-oxide-metal configuration operating under both polarities (b) Breakdown voltage V_B and breakdown field E_B vs. film thickness for positive (black, square) or negative (red, triangle) polarity applied to the top contact. The error bars represent max and min values for the data scatter with the average value as the data point.....46

Figure 19: (a) Fit of the experimental I-V characteristics of a 56 nm thick Al oxide film to a combination of dielectric leakage mechanisms; each process in turn is assumed to dominate conduction in the voltage region where the corresponding characteristics applies: Schottky Emission (Red), Poole-Frenkel (Blue), Fowler-Nordheim (Orange).(b) I-V characteristics of a 32nm thick oxide layer; a good fit could be obtained by assuming only SE and FN conduction mechanisms. (c) Schematic for the MOM electronic conduction mechanisms.....48

Figure 20: (a) Mott-Schottky plots of as-anodized aluminum oxide films at 32 nm and 44 nm. (b) Dopant density as a function of thickness50

Figure 21: The characteristic I-V curves for Al_2O_3 layers of different thickness. Polarity refers to the voltage being applied to the .05M Na_2SO_4 electrolyte drop, with the ground being the base aluminum layer.51

Figure 22: (a) Typical I-V characteristics from a negatively biased EOM contact consisting of a 56nm of oxide and a .05M Na_2SO_4 droplet as the top contact. The dielectric current leakage models are fitted to the data using Equations 2 and 4 (b) two regions of the negative polarity curve are identified where the electronic and ionic current dominate, respectively; the transition corresponds roughly to at the anodization voltage (c) schematic of the oxide/electrolyte interface for the negatively biased system.53

Figure 23: Three consecutive I-V characteristics recorded at a 38nm thick oxide surface using the same .05M Na_2SO_4 droplet for all curves. The curves were run (black to red to blue) immediately following one another without altering the configuration. Oxide thickening is observed between 1 and 2, breakdown between 2 and 3.....54

Figure 24: (a) XRR scans of tantalum oxide films ranging from the unanodized substrate to anodization at 60 V with (b) the resulting thickness calculated from (a).....56

Figure 25: (a) I-V characteristics for tantalum oxide films of various thickness in a metal-oxide-metal configuration operating under both polarities (b) Breakdown voltage V_B and breakdown field E_B vs. film thickness for positive (black, square) and negative (red, triangle) polarity applied to the top contact. The error bars represent max and min values for the data scatter with the average value as the data point.....58

Figure 26: Fit of the experimental I-V characteristics of a 42 nm thick Ta oxide film to a combination of dielectric leakage mechanisms; each process in turn is assumed to dominate conduction in the voltage region where the corresponding characteristics applies: Schottky Emission (Red), Poole-Frenkel (Blue).....60

Figure 27: (a) Mott-Schottky plot of 64 nm tantalum oxide (b) summary of donor densities for 34, 49, and 64 nm oxides.....	61
Figure 28: The characteristic I-V curves for tantalum oxide layers of different thickness. Polarity refers to the voltage being applied to the .05M Na ₂ SO ₄ electrolyte drop, with the ground being the base tantalum.....	62
Figure 29 : Comparison of EOM I-V characteristics for tantalum and aluminum oxide under anodic polarization.	63
Figure 30: Dielectric Constant of aluminum and tantalum oxide films anodized at 30 V reaching a thickness of 44 and 46 nm, respectively.	64
Figure 31: Summary of hydrophobic layer formation.....	67
Figure 32: Simulated Lippmann-Young relationship using different thickness combinations of aluminum oxide and hydrophobic materials.....	68
Figure 33: Thin film Cytop layers showing (a) tearing on aluminum oxide and (b) tearing on gold with electrodeposited copper on the bare gold substrate	70
Figure 34: Force-depth curves of 20 nm Cytop film.....	71
Figure 35: Contact angle vs. Immersion time for 1mM ODPA SAMs formed in Toluene at room temperature (black), 45°C (red), and 65°C (green)	73
Figure 36: Sketch of SAM formation process progressing from a disordered “lying down” phase to Image reproduced from Ref. [119].....	74
Figure 37: Low voltage SEM of oxide-SAM surface using 1mM ODPA in toluene at 45°C immersed for (a) 60 hours and (b) 40 hours. Dark regions show high C and P EDS signals	75
Figure 38:(a) XRR patters for aluminum oxide and various SAM immersion times, as indicated in plot. (b) zoomed in region from (a).	76
Figure 39: Dynamic contact angle measurements on 1mM ODPA in toluene at 45°C surfaces at various immersion times. (a)-(b) raw force-depth data and (c) calculated CAH values across immersion times.....	79
Figure 40: Temperature vs. alkyl chain length for molecular conformations in final monolayer [143]. Image from Ref. [141].	81
Figure 41: AFM image of (a) 44 nm tantalum oxide substrate and (b) 5 min immersion of 2 (v/v) OTS in toluene on 44 nm tantalum oxide.....	82
Figure 42: (a) AFM image and (b) SEM image of 60 min immersion of 2 (v/v) OTS in toluene on 44 nm tantalum oxide	83
Figure 43: (a) and (b) SEM images at different magnifications and (c) AFM image of 120 min immersion of 2 (v/v) OTS in toluene on 44 nm tantalum oxide	84
Figure 44:(a) XRR patters for tantalum oxide and various silane SAM immersion times, as indicated in plot. (b) zoomed in region from (a).	85

Figure 45: Force-depth measurements on silane surfaces at various immersion times (a) in lab air (b) under inert atmosphere immersed for 30 min, (c) 60 min, and (d) 120 min. Contact angle hysteresis values given in plot (red).....	87
Figure 46: Electrowetting and leakage current measurements on bilayers of ~22nm Cytop + Aluminum Oxide with thicknesses (a) 15nm (b) 32nm (c) 44nm. Contact angle data in black (left axis) with Eq. 6 modeled (black line) and measured current density in blue (right axis)	91
Figure 47: SEM image of Aluminum Oxide – Cytop layer showing the detachment of the fluoropolymer indicated by wetting out in the drop image inset. EDS map of Fluorine signal given in yellow.	95
Figure 48: Electrowetting and leakage current measurements on bilayers of Aluminum Oxide - Cytop of (a) 43nm and (b) 210nm. Contact angle data in black (left axis) with EQ.1 modeled (black line) and measured current density in blue (right axis).....	97
Figure 49: Contact angle vs. Cycle number are shown for cyclic measurements of (a) 32nm aluminum oxide – 21nm Cytop and (b) 44nm aluminum oxide – 22nm Cytop bilayers until no wetting was observed	99
Figure 50: Contact angle vs. Cycle number cyclic measurements are shown on 44nm aluminum oxide /210nm cytop bilayer with applied voltages of (a) $V_{on} = 20\text{ V}$ and (b) $V_{on} = 25\text{ V}$	101
Figure 51: (a) Current-time transient for cycles 125 to 130 from the Fig. 5 contact angle measurements with (a) $V_{on} = 20\text{ V}$ and (b) $V_{on} = 25\text{ V}$ on 44nm aluminum oxide/210nm Cytop bilayer.....	103
Figure 52: Contact potential difference maps of 44 nm Al_2O_3 – 20 nm Cytop surfaces total cycle, numbers indicated in the figure. Colors correspond to mV in legend.....	104
Figure 53: Contact potential difference map of 44 nm Al_2O_3 – 210 nm Cytop surface with cycle applied voltage values for cyclic spots, numbers indicated in the figure.	105
Figure 54: Theoretical contact angle vs. voltage Lippmann-Young curves for 21 nm Cytop + 32 nm Ta_2O_5 (black) and Al_2O_3 (red)	107
Figure 55: Electrowetting and leakage current measurements on bilayers of ~22nm Cytop + tantalum oxide with thicknesses (a) 32nm and (b) 44nm. Contact angle data in black (left axis) with Eq. 6 modeled (black line) and measured current density in blue (right axis)	108
Figure 56: Contact angle vs. Cycle number are shown for cyclic measurements of (a) 32nm tantalum oxide – 21nm Cytop and (b) 44nm tantalum oxide – 22nm Cytop bilayers until no wetting was observed	110
Figure 57: Contact potential difference maps of 44 nm Ta_2O_5 – 21 nm Cytop surfaces, total cycle numbers indicated in the figure. Colors correspond to mV in legend.....	111
Figure 58: Contact potential difference map of 44 nm Ta_2O_5 surfaces, total cycle numbers indicated in the figure. (a) & (b) are the same surface at different scales, in mV indicated by the legend	113
Figure 59: Contact angle vs. Cycle number cyclic measurements are shown on 44nm tantalum oxide /210nm cytop bilayer with applied voltages of (a) $V_{on} = 20\text{ V}$ and (b) $V_{on} = 25\text{ V}$	115

Figure 60: Contact potential difference maps of 44 nm Ta₂O₅ – 21 nm Cytop surfaces total cycle, numbers indicated in the figure. Colors correspond to mV in legend..... 116

Figure 61: Electrowetting and leakage current measurements of ODPA (formation times in plot) + 44nm aluminum oxide. Contact angle data in black (left axis) with Eq. 6 modeled (black line) and measured current density in blue (right axis) 118

Figure 62: Electrowetting and leakage current measurements of ODPA (formation times in plot) + 44nm tantalum oxide. Contact angle data in black (left axis) with Eq. 6 modeled (black line) and measured current density in blue (right axis) 119

Figure 63: Contact angle vs. Cycle number are shown for cyclic measurements of 44nm tantalum oxide with ODPA monolayer immersed for 32hr in 45°C toluene..... 121

Figure 64: Electrowetting and leakage current measurements of Silane SAMs (formation times in plot) + 44nm tantalum oxide. Contact angle data in black (left axis) with Eq. 6 modeled (black line) and measured current density in blue (right axis)..... 123

Figure 65: Contact angle vs. Cycle number are shown for cyclic measurements of 32nm and 44nm tantalum oxide with 30 min formation of Silane SAMs 2% (v/v) in toluene under Ar..... 124

Figure 66: Contact potential difference maps of (a) 32 nm and (b) 44 nm Ta₂O₅ + 30min formation of Silane SAMs 2% (v/v) in toluene under Ar. Total cycle numbers indicated in the figure. Colors correspond to mV in legend..... 125

Figure 67: Dynamic EWOD 129

Figure 68: (a) Current Density vs. time for stepped electrowetting measurements on 44 nm aluminum oxide + 56 nm Cytop, (b) current – time data plotted on log-log scale with beta indicating the slope of each voltage step, and (c) the power law exponent at each voltage step, with an exponential fit in red..... 134

Figure 69: (a) power law exponent for V_{on} = 20 V and (b) power law exponent for V_{on} = 25 V for 44nm aluminum oxide + 210nm cytop bilayer. 135

Chapter 1

Overview

Handling and manipulation of fluids in the micro to nano-liter scale poses significant challenges as fundamental fluidic physics drastically change at such scales, due to surface tension and viscosity becoming dominant over inertial forces. Microelectromechanical systems (MEMS), have been utilized in many ways to actuate microfluidic systems [1], aiming for devices to run automated chemical and biological measurements [2]. Experimental systems used pumps to generate pressure gradients and enable fluid transport, but initially the pumps were outside the chip structure limiting device mobility and practical application [3]. In self-contained on-chip systems, mechanical pumps relying on precisely micromachined components were utilized, but were limited by the high cost and limited reliability of the actuation mechanism [4]. Alternatively, surface tension was considered as an attractive method to control microfluidic transport [5], due to dominance of surface effects with increasingly large surface to volume ratio [2]. Manipulation of surface wettability can be achieved through thermal control (thermocapillarity) or electrical control (electrocapillarity), with electrical control considered more promising due to higher efficiencies combined with avoidance of fluid heating [6]. The electrocapillary effect of a drop on an electrode surface is known as electrowetting. This phenomenon consists in enhancing the wettability of the surface by an applied electric field. Initially the efficacy of electrowetting was used on metals with limited success, as only small contact angle change would occur prior to electrolysis of aqueous solutions. In 1993, Berge discovered that utilizing a thin insulating layer between the electrode and electrolyte allows for large scale reversible contact angle change, thus creating electrowetting-on-dielectric, or EWOD [7]. The ability to provide reversible and precise control of the contact angle created the opportunity for many new applications based on this effect, significantly growing the field from the less than five publications appearing per year prior to 2000 [8]. Commercial devices based on EWOD are currently available in electro-optic displays (Liquidvista Co.) [9], variable focus lenses (Varioptic Co.) [10], electronic paper (Plastic Logic Co.) [11], and various lab-on-a-chip applications [12].

In order to achieve proper EWOD function, the dielectric layer must be insulating, possess an appreciable dielectric strength, and exhibit initial water contact angles in excess of 100° . The Lippmann-Young theory (Chapter 2, Eq. 6) provides an equation to predict the contact angle change

with applied voltage, which is dependent on the capacitance of the dielectric layer. Therefore, as the dielectric layer thickness decreases so does the voltage needed to achieve a given contact angle change. In actuality the breakdown characteristics of the layer must also be considered. The maximum functional voltage at a given thickness is related to the breakdown field, which introduces a fundamental limitation on the thickness of the dielectric layer. The interplay of dielectric constant, thickness, and breakdown strength is highlighted in Figure 1. Data for a commonly used EWOD hydrophobic commercial polymer, Cytop, are shown with solid lines, the linear dependent breakdown field strength in red and the square root voltage needed for 30° of contact angle change in black (calculated via the Lippmann-Young expression, Chapter 2, Eq. 6). A contact angle change of 30° is typically the maximum achievable for systems in air in current EWOD operation [13], as will be clarified in Chapter 6. The operational limitation of the polymer to achieve this contact angle change is given by the intercept of the breakdown field (red) with the required contact angle change voltage in black, at 40 V. If a lower voltage is applied than this operational limit, either the change in contact angle must be less than 30° or the dielectric layer will undergo breakdown, highlighted in grey. The polymer has a low breakdown field (1MV/cm), requiring an excess of 400 nm to achieve the contact angle change without failure. The minimum operation voltage can be decreased by selecting a higher breakdown field strength and/or a greater dielectric constant material, demonstrated in Figure 1 with the dotted curves, using a threefold increase in both properties. If both material properties are increased three times, the combined improvements decrease the operating voltage to only 6 V, requiring a 20 nm thick dielectric layer.

The overarching objective of this dissertation is to design high performance and reliable material systems for electrowetting at low voltages. Lower voltage operation is especially important for mobile applications where batteries are the likely power source, such as displays or lab-on-chip systems. The target is to achieve approximately 30° of contact angle change under 15 V, reliably. The surface must be hydrophobic, with contact angles greater than 100°, as electrowetting can only lower the contact angle. Additionally, the surface must have low contact angle hysteresis, defined as the difference between advancing and receding contact angles, when the three phase contact line moves. These constraints lead to the widespread use of hydrophobic fluoropolymers as the single dielectric layer; these materials include mainly commercially available and easily fabricated materials, such as Teflon [14], Cytop [15], and FluoroPel [16]. However, using the analysis in Figure 1, in order to decrease the operation voltage from using at least 40 V with a 400 nm dielectric layer, an additional layer is required, since various hydrophobic polymers have similar breakdown field and dielectric

constant values, limiting the parameter space. Therefore, in this study the dielectric layer and hydrophobic layer are broken into two different categories in order to optimize different properties separately. Polymer-dielectric bilayer systems studied so far include the above hydrophobic polymers, combined with oxides such as SiO_2 [13], [17], Al_2O_3 [18], [19], Ta_2O_5 [20], [21] as the high dielectric strength layer. Commonly these investigations are limited to evaluation of contact angle vs. voltage response for the electrowetting region modeled by the Lippmann-Young relationship. The bilayer systems in this work will be investigated throughout the complete EWOD response until failure through static, dynamic, and cyclic measurement. In addition, electrowetting performance will be related to the processes occurring in the dielectric layer.

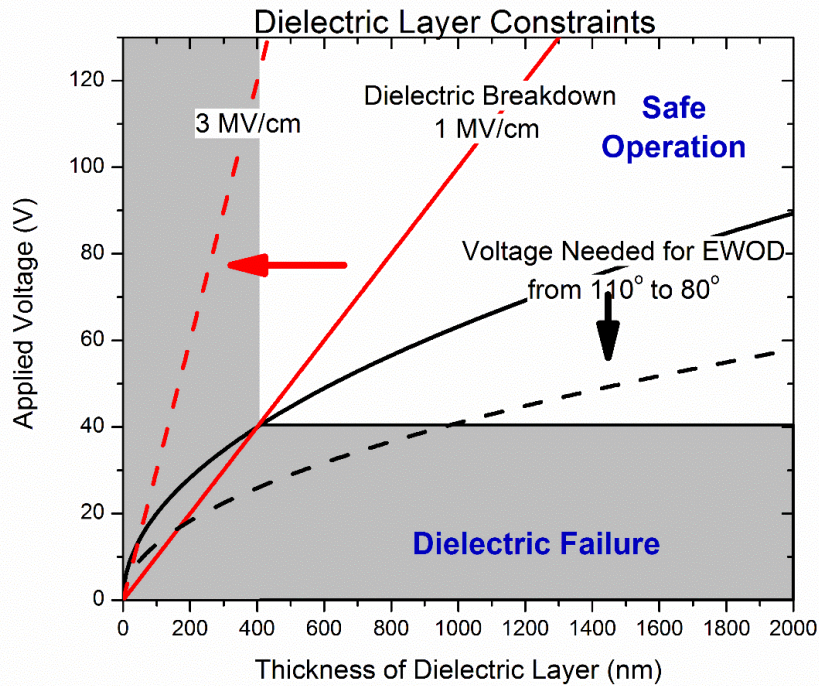


Figure 1: Minimum voltage and dielectric layer thickness requirements for 30o of EWOD operation for 1MV/cm – $\epsilon_r=2.1$ (solid) and 3MV/cm – $\epsilon_r=7$ (dotted)

The primary driver for minimizing the voltage dependence on the contact angle is to use a high dielectric constant material as the primary dielectric layer. The requirement of the dielectric material is analogous to the current replacement of SiO_2 as gate oxides in CMOS, following similar constraints. The dielectric must act as an insulator, especially in conjunction with aqueous electrolytes

when the applied voltages used exceed the potential window of electrochemical water stability. Therefore, large bandgap film materials are desirable, with a sufficient thickness to avoid tunneling. Additionally, the layer would ideally present limited electronic defects, as trap-assisted conduction occurs until a critical percolation path ultimately leads to failure of the dielectric [22]. Figure 2 shows common dielectric materials for candidate gate oxides in CMOS highlighting the tradeoff between the dielectric constant and bandgap [23]. The dielectrics chosen for this study are Al_2O_3 and Ta_2O_5 , which meet the outlined requirements and lab fabrication constraints.

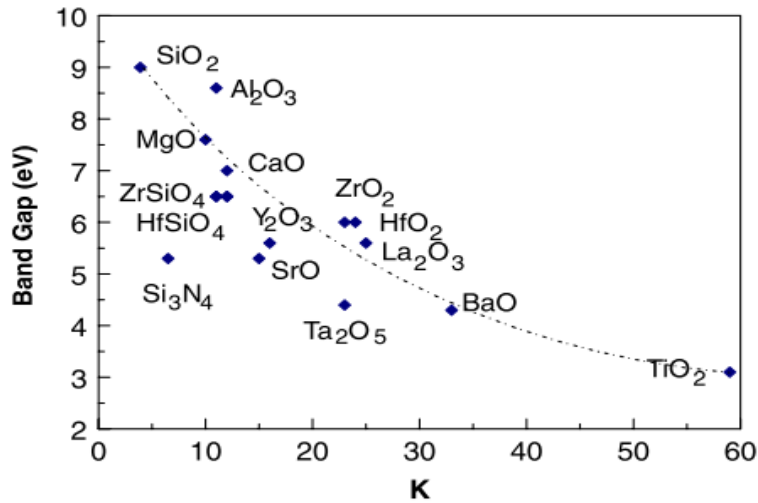


Figure 2: Dielectric constant and bandgap for various oxides. Image reproduced from Ref. [23]

The hydrophobic layer is evaluated as the second component of the dielectric stack. Three different hydrophobic materials will be studied to provide high initial contact angles with minimal resistance of the three phase contact line motion. A commercial fluoropolymer Cytop, which has been commonly used in the electrowetting literature, is employed. The polymer can be reliably synthesized only for thicknesses larger than 20 nm; the thickness of the hydrophobic layer could be reduced only using self-assembled monolayers.. Phosphonic acid and silane self-assembled monolayers are studied in various solution formation conditions to provide a continuous and stable surface.

Within the general objective of this dissertation for low voltage EWOD, the following scientific questions are examined. (1) Can anodic oxides serve as high-k dielectrics in electrowetting systems, (2) can self-assembled monolayers reliably function as the hydrophobic layer, and (3) how do the bilayer systems fail. Additionally, it is my hope that this work would establish a framework for better understanding of electrowetting systems, enhancing the properties for successful structures.

The dissertation is broken down in the following structure, understanding in turn the properties of each individual layer in the EWOD system. Chapter 2 provides the essential background theory behind wetting and anodic oxide formation. Chapter 3 discusses the experimental techniques used to characterize and evaluate the various oxides and hydrophobic materials. Chapter 4 investigates the formation and properties of the anodically grown aluminum and tantalum oxide. Chapter 5 covers the formation of the hydrophobic layer as the second component of the dielectric stack. Chapter 6 discusses the electrowetting performance of the combination of oxide and hydrophobic layer characterized in the previous chapters. Chapter 7 highlights several open questions with future work and includes the conclusions of the dissertation.

Chapter 2

Essential Background Theory

Part of this chapter is reproduced from:

M. Mibus, X. Hu, C. Knospe, M. L. Reed, and G. Zangari, “Anodic Metal Oxides for Electrowetting Systems,” *Curr. Nanosci.*, vol. 11, no. 3, pp. 333–342, 2015.

This chapter highlights the theoretical background to many of the topics covered throughout the dissertation. Specifically, the concept of wetting and its extension to electrowetting are discussed, and the formation of anodic oxides and their properties are covered.

2.1 Wetting Basics

The theoretical aspects of wetting discussed here are limited to the electrowetting theory without discussing the complexity of this rich and fascinating field; for a more complete overview see the seminal work by de Gennes [24] or the equally excellent modern review by Bonn [25]. Additionally, gravity is always neglected in the discussion. The Bond number in fact, a unitless number measuring the importance of surface tension (γ) relative to gravity (g) ($Bo = \Delta\rho R^2 g / \gamma_{lg}$) with R as the length and ρ the difference in density between phases, ranges for the volumes of the fluids examined in this dissertation between 0.5 to 1, indicating that surface tension is dominant [8]. First we consider the placement of a liquid drop on a solid surface. Prior to touching the surface, the drop assumes a spherical shape as a result of intermolecular forces. The molecules in the liquid bulk are attracted equally in all directions, creating no net force. However, the molecules at the surface witness an inward force toward the liquid as the liquid – liquid cohesive force is significantly stronger than the air – liquid adhesive forces [26]. This attraction generates the surface tension, defined as the amount of energy needed to enlarge the surface area by one surface unit. Water is the primary fluid used throughout the dissertation, with a surface tension of 72 mJ/m^2 between water and air. The surface tension for water is very large among fluids due to the permanent dipole of water molecules. To provide a context, the surface tension of the majority of other room temperature fluids, particularly organics, commonly range between $30 - 50 \text{ mJ/m}^2$, while liquid metals such as Mercury reach 485 mJ/m^2 .

The surface tension creates a net force acting to compress the drop, which is balanced at equilibrium by the internal pressure of the drop. Laplace in 1805 found that the increase in pressure

across the boundary of two fluids is given by the mean surface curvature times the surface tension (γ), defined for liquid-vapor in Eq. 1 [27],

$$\Delta P = 2\gamma_{LG}\kappa = \gamma_{LG} \left(\frac{1}{R_1} + \frac{1}{R_2} \right) \quad \text{Eq. 1}$$

with κ as the mean curvature and R_1 and R_2 as the principal radii of curvature. Placing the drop on a solid surface causes three interfacial tensions to be active: solid-liquid, liquid-gas, and solid-gas. Young's equation [28] gives an equilibrium force balance of the three phase contact line in Eq. 2.

$$\gamma_{SG} = \gamma_{SL} + \gamma_{LG} \cos(\theta_{eq}) \quad \text{Eq. 2}$$

The equilibrium contact angle (θ_{eq}) quantifies the amount of wetting at the surface; this may range from complete wetting ($\theta_{eq} = 0^\circ$) to no wetting ($\theta_{eq} = 180^\circ$), with partially wetting referring to the configurations ($0^\circ < \theta_{eq} < 180^\circ$). The shape of the drop must still follow the Laplace equation, thus the drop sits as a spherical cap on the surface. Using the relationships from Eq. 1 and Eq. 2 provides the starting point for the analysis of electrowetting systems, i.e., the sessile drop on the surface.

The materials used throughout this dissertation are primarily bilayers, one providing the necessary dielectric properties and the other generating hydrophobicity. The anodic oxides (Chapter 4) are partially wetting with contact angles typically between 30-40°, which is the primary reason a hydrophobic layer (Chapter 5) is added, with initial angles near 110°.

2.2 Electrowetting

The alteration of the equilibrium angle of a sessile drop (Eq. 2) by an electric field was originally observed by Gabriel Lippmann and codified in the classical derivation of the electrocapillarity equation [29], using Gibbsian interfacial thermodynamics. Lippmann demonstrated field- induced charge accumulation in the metal at an electrolyte-mercury interface with a distribution of opposite charge ions at the liquid interface causing a reduction in the effective interfacial surface tension. The differential relationship between surface tension (γ), voltage (V), and charge density (ρ) is given by Eq. 3 at a constant chemical potential (μ):

$$\rho = -\left.\frac{\partial\gamma}{\partial V}\right|_{\mu} \quad \text{Eq. 3}$$

The voltage dependence of the surface tension is found by integrating Eq. 3, but this requires knowledge of the relationship for the voltage dependent ion distribution in the liquid. The ion distribution at the charged interface is known as the electrical double layer, which is comprehensively modeled by considering the ions at the interface and a diffuse component dependent on applied potential and ion concentration. The simplest description of the ion-electrode interface uses a constant Helmholtz layer [30], where the ions are placed at a fixed distance (\sim nm) from the surface, which is simply integrated to obtain Eq. 4 [31]. The integration starts from the electrode potential at the point of zero charge (V_{PZC}) rather than zero, since the electrode has a spontaneous charge layer. V_{PZC} describes the voltage required to compensate for this spontaneous charging.

$$\gamma_{SL}(V) = \gamma_{SL}^0 - \int_{V_{PZC}}^V \rho_{SL} dV = \gamma_{SL}^0 - \frac{\epsilon_0 \epsilon_H}{2d_H} (V - V_{PZC})^2 \quad \text{Eq. 4}$$

with ϵ_H the liquid dielectric constant, ϵ_0 the free space permittivity, d_H the layer thickness, combining to give the Helmholtz capacitance. No applied voltage dependence is assumed for γ_{LG} , allowing for the voltage dependence in Eq. 4 combined with Young's relationship (Eq. 2) to describe the contact angle change for an electrolyte on an electrode surface,

$$\cos(\theta) = \cos(\theta_{eq}) + \frac{\epsilon_0 \epsilon_H (V - V_{PZC})^2}{2 d_H \gamma_{LG}} \quad \text{Eq. 5}$$

with θ being the *apparent* contact angle, a distinction that will be elaborated on further in subsequent sections. Suppose that a drop of a typical dilute salt electrolyte NaCl is placed on an electrode. The values of the constants in Eq. 5 become $d_H = 0.4$ nm, $\epsilon_H = 78.5$, $\gamma_{LV} = 72$ mN/m [32], giving $\cos(\theta) = \cos(\theta_{eq}) + 12 * V^2$, a massive change. Even with the simple ion distribution assumed for the analysis, the results demonstrate the strong influence of the electric field on contact angle changes. However, in this hypothetical system, the maximum achievable change is limited by the potential window stability of the aqueous fluid, with electrolysis occurring ideally at 1.23V.

In 1993, Berge discovered that the previous response of an electrolyte to an applied voltage operates similarly on an insulating surface covering a conductor [7]. Introducing a dielectric layer over

the electrode creates two capacitors in series, the insulating layer and the Helmholtz layer, but the Helmholtz capacitance is several orders of magnitude larger (due to the much lower thickness), leading to the total capacitance being generated by the dielectric layer. Another common simplifying assumption is that the dielectric does not give rise to significant charge in absence of applied voltage, leading to $V_{pzc} = 0$ [8]. Combining these simplifying assumptions results in the commonly presented electrowetting-on-dielectric (EWOD) relationship given in Eq. 6,

$$\cos(\theta) = \cos(\theta_{eq}) + \frac{1}{2\gamma_{LG}} \frac{\epsilon_{diel}\epsilon_0}{d_{diel}} V^2 \quad \text{Eq. 6}$$

now using ϵ_{diel} and d_{diel} as dielectric constant and thickness of the insulator, respectively. The second term on the RHS of the equation is commonly referred to as the electrowetting number ($\epsilon_{diel}\epsilon_0 V^2 / (2d_{diel}\gamma_{LG})$) [8], a ratio of electrostatic energy to surface tension, which describes how effective the applied voltage will be in deforming the drop. Using a layer of Teflon, a commercial fluoropolymer, $\epsilon_{diel} = 2$ and $d = 500\text{nm}$, gives $2.5 \times 10^{-4}/V^2$ as the electrowetting number, several orders of magnitude lower than what was observed in the electrode-electrolyte system, using Eq. 5. A schematic representation of EWOD is shown in Figure 3(a) for a partially wetting electrolyte on a hydrophobic surface. Equation Eq. 6 works very well for predicting the macroscopic change of apparent contact angle and has been experimentally verified over a wide range of systems and material configurations. The above derivation is referred to as the ‘electro-chemical’ interpretation of electrowetting; this makes sense from an intuitive standpoint, but doesn’t provide a physical picture of how the reduction in contact angle is achieved in mechanical terms.

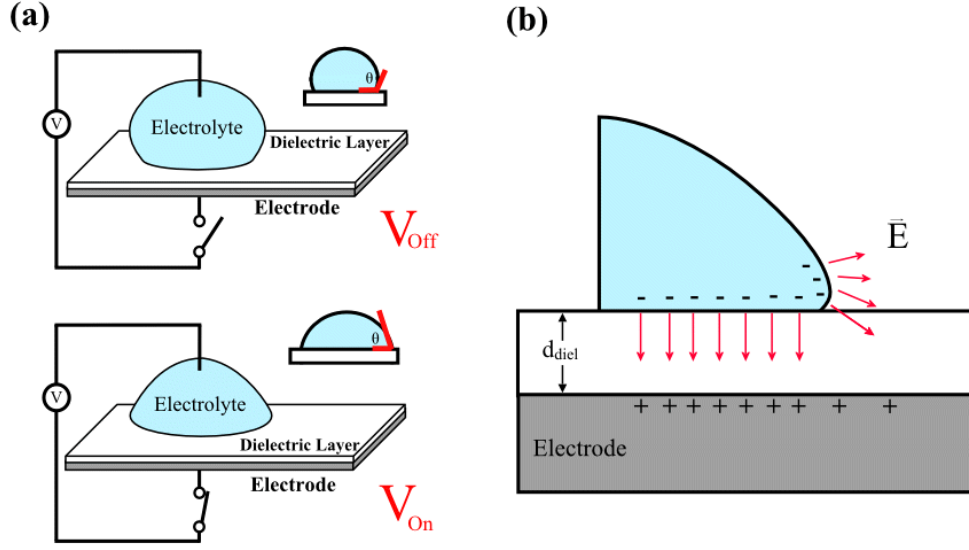


Figure 3: (a) basic EWOD schematic showing the change in contact angle with applied voltage (b) a close up view of the contact line showing the actual deformation of the drop with electric field.

A more detailed description of the contact line has been developed [33]–[38] through analysis of an electro-mechanical force balance at the drop surface, originally introduced by Jones et. al. [38]. Considering only the forces on the liquid, the analysis determines that the changing drop profile changes while without considering any voltage dependent interfacial tension. The detailed formulation is reviewed in [8]. The analysis assumes that the liquid surface possesses a net charge, which causes a downward (electrostatic) force along the liquid-solid interface when a voltage is applied. However, at the edge of the drop an electric fringe field creates a Maxwell stress, generating a net force outward of the surface normal, schematically shown in Figure 3(b). The net force is found by integration of the Maxwell stress tensor over a liquid volume element. As a result, the only contribution that doesn't cancel out is directed upon the surface normal, which is given by the Maxwell stress Π_{el} in Eq. 7,

$$\Pi_{el} = \frac{\epsilon_0}{2} \vec{E}(\vec{r})^2 \quad \text{Eq. 7}$$

where $\vec{r}(\text{arrow})$ is the surface normal. In order to balance the stress, the drop must deform consistently with the Laplace pressure (Eq. 1) everywhere along the surface, thus $\Pi_{el} = \Delta P_L$. Vallet et. al.,

demonstrated that the electric field diverges around the contact line, with the Maxwell stress decaying to negligible values at the length scale of the dielectric layer thickness from the contact line [39]. As a result, the net local force on the drop can be found by integrating the horizontal component of the Maxwell stress resulting in the simple expression given by half the dielectric capacitance times the voltage squared, Eq. 8.

$$F_x = \frac{\epsilon_{diel}\epsilon_0}{2d_{diel}} V^2 \quad \text{Eq. 8}$$

The primary consequence of the previous analysis is that the local contact angle does not actually change, rather we macroscopically observe a change in an *apparent* contact angle. The difference can be experimentally visualized using a characteristic length d/ϵ_{diel} from the contact line [40]. Figure 4, shows the difference between the local and apparent contact angle at dielectric length scales from 10 to 150 μm , with the white bar giving the characteristic length. However, this relationship breaks down when the thickness of the dielectric exceeds the drop size, making local and apparent angles equal [41].

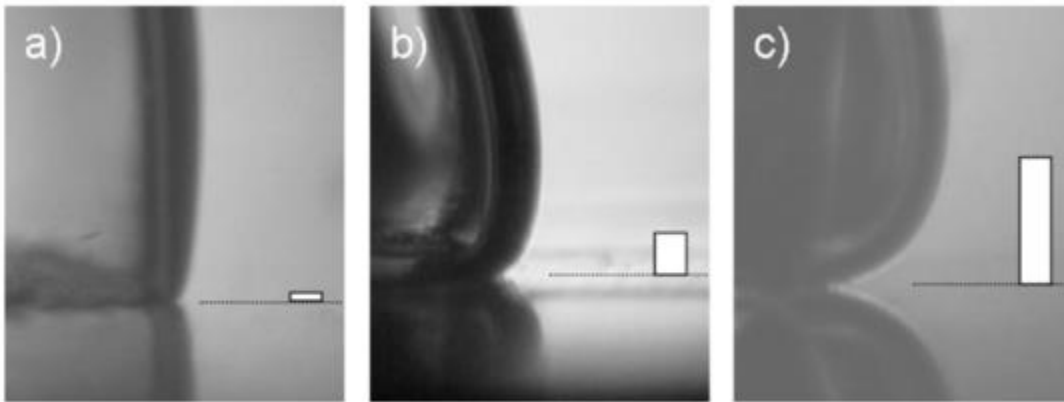
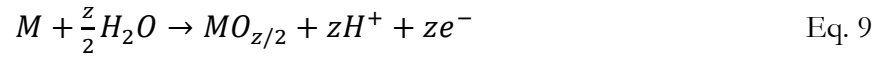


Figure 4: Close up of contact line with dielectric thicknesses of (a) 10 μm , (b) 50 μm , and (c) 150 μm . The white bars show the characteristics thickness (d/ϵ_{diel}). Image reproduced from [40].

The majority of the work in this dissertation uses bilayers consisting of a valve metal oxide and a fluoropolymer. The oxide layers were formed by an electrochemical anodization method, i.e., by applying an anodic potential to a precursor metal layer. The theory of oxide formation as well as the key solid-state leakage current mechanisms are discussed in the following.

2.3 Anodization of Valve Metals

Valve metals have a strong tendency to readily form a surface oxide in air or an aqueous solution. The term valve metals comes from the observation that these metals allow current flow only in one direction. This term was coined by Güntherschulze and Betz as “vollständige ventilwirkung” or complete valves effect in Al, Bi, Sb, and Ta or “unvollständige ventilwirkung” for partial valve effect in Ag, Cd, Fe, Mg, W, Zn, Zr [42]. The potentially protective nature of these oxides towards corrosion in many environments make these materials ideal candidates for operation in microfluidic systems. Metal oxide (MO) formation by electrochemical anodization proceeds, ideally, through the following reaction scheme where the metal (M) reacts with water to form the oxide [43]:



The growth of oxide films was experimentally described to follow the high field model [44], whereby the film grows both by ion migration and diffusion and the dependence of anodization current on the applied electric field is given by Eq. 10:

$$i = i_0 \exp(aE) \quad \text{Eq. 10}$$

where i is the oxide formation current, i_0 the initial current density, a the high field constant, and E the electric field strength in the oxide. In solution, the anodic potential or current can be supplied from an external circuit for precise control of the final oxide layer thickness. The theory of oxide formation has greatly evolved from the initial formulations of Güntherschulze and Betz in 1934 [42]. The process is schematically shown in Figure 5, with Figure 5a, showing adjacent lattice planes in the oxide and Figure 5b the activation energy reduction due to the applied electric field for the hopping ions. The hopping movement of the ions occurs via a neighboring vacancy or interstitial position at a distance equal to the lattice constant a , requiring an activation energy W . When an electric field is applied ($E > 0$) the activation barrier is lowered in the direction of the applied field (W_{\rightarrow}) by $\alpha zFEa$ with α being the transfer coefficient, z the mobile species charge, and F Faraday's constant. Conversely, the activation barrier is increased in the opposite direction. A detailed and complete derivation, which retains the functional form of Eq. 10, can be found in Ref. [45]. The rate determining step (RDS) in this model could be either ion transport through the interfaces, for example the -

oxide/electrolyte [46] or the metal/oxide [47], or within the oxide [48], depending on the material system.

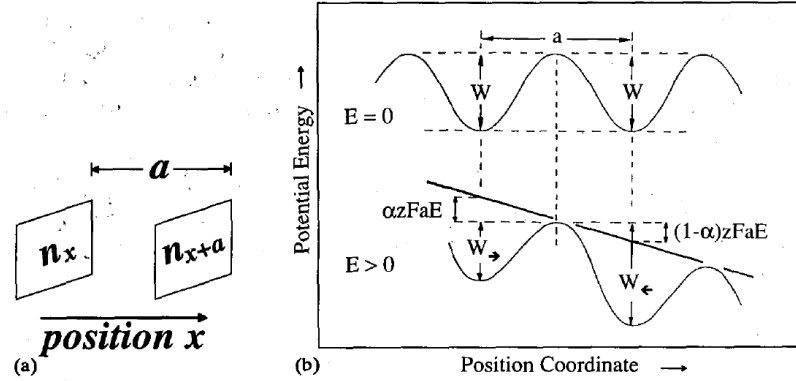


Figure 5: Schematic of the high-field model (a) the adjacent lattice planes in the oxide (b) the effect of electric field on activation energy (W). Images from Ref. [45]

Although the high field model broadly describes the formation of anodic oxides, it does not capture all the important features of the process, and the final properties of the film are highly dependent on the nature of the mobile metal ions, oxygen, and various ionic electrolyte species as well as the overall crystallinity of the resulting materials. Amorphous oxides (Al, Nb, and Ta) are formed via the transport of both anions and cations with transport numbers close to 0.5 at high field, as indicated by marker studies [49], [50]. Therefore, the oxide growth occurs simultaneously at both the metal/oxide and oxide/electrolyte interface. In contrast, the growth of crystalline oxides (Hf and Zr) is dominated by the transport of oxygen anions along grain boundaries giving transport numbers close to 1.0 [45], [51].

The simultaneous growth of the amorphous oxides at both interfaces leads to formation of point defects, with the oxygen vacancies creating an n-type region at the metal/oxide interface and metal ion vacancies generating a p-type region at the oxide/electrolyte interface. Additionally, electrolyte components tend to be incorporated at the oxide/electrolyte interface. For example, borate based electrolytes result in the presence of B_2O_3 in the outer third of the oxide film [52]–[54]. The resulting film has a p-intrinsic-n (p-i-n) structure, shown in Figure 6 for anodically grown aluminum oxide [55], [56]. As the thickness of the film increases, the intrinsic region grows while the defect

regions do not, remaining near the interfaces. Consequently, thin film amorphous oxides tend to show a highly asymmetric behavior in transport properties.

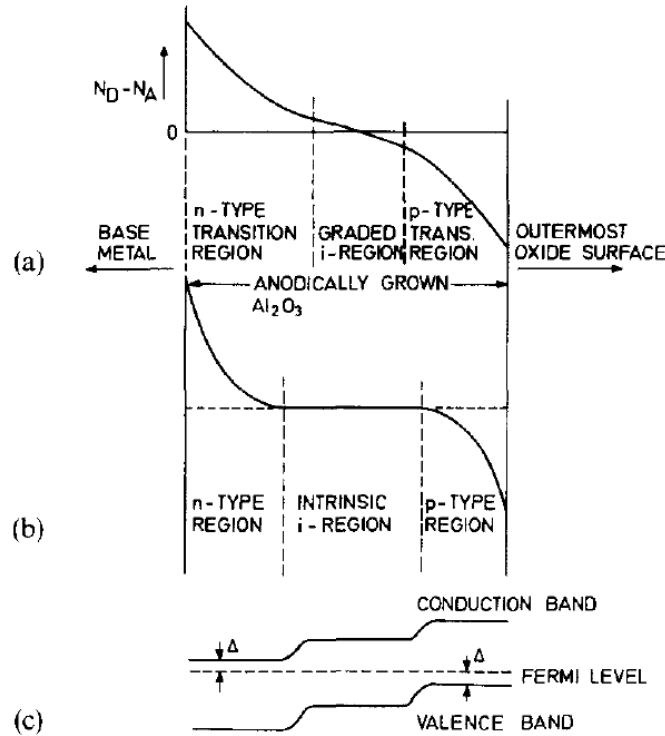


Figure 6: Schematic of a p-i-n structure in as-grown anodic Al_2O_3 for (a) thin films and (b) thick films. Image from Ref. [56]

2.4 Conduction Phenomena in Dielectrics

The metal oxides exhibit a large band gap (3 – 9 eV) and are classified as dielectric; however, upon the application of an electric field, a small current still flows through the layer, due to the presence of defects, enabling transport of electrons or ions through various conduction mechanisms. The continuous flow of this leakage current causes electrical stresses distributed across the dielectric, resulting in breakdown and failure when a critical defect density creates a percolating conductive path between the electrodes [57], [58]. For electrowetting devices designed for continuous operation, reliability of the dielectric is paramount; therefore, common leakage mechanisms are discussed in the following to elucidate the underlying phenomena which may eventually cause failure of the dielectric.

The tightly bound electrons in a dielectric layer respond to applied fields through a change in dielectric polarization. At temperatures higher than 0K, some electrons can be thermally excited and a small concentration of donor impurity levels can populate the conduction band. The conduction current in insulators under a small electric field will be very small because their conductivities are inherently low, on the order of 10^{-20} - 10^{-8} ohm⁻¹-cm⁻¹. However, conduction current through the dielectric film is significant when large electric fields are applied.

The band structure of a solid is determined by its crystal structure and locally by its short-range order [59], generating a well-defined forbidden gap for crystalline solids. However, many dielectric layers are amorphous, which tend to smear the band edges, as shown schematically in Figure 7 [60]. The amorphous nature as well as interstitials, surface states, and vacancies allow for electronic processes to occur at lower energies than ideal band-gap insulators [43]. As a result, the observed current densities are much higher than theoretically expected [60].

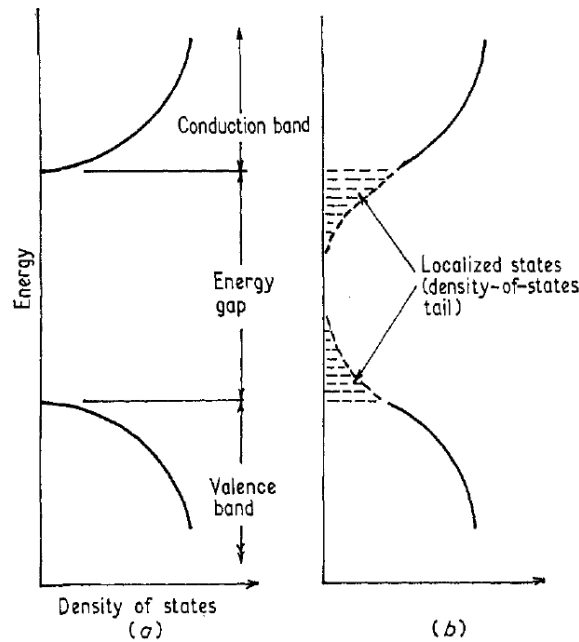


Figure 7: Energy diagram of an insulator (a) crystalline (b) amorphous. Image from Ref. [60]

The materials of interest for electrowetting application are all insulators with a band gap of at least several eV, which results in a very low electrical conductivity. Several transport mechanisms can

coexist at once, but generally one dominates, depending on dielectric thickness [61]. Conduction processes in dielectrics are primarily classified as either electrode-limited or bulk-limited, as summarized in Figure 8 for a metal-insulator-metal configuration. Electrode-limited conduction depends on the properties of the electrode/dielectric interface and follows a temperature-induced or field-induced emission (A), Fowler-Nordheim tunneling (B), or direct tunneling (F). Bulk-limited conduction depends on the electrical properties of the dielectric layer, specifically the trap energy distribution and their mutual distance throughout the layer, resulting in one of the following transport processes: Poole-Frenkel emission (C), space-charge, or ionic conduction (E).

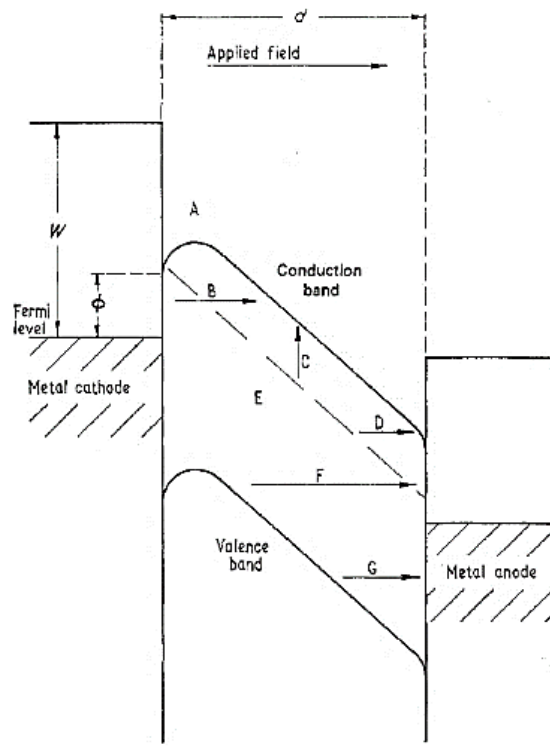


Figure 8: Overview of possible conduction mechanisms in metal-insulator-metal systems. Image from Ref. [61]

2.4.1 Electrode-Limited Conduction Processes

A commonly observed conduction mechanism in dielectric films is thermionic emission, which is described by the Schottky-Richardson Equation (Eq. 11). Current flows due to the rate at which electrons are thermally excited over the interfacial energy barrier (ϕ) into the conduction band. When

electrons can gain enough energy to overcome the energy barrier at the metal-dielectric interface, they are injected in the dielectric. This interfacial barrier height can be greatly reduced by an image force (β), a phenomenon known as the Schottky effect.

$$J = AT^2 \exp\left(\frac{-\phi}{kT}\right) \exp\left(\frac{\beta E^{\frac{1}{2}}}{kT}\right) \quad \text{Eq. 11}$$

$$\text{where, } \beta = \frac{q^3}{4\pi\epsilon_r\epsilon_0}$$

In Eq. 11 J is the current density, A the Richardson constant, ϕ is the total barrier to thermionic emission, β the Schottky field lowering coefficient, and E is the electric field. The Schottky plot ($\ln(J/T^2)$ vs $E^{1/2}$) is commonly used to measure the barrier height of the interface from the resulting linear intercept at $E=0$. With increasing field the barrier bending is enhanced, lowering the barrier and increasing the probability of tunneling as the wave function can penetrate through the triangular barrier. This results in another carrier injection mechanism to dominate, tunneling, which is described by the Fowler-Nordheim relationship, Eq. 12,

$$J = \frac{m q^3}{m^* 8\pi h \phi} E^2 \exp\left(\frac{-8\pi(2m^*)^{1/2} \phi^{3/2}}{3qh} \frac{1}{E}\right) \quad \text{Eq. 12}$$

with m^* being the electron effective mass in the oxide. If the oxide is very thin, less than 50Å, direct tunneling can occur. Direct tunneling isn't explicitly considered here, as the breakdown voltage for a layer with a thickness having direct tunneling would be well below the voltage needed to elicit significant contact angle change.

2.4.2 Bulk-Limited Conduction Processes

A process analogous to Schottky Emission can also occur in the bulk of the dielectric, where electrons can be excited from trap states into the conduction band. This process is known as Poole-Frenkel (PF) emission, Eq. 13, which describes a reduction of the energy barrier for the trapped electron due to an applied field across the dielectric film, increasing the probability of emission. The slope of the linearized PF emission equation is half of that observed in the Schottky emission, a feature which allows to differentiate the two mechanisms through their temperature dependence.

$$J = J_0 E \exp\left(\frac{-\phi}{kT}\right) \exp\left(\frac{\beta E^{1/2}}{2kT}\right) \quad \text{Eq. 13}$$

If carrier injection occurs through an ohmic contact, the current is typically limited by space-charge, due to a field-generated charge imbalance in the dielectric. This formulation was first proposed to describe electron transport in a vacuum diode, which has been modeled with Child's law [62], using an assumption of no scattering. Mott and Gurney instead formulated a trap-free space charge current for solid materials considering single carrier scattering [63], arriving at

$$J = \frac{9}{8} \epsilon_r \epsilon_0 \mu \frac{V^2}{t^3} \quad \text{Eq. 14}$$

with μ being the carrier mobility, and t the film thickness. Both the voltage and thickness dependence have been experimentally confirmed, but real systems exhibit a high density of trap sites, leading to a different voltage dependence [64]. Once enough charge is passed, the trap states become filled, and Eq. 14 is again applicable [65].

2.5 Breakdown

The breakdown strength of the dielectric material is paramount for any electrowetting device application and operation. As shown in Figure 1, the breakdown strength strongly influences the minimum voltage required for operation. Breakdown occurs by ramping the applied voltage in solid-state measurements until an abrupt and irreversible jump in the leakage current occurs, leading to an increase of several orders of magnitude. Alternatively, time-dependent dielectric breakdown (TDDB) monitors the time to failure at a constant field below the breakdown voltage. High- k materials have been under investigation as replacement gate dielectrics in CMOS systems since SiO₂ films have become susceptible to electron tunneling as a consequence of ongoing device miniaturization. The search for new dielectrics has led to an interest in the long term reliability of these structures, leading to the availability of physical models with predictive ability.

The initial stages of failure in dielectric layers have been shown to occur as a result of both current- and field- induced mechanisms [58], [66], [67], followed later by increased current flow causing Joule-heating. The thermochemical model [68] postulates the presence of large local electric fields generated by superposition of the applied electric field and the dipolar field described by the Mossotti field (or Lorentz relation) $E_{loc} = [(2+k)/3]E_{app}$ [69]. This relation indicates that as the dielectric strength (k) of the material increases, so does the local field, leading eventually to distorted bonds and weakened bond strength of polar species, which become susceptible to breakage through

thermally activated processes [70]. As bonds break, conductive paths continue to form, leading to increasing current and simultaneous thermal degradation that cause the eventual failure of the layer. Alternative physical models of breakdown involve hole injection from the anode [71] instead of electron injection from the cathode, and/or the release of hydrogen at the anode [72]. The anode hole injection model hypothesizes that hole trapping caused by impact ionization of hot electrons may be the cause of breakdown. As the generated holes are trapped at the cathode region, the potential barrier decreases leading to the enhancement of Fowler-Nordheim tunneling, generating larger current injection, until a critical hole density is reached, sufficient to induce breakdown. Similarly in the hydrogen release model, the impact of hot electrons at the anode releases hydrogen, which under the applied field travels back to the cathode generating defects. The latter mechanism has been shown to be important at SiO₂/Si interface, since during processing these materials are subjected to thermal annealing in forming gas to passivate defects [48]; it is unclear whether the other oxide materials may be susceptible to this degradation mechanism.

Chapter 3

Experimental Methods

This chapter describes the key experimental methods for fabrication and characterization of the bilayer films used throughout this work. Emphasis is placed on the less commonly used techniques. The formation and characterization of the hydrophobic layer is separated for a more in depth discussion covered in Chapter 5.

3.1 Anodization

Oxide layers were grown through anodic oxidation of evaporated or sputtered aluminum and tantalum films, respectively, forming the primary insulating dielectric layer for our electrowetting systems. The theoretical details of the anodization process are covered in detail in Chapter 2.2. Many different anodization electrolytes were tested to achieve optimal formation conditions of these materials, but the most consistent and reproducible solution for both metals as covered in Chapter 4, was 30 wt% ammonium pentaborate ($\text{NH}_4\text{B}_5\text{O}_8$) in 99.99% ethylene glycol.

Aluminum films of 100 nm thickness were grown by e-beam evaporation (CHA Industries, Fremont, CA) onto the native surface of a Si wafer, pre-coated with a 5 nm thick titanium adhesion layer. Samples were cut from the main wafer using a diamond scribe, cleaned successively with an acetone, isopropanol, and methanol rinse. Aluminum anodization was performed at room temperature in a two electrode electrochemical cell with the electrodes in a vertical configuration at constant potential for 8 minutes, using a platinum mesh counter electrode. Figure 9(a) shows the cell configuration with the current density vs. anodization time in Figure 9(b). The oxide thickness remained nearly constant after ~ 2 min, determined by ellipsometry, as the majority of charge is given within the first 30 s with high current values (charge = current x time). A Kepco power supply controlled the voltage, and a Keithley 2001 meter was used to monitor current flow, controlled by a LabVIEW program. After anodization the oxide layer was cleaned with Millipore water and acetone, then immediately used or stored in a vacuum desiccator. Tantalum films of 100 nm thickness were sputtered onto a native Si wafer. Anodization and preparation of the surface followed the same procedure as the aluminum layers.

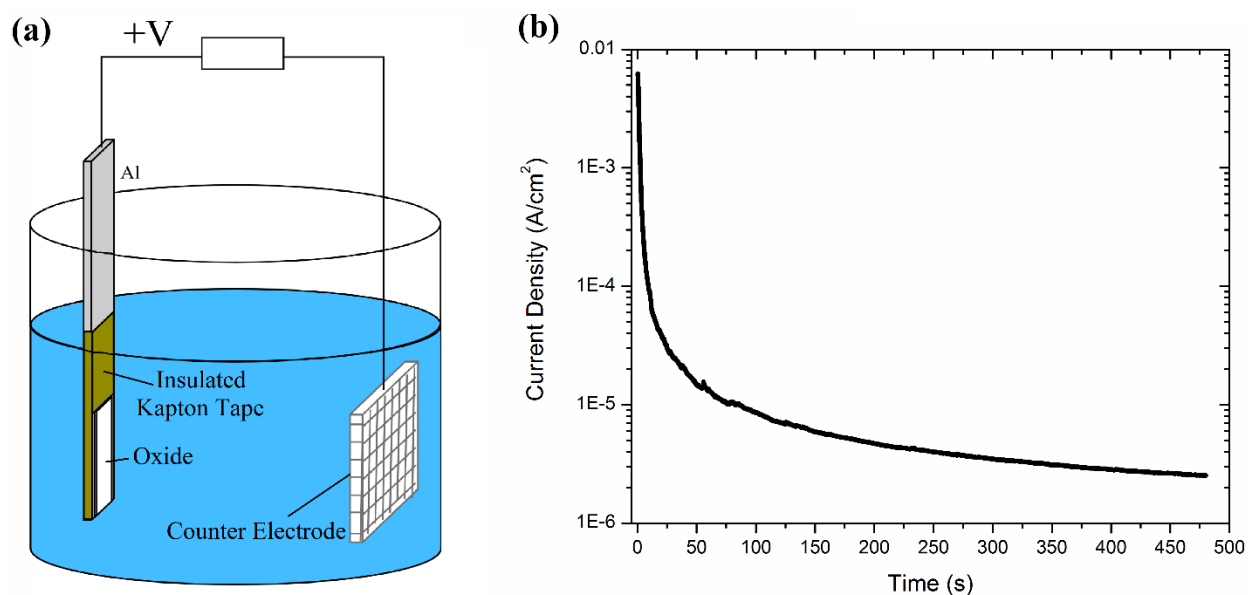


Figure 9: (a) Anodization Setup with using an aluminum bar and a platinum counter-electrode (b) current density vs. time for aluminum oxide anodization at 20 V.

3.2 Current – Voltage and Capacitance Measurements

The current-voltage (I-V) characteristics of the oxide films were recorded using both a metal-oxide-metal (MOM) and an electrolyte-oxide-metal (EOM) configuration. A basic schematic for the testing procedure is given in Figure 10. The samples are placed on a Micromanipulator 7000 probe station with two leads connected via a vacuum chuck to the probe station. Each probe used a gold plated tungsten needle, connected to a HP 4145b semiconductor property analyzer.

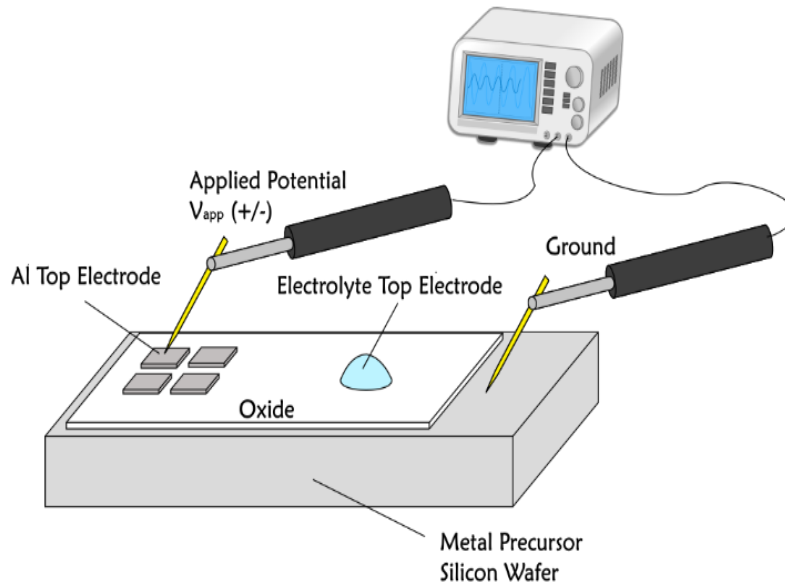


Figure 10: Set up for I-V and C-V measurements

MOM contacts were obtained by depositing a 100 nm thick Aluminum film with e-beam evaporation on top of the metal oxide barrier layer. Eight independent Al contacts with 0.80mm^2 area were grown at distinct locations on the oxide using a shadow mask. EOM contacts were prepared by carefully positioning a $1.5\mu\text{L}$ droplet of a $.05\text{M}$ sodium sulfate solution on the oxide surface with a pipette. All solutions described above were prepared from Milli-Q water (resistivity $18.2\text{ M}\Omega\cdot\text{cm}$), using chemicals from Sigma-Aldrich with $>99\%$ purity.

The same measurement configuration was additionally used with a Keithley 4200 SCS Parameter Analyzer. The I-V characteristics measured with the Keithley system confirmed the same sample characteristics measured with the HP 4145b system. The Keithley system allows for capacitance measurements, which were run in the MOM configuration sweeping both bias and frequency, for dielectric constant determination.

3.3 X-ray Reflectivity (XRR) [74]

A X-ray Reflectivity measurement is commonly used to characterize thin films using the principle of refraction rather than Bragg diffraction. The XRR measurement uses the direction normal to the film surface to obtain film thickness, interfacial roughness, and density of the surface.

A basic schematic of the measurement is given for a flat substrate in Figure 11. The scan begins at a $2\theta = 0^\circ$ where the beam is initially totally reflected by the air-film interface. Once the incident angle equals the critical angle, defined as the angle below which total reflectance of the x-ray beam occurs [75], x-ray propagate across the sample surface. The critical angle is given by Eq. 15,

$$\cos(\theta_c) = n \quad \text{Eq. 15}$$

with n the refractive index of the material, a density dependent quantity, with $n = 1$ for air as a reference. For angles greater than θ_c , X-rays penetrate the substrate by refraction. The intensity decays rapidly following an oscillatory behavior, known as Kiessig fringes. The Kiessig fringes occur as a result of a phase shift resulting in constructive and destructive interference from the two interfaces, the substrate and the film in this simplified case, with the period of oscillation dependent on thickness. The film thickness (T) is calculated by Eq. 16,

$$T = \frac{2\pi}{\Delta q_z} \quad \text{Eq. 16}$$

with q_z ($q_z = 4\pi\sin(\theta)/\lambda$) being the period of oscillation in reciprocal space from the reflected intensity.

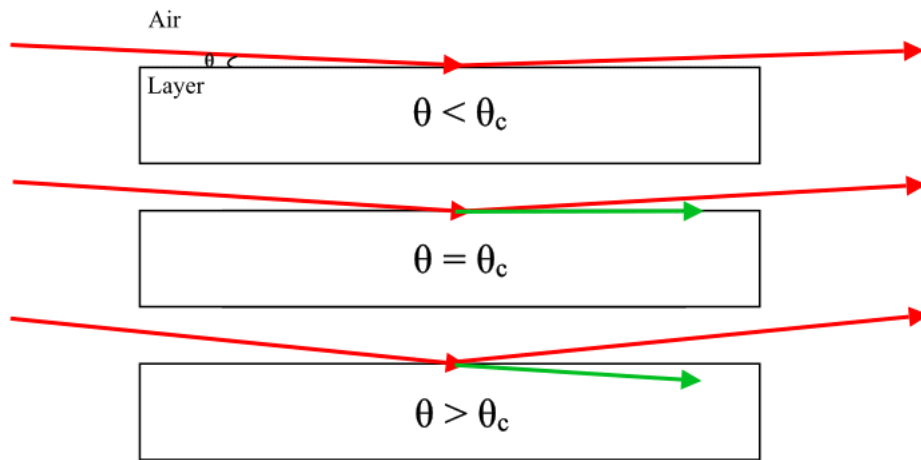


Figure 11: Basic XRR measurement beam alignment

The XRR measurements were performed using a Panalytical X'Pert Pro system in a grazing incident beam configuration. Each sample requires a series of optimizations for the beam and sample alignments to maximize the signal during the measurement prior to the XRR measurement. The beam was scanned over a 2θ range from 0° to 3° , after which the measured intensity could not be distinguished from the instrument background noise. Figure 12 shows the experimental XRR patterns for a 100 nm sputtered tantalum layer (blue) and the substrate after anodization with a resulting 8 nm oxide layer. The key features of the measurement are highlighted showing the location of the critical angle, the Kiessig fringes for both the oxide and tantalum layers (Figure 12(b)), with the roughness a function of the slope at higher 2θ values ($>1^\circ$).

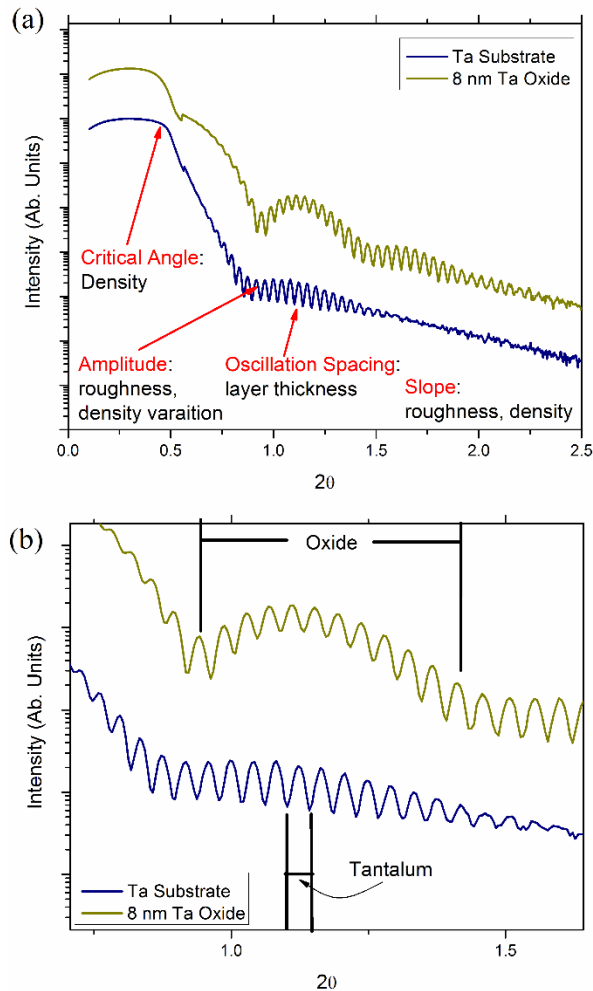


Figure 12: (a) XRR data for tantalum (purple) and tantalum oxide (gold) layers, with XRR features highlighted in the plot and (b) Kiessig fringes

The primary method to analyze the XRR data requires building a model of the system initially with approximate values for density, roughness, and thickness. For example in Figure 12, the system is a silicon layer, tantalum layer, and tantalum oxide. The thickness of the layers can be simply assessed from the Kiessig fringes using Eq. 16 for tantalum and tantalum oxide; silicon isn't detected since its thickness is larger than 200 nm. Using an estimated roughness and bulk density for each layer, the software creates a simulated profile of the structure. This simulated structure is modeled through the Panalytical Reflectivity software package and then compared to the actual spectra. The software runs a least squares fit from the simulated material structure to the experimental data, varying the layer thicknesses, roughness, and density. The procedure must be carried out with care as it is easy for the software to produce non-physical results without constraining the various parameters, but for our system the substrate/oxide parameters are already approximately known, facilitating the procedure. The most reliable method for interpretation was to understand the properties of the individual layers. For example in Figure 12(a), constructing the model for the tantalum substrate is a simple fit, giving density, thickness, and roughness for the layer. Analyzing anodized films would utilize the previously determined properties of the base layer. This becomes particularly important for self-assembled monolayers (See Chapter 5) as the variations in the XRR data are minor, and require a complete model of the underlying layers.

3.4 Scanning Kelvin Probe

Scanning Kelvin Probe (SKP) is a non-contact technique that utilizes a vibrating capacitive probe to measure the surface potential between a sample and the vibrating probe [76], thus generating a map of the contact potential difference, equal to the local work function. A simple description of the technique is shown in Figure 13 demonstrating the measurement when two metals are brought together. Initially in (a) the two metals are not connected, and E_{F-i} (the Fermi energy) and Φ_i (the work function), with the subscript i representing metal 1 or 2. Connecting the metals through an external circuit (b) results in electrons flowing from the lower work function (metal 2) to the higher work function (metal 1), until the Fermi levels equal. The measurement determines this voltage difference between the materials by externally applying a voltage (V_{app}) until no current flows (c). The basic overview from Figure 13 shows how the system works when using the system for two conductors, just as was done originally by Lord Kelvin in 1898 [77]. Measurements for the materials in this work do not measure work function, but rather surface potentials for the insulator surface. The system

utilizes a vibrating gold probe with a sinusoidal vibration over the sample (Figure 13(d)), optimized in design to provide a significantly more sensitive measurement than the overview from (a)-(c).

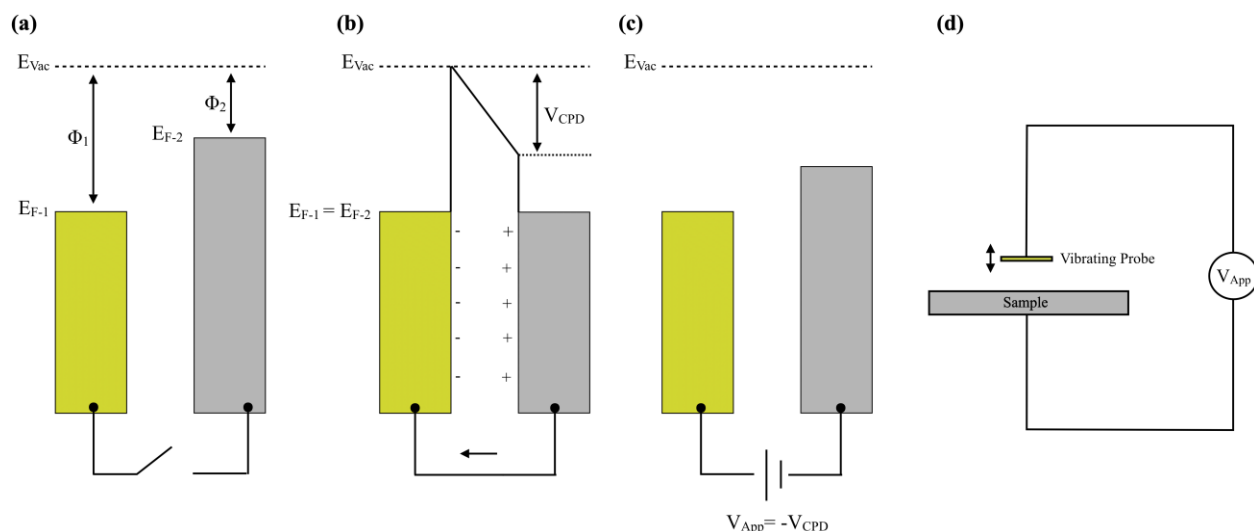


Figure 13: Schematic of SKP operation (a)-(c) process of measuring the contact potential difference between two metals and (d) the actual measurement configuration used.

SKP measurements were performed with a KP Technology (Scotland) Ambient Advanced SKP system using a 50 μm diameter gold coated probe tip. Using the null-method, an external bias is applied until no current is observed, defining the contact potential difference (CPD). We employ the SKP technique to monitor the damage of the bilayer structure after EWOD measurements by scanning at 0.25 mm intervals in an x-y grid to produce a surface map. The CPD values from the Kelvin probe allow for the charge density in the film to be determined and correlated to electrowetting performance.

3.5 Static Contact Angle

A Ramé-Hart Goniometer Model-200 (Succasunna, NJ) was used to image and quantify contact angles using their analysis software, DROPimage Standard. The system, shown in Figure 14, simply uses a camera to image the drop with a light source placed behind the drop, with a resulting image given in Figure 14(b). Static electrowetting measurements were performed by placing in air a 10-100 μL drops of a 0.05M sodium sulfate solution on a bilayer stack and applying voltage between the metal substrate and an inert Au probe in contact with the electrolyte drop. A Kepco power supply controlled the voltage, and a Keithley 2001 meter were used to monitor current flow, using a Labview program.

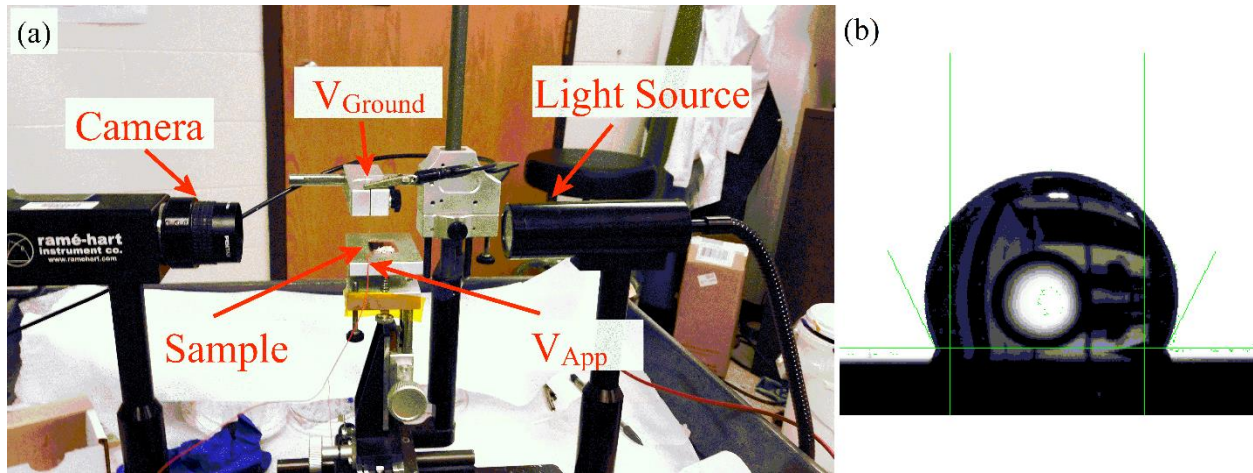


Figure 14: (a) Static EWOD measurement system (b) DROPIImage Standard Software for contact angle determination

3.6 Dynamic Contact Angle

Dynamic contact angles describe three phase boundary motion giving “advancing” and “receding” contact angles, with their difference defining the contact angle hysteresis (CAH). CAH is typically measured using one of three methods [78]. The simplest technique induces drop motion by tilting the sample, monitoring the angles optically while the droplet slides (similar to the static angle system). The second method adds and removes liquid from the drop, measuring the contact angle during the change in volume. The third method externally controls the movement of a surface, measuring the resulting force from dipping the sample into and out of a liquid bath. The technique, known as the Wilhelmy plate method, calculates the contact angle by performing a force balance on the sample, using Eq. 17 & Eq. 18. The instrument corrects for the sample weight by tarring prior to insertion into the liquid. The effects of the buoyancy force are isolated by extrapolating the graph back to the zero depth of immersion. The remaining force is the wetting force (Eq. 18) with P as the wetted area, allowing for contact angle determination.

$$F_{total} = F_{wetting} + \text{weight of probe} - \text{buoyancy} \quad \text{Eq. 17}$$

$$F_{wetting} = \gamma_{LV} \cdot P \cdot \cos \theta \quad \text{Eq. 18}$$

Our work used a Krüss tensiometer and a Kepco power supply when investigating voltage dependent performance. A schematic of the technique and the resulting data are shown in Figure 15. Initially, the immersion shows changing force-depth behavior upon contact of the edge with the liquid surface and any edge inhomogeneities until 1.5 mm. Typically the repeated measurement on the surface is performed at a depth far away from the edge of the sample, 4 mm to 8 mm for this example. The advancing and receding angles are calculated by linear fit (dotted red line) of the highlighted advancing and receding regions extrapolated to zero immersion. In contrast with sessile drop contact angle measurements, the system allows us to perform these contact angle tests in an uncommon configuration changing the shape of the three phase boundary, and explore the impact of contact angle saturation in electrowetting (see Section 6.5) and hysteresis.

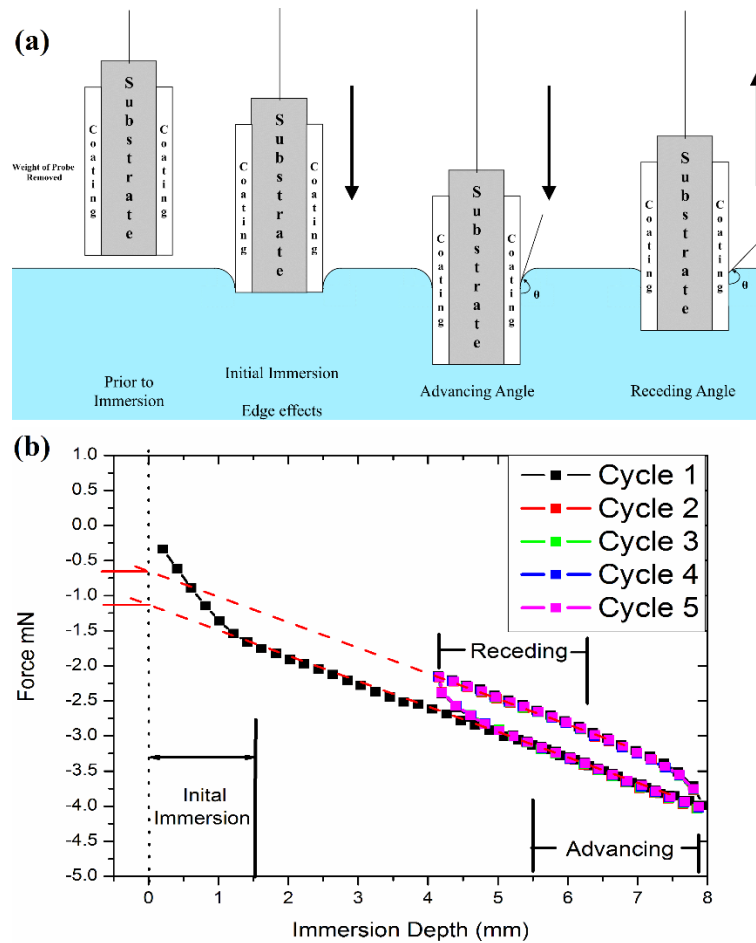


Figure 15: (a) schematic of a hydrophobic coated substrate being dipped into a liquid bath showing advancing and receding contact angles. (b) Corresponding force-immersion depth data for the process in (a). Data from a 21 nm Cytosol surface (from Chapter 5)

3.7 Scanning Electron Microscopy and Energy Dispersive X-ray spectroscopy

A scanning electron microscope (SEM) allows for the imaging of a surface by focusing an electron beam through a series of magnetic lenses onto a material under investigation. The beam is rastered across the sample surface, using secondary emitted electrons, picked up by the detector, resulting in a computer processed image. If the electrons are of sufficient energy, they excite electrons from the material under examination to a higher energy state, which releases characteristic x-rays, allowing for elemental analysis known as energy dispersive X-ray spectroscopy (EDS) [79].

This work used a FEI Quanta 650 SEM with an attached Oxford X-Max^N EDS detector to examine the surface of the oxides and polymers. As the systems under investigation are insulating, very low accelerating voltages were used, typically 500 V, to minimize charging while allowing for surface imaging. Higher energies were used for EDS measurements, still below 5kV, to generate K-alpha characteristic X-rays from the sample for element identification.

3.8 Atomic Force microscopy

Atomic force microscopy (AFM) uses a force probe to “touch” the surface in order to produce two-dimensional surface topography at the nanometer length scale [80]. The probe tip attached to a flexible cantilever is placed near the surface of interest, as shown in Figure 16. The cantilever bends due to surface forces while scanning. A laser is focused on the top of the cantilever, reflecting onto a photodiode. The bending of the cantilever is then quantified by the changing response of the photodiode, turning into a 2D height image.

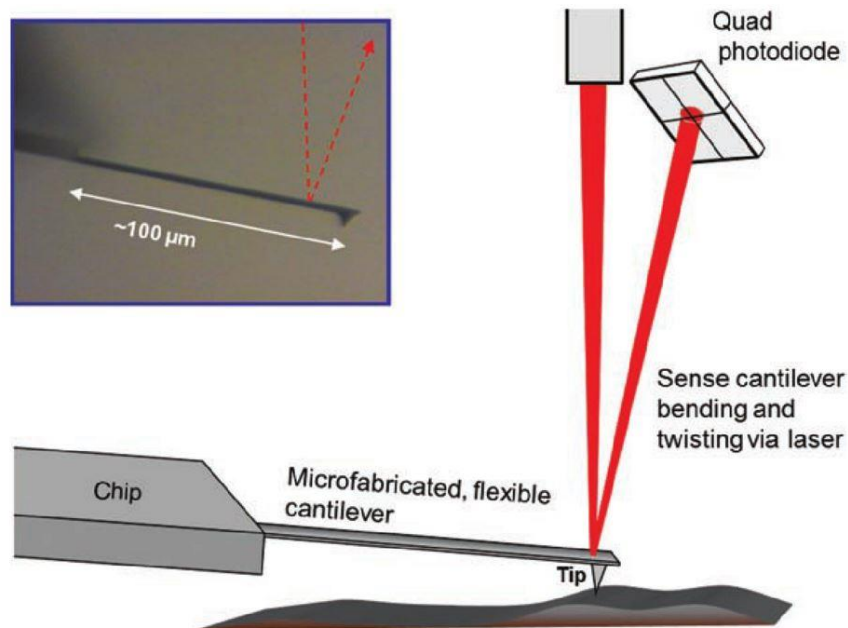


Figure 16: Schematic of AFM operation. Image from Ref [80].

A Bruker Innova AFM system has been used to primarily study polymer and SAM materials in this work. Silicon AFM probes with a force constant of 40 N/m covered with an aluminum reflective coating were used in tapping mode. Tapping mode uses tip oscillation at its resonance

frequency (300-400 kHz) intermittently contacting the sample surface [81]. This mode of operation limits the modification and damage on soft materials, while reducing wear on the probe tip. AFM scans were analyzed through the Bruker NanoScope Analysis v. 1.5 software allowing for height and roughness calculations, cleaning up noise, and removing sample tilt.

3.9 Mott-Schottky

Mott-Schottky analysis is a specific type of impedance measurement to characterize the doping type and density as well as the flat band voltage of a semiconductor electrode. This technique has also been effective in characterizing insulating layers under the same principle by measuring the voltage dependence capacitance under depletion conditions[82]–[86]. We use the technique to quantify the defects in the amorphous metal oxides.

Under depletion conditions the dominant measured capacitance is the space charge in the oxide layer. Using the 1-D Poisson's equation, Eq. 19, relates the charge density (ρ) at a position x from the surface to the potential difference (V).

$$\frac{d^2V}{dx^2} = \frac{\rho}{\epsilon_r \epsilon_0} \quad \text{Eq. 19}$$

Using Gauss' law relating the electric field to the charge at the interface and the Boltzmann distribution to describe the electron distribution, Eq. 19 can be solved for the Mott-Schottky expression (Eq. 20) giving a voltage dependent inverse square capacitance relationship [86], [87].

$$\frac{1}{C^2} = \frac{\pm 2}{\epsilon \epsilon_0 e N} \left(V - V_{fb} - \frac{kT}{e} \right) \quad \text{Eq. 20}$$

with C the capacitance, e is the elementary charge, V the applied potential, V_{fb} the flat band potential, k the Boltzmann constant, and T is the absolute temperature. The measurements were performed in pH 9.2 borate buffer solution (.075M $\text{Na}_2\text{B}_4\text{O}_7 \cdot 10 \text{H}_2\text{O}$ and 0.05M H_3BO_3) at room temperature with a Mercury/Mercurous Sulfate reference electrode (MSE, $0V_{\text{MSE}} = 0.65V_{\text{SHE}}$) at a frequency of 1 kHz in the potential range $0-2V_{\text{MSE}}$ using a Biologic SP-150 potentiostat (Grenoble, France)

The measurement applies a small amplitude (10-15 mV) sinusoidal ac voltage, $V(t)$ Eq. 21, with the resulting current given by Eq. 22, with I_0 as the steady-state current and I_m the maximum current from the sinusoidal signal. The resulting impedance, Z , is simply given in Eq. 23 using Ohm's law with the angular frequency ω .

$$V(t) = V_0 + V_m \sin(\omega t) \quad \text{Eq. 21}$$

$$I(t) = I_0 + I_m \sin(\omega t + \theta) \quad \text{Eq. 22}$$

$$Z(\omega) = \frac{V(t)}{I(t)} = Z' + jZ'' \quad \text{Eq. 23}$$

The capacitance (C) is calculated from the imaginary component of the impedance in Eq. 24, measured at the frequency (f) with the highest capacitance [86], typically around 1 kHz for the oxides under investigation.

$$Z'' = -1/(2\pi f C) \quad \text{Eq. 24}$$

Chapter 4

Dielectric Oxide Properties

Part of this chapter is reproduced from:

M. Mibus, C. Jensen, X. Hu, C. Knospe, M. L. Reed, and G. Zangari, "Dielectric breakdown and failure of anodic aluminum oxide films for electrowetting systems," *J. Appl. Phys.*, vol. 114, no. 1, p. 014901, 2013.

and

M. Mibus, C. Jensen, X. Hu, C. Knospe, M. L. Reed, and G. Zangari, "Improving dielectric performance in anodic aluminum oxide via detection and passivation of defect states," *Appl. Phys. Lett.*, vol. 104, no. 24, p. 244103, Jun. 2014.

This chapter discusses the properties of the anodically formed metal oxide films: aluminum oxide and tantalum oxide. In order to assess the performance of EWOD systems, it is important to decouple the properties of the typical bilayer system to gain insight into the processes occurring at each layer. Aluminum oxide and tantalum oxide films are characterized by their thickness (using ellipsometry and X-ray Reflectivity), Mott-Schottky measurements, and current – voltage (I-V) characteristics. Two types of I-V measurement configurations were used, metal – oxide – metal (MOM) and electrolyte – oxide – metal (EOM), to investigate both electronic and ionic processes in the films. Additionally, the dielectric constant for both systems is determined through capacitance measurements.

4.1 Aluminum Oxide

4.1.1 Oxide Growth

Several anodization solutions were initially experimented with for the formation of aluminum oxide; based upon the uniformity of the layer, the best breakdown characteristics, and reproducibility, a solution of 30 wt% ammonium pentaborate in ethylene glycol was selected. The solution was originally suggested by Diggle [49] based on the high current efficiency during formation. Figure 17 shows the Aluminum oxide thickness, as determined by ellipsometry, vs. anodization voltage. As expected the relationship is approximately linear, with an anodizing ratio of $\sim 1.2\text{nm/V}$. The sample anodized at 10V shows a positive deviation from the extrapolated linear trend; this behavior is ascribed to a change in the ionic migration process, dominated at low voltage by ion injection in the oxide, and at higher voltage by bulk ion migration, leading to an increase in average growth rate at thinner thickness [49].

On the same grounds, the extrapolation at low voltages should not be taken literally, since under these conditions both ion migration and diffusion may contribute to ionic transport.

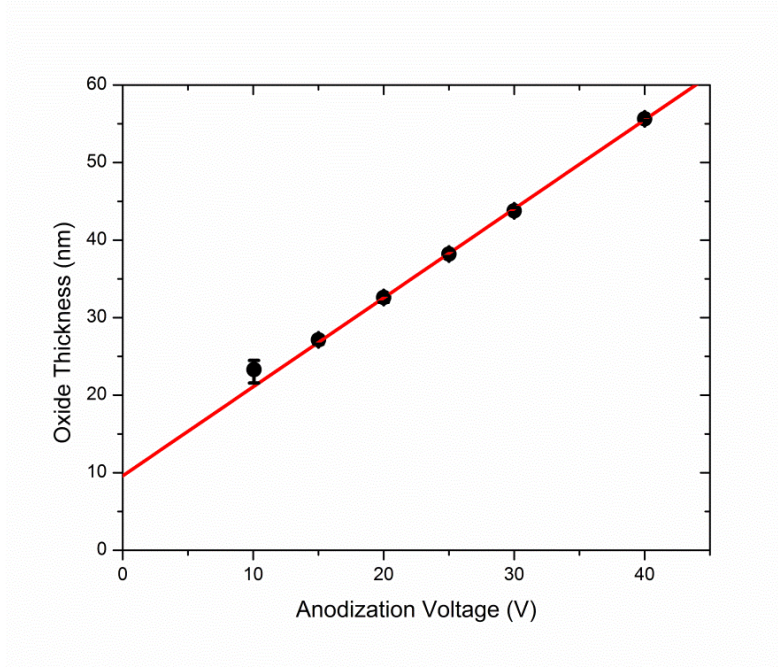


Figure 17: Thickness of anodized aluminum oxide films vs. anodization voltage. Thickness measurements by ellipsometry are in close agreement with calculations from the charge density.

4.1.2 Metal-Oxide-Metal Contacts

Current-voltage I-V characteristics for MOM contacts were recorded for various oxide film thickness and typical results are reported in Figure 18(a). The characteristics are highly non-linear and are asymmetrical with respect to polarity, with the positive polarity (positive voltage applied to the top Al contact) always showing breakdown at a lower voltage. A sharp, hard breakdown, leading to a steep current increase up to the maximum current allowed by the available instrumentation, is observed in all cases. The electrical behavior of the oxide is reversible if the applied voltage is maintained below the breakdown voltage V_B , but the changes in conductivity are irreversible if the region of breakdown is reached. Figure 18(b) reports V_B and the corresponding breakdown field $E_B = V_B/t$, measured under both polarities as a function of the oxide film thickness. For each sample, the error bars identify the highest and lowest value of V_B , E_B measured on that sample, and the symbols represent the average value. It is noted that both the scatter in V_B , E_B and the difference between $V_{B+}(E_{B+})$ and $V_{B-}(E_{B-})$ decrease with increasing thickness (i.e. increasing anodization voltage). The breakdown field for the oxides ranges between 3-7 MV/cm with the value leveling to 7 MV/cm in both polarities with

increasing film thickness (Figure 18(b)), similar to the values observed in other anodic aluminum oxide films [56], but higher than thermally oxidized aluminum (5MV/cm) [88], suggesting a better quality film.

The observed asymmetry in the I-V characteristics can be traced back to an asymmetry in the Al oxide film structure. During anodization, the large electric field in the oxide causes injection of metal ions from the metal side, and of anions from the electrolyte (O^{2-} , OH^- , borate), into the oxide. Opposite gradients in the concentration of both cations and anions are therefore present within the oxide, leading to the formation of a p-intrinsic-n (p-i-n) junction, where the p and n region are several nm thick as determined by their doping polarity is determined by an excess of anions and cations, respectively [55]. The presence of a p-i-n junction naturally leads to asymmetric characteristics; in addition, the degree of asymmetry would decrease with increasing oxide thickness since under these conditions the intrinsic region makes up most of the oxide thickness and would dominate the electrical behavior. Under positive bias the p-i-n junction is forward biased, and the resulting current is larger. A larger current flowing through the oxide would accelerate the breakdown process, leading to a lower breakdown voltage, as observed. It should be noticed also that during anodization the sample is subjected to negative bias polarization, according to the definition adopted here; the fact that a higher breakdown voltage is observed under these conditions suggests therefore that transport of charges becomes more difficult when the oxide is subject to the same bias present during anodization.

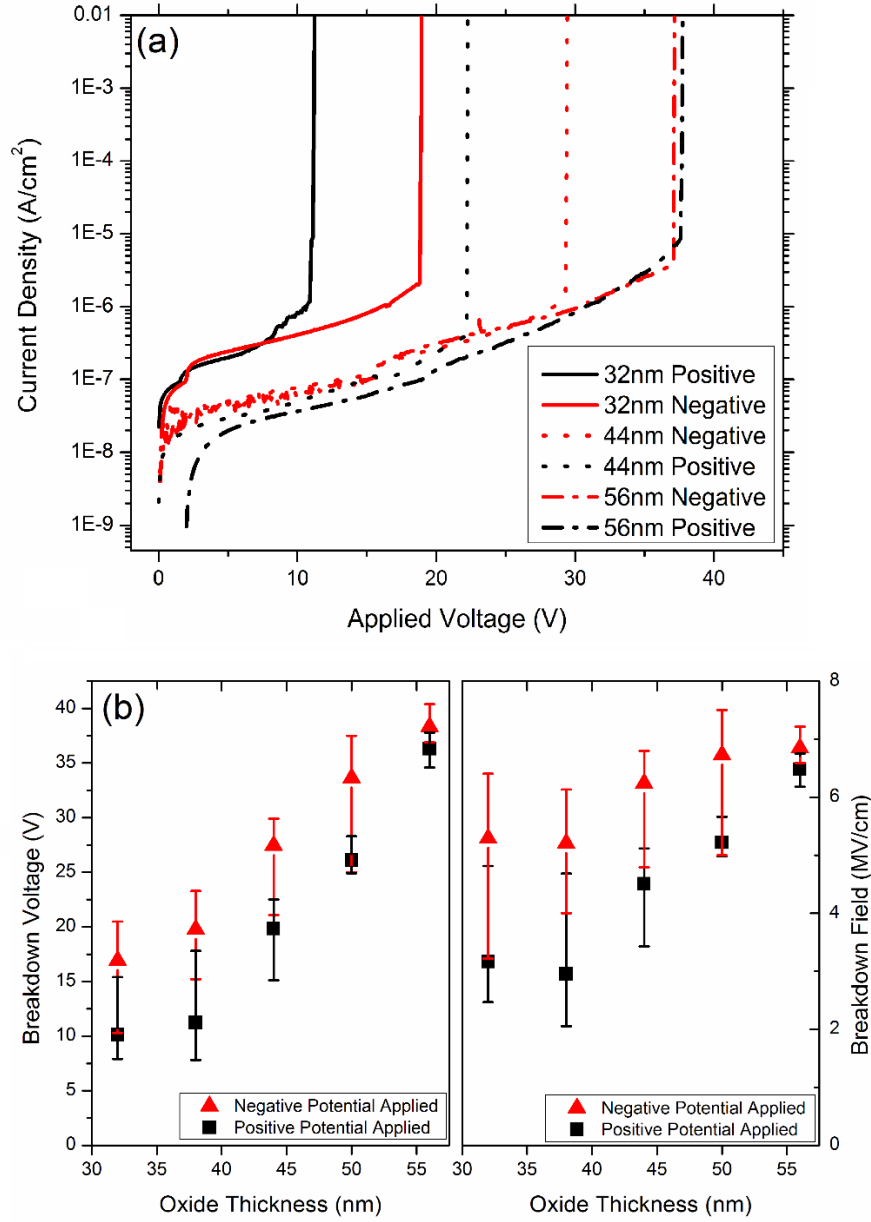


Figure 18: (a) I-V characteristics for aluminum oxide films of various thickness in a metal-oxide-metal configuration operating under both polarities (b) Breakdown voltage V_B and breakdown field E_B vs. film thickness for positive (black, square) or negative (red, triangle) polarity applied to the top contact. The error bars represent max and min values for the data scatter with the average value as the data point.

4.1.3 Electronic conduction processes in MOM contacts

The highly defected structure of anodized Al oxide gives rise to localized excess or deficit of oxygen, Al, or impurities, yielding a high density of trapped charges which act as electrically active defects [89]. The defect concentration has been quantified for a wide variety of passive metal films, yielding values in the range of 10^{18} - 10^{20} cm^{-3} [43]. Specific values for anodic aluminum oxide barrier layers have recently been measured at 10^{18} - 10^{19} cm^{-3} , depending on thickness [90]. Significant electronic conductivity may therefore be present, and various electronic conduction processes become thus possible. These include Schottky emission (SE) (Chp 2, Eq. 11), Poole-Frenkel emission (PF) (Chp 2, Eq. 13) and Fowler-Nordheim tunneling (FN) (Chp 2, Eq. 12) [61]; the total electronic current would therefore be: $j = j_{\text{SE}} + j_{\text{PF}} + j_{\text{FN}}$.

It is possible to fit the experimental I-V characteristics assuming that the three processes described above dominate within distinct applied potential regions. The transition from SE to PF emission in 56nm oxides is marked by a change in the slope in the semi-logarithmic characteristics (Figure 19(a)); a narrow voltage region just before the irreversible increase in current on the other hand can be fit with a FN tunneling characteristics. 32nm thick layers in contrast (Figure 19(b)) are better fit with a superposition of SE and FN tunneling only; this is consistent with thinner films being less dependent on charge traps for conduction.

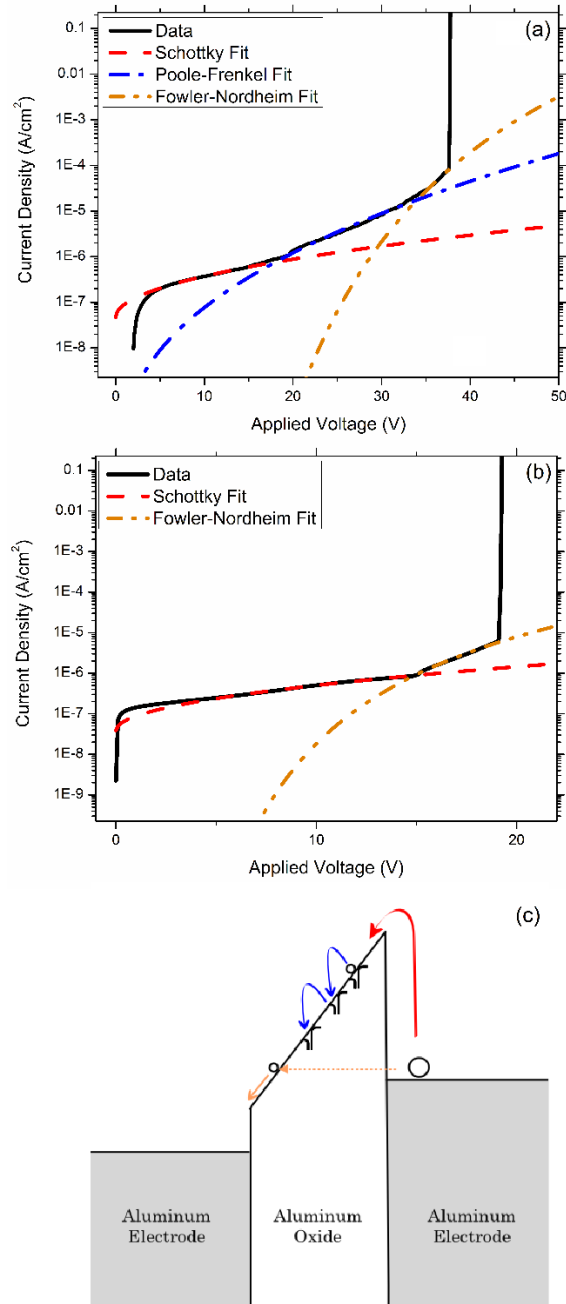


Figure 19: (a) Fit of the experimental I-V characteristics of a 56 nm thick Al oxide film to a combination of dielectric leakage mechanisms; each process in turn is assumed to dominate conduction in the voltage region where the corresponding characteristics applies: Schottky Emission (Red), Poole-Frenkel (Blue), Fowler-Nordheim (Orange). (b) I-V characteristics of a 32nm thick oxide layer; a good fit could be obtained by assuming only SE and FN conduction mechanisms. (c) Schematic for the MOM electronic conduction mechanisms.

In summary, the current flowing through Al oxide dielectric films is electronic in nature and is described by a combination of emission, hopping, and tunneling processes (Figure 19(c)) that become dominant within distinct applied voltage ranges. The order in which they are observed depends on the energy barrier for the corresponding process, with tunneling being active only at large voltages. Accumulation of the damage originated by the charge carriers transport under the applied field leads to the formation of a percolative path, increase in conductivity, and irreversible damage, eventually leading to dielectric failure. The observed asymmetry in the characteristics is explained by the formation of an asymmetric charge distribution within the oxide as a consequence of the anodization process.

4.1.4 Mott-Schottky Analysis

Figure 20(a) shows the Mott-Schottky (MS) plots (C^{-2} vs. V) for 32 nm and 44 nm thick Al oxide, in the as-anodized condition. Each curve reveals two linear regions, the positive slope being indicative of n-type doping and the negative slope evidencing p-type doping. By scanning the potential to more positive values, depletion is first induced at the O/E interface, and successively at the M/O interface, allowing the examination of both doped regions in the same measurement; the intersection of the two linear regions yields an estimate of U_{fb} . Analogously, Hakiki et. al., performed M-S measurements of passive films on stainless steels and observed two distinct linear regions, which they interpreted as an outer p-type Cr_2O_3 layer and an inner n-type Fe_2O_3 film [91].

The slope of each linear region was used to calculate the dopant density through Chp. 3, Eq. 20, summarized in Figure 20(b). The as-anodized films show a much larger slope for the n-type region, indicating a lower doping concentration, but both interfaces show significant dopant densities both exceeding 10^{18} cm^{-3} across all thicknesses. The dopant densities decrease with increasing thickness, with the 56 nm oxide film measuring almost an order of magnitude lower than the 32 nm film. This reduction coincides with the conduction becoming nearly symmetric for the 56 nm film (Figure 18(a)). The MS analysis supports the assertion of the p-i-n structure in the oxide layer as the cause of the asymmetrical MOM conduction.

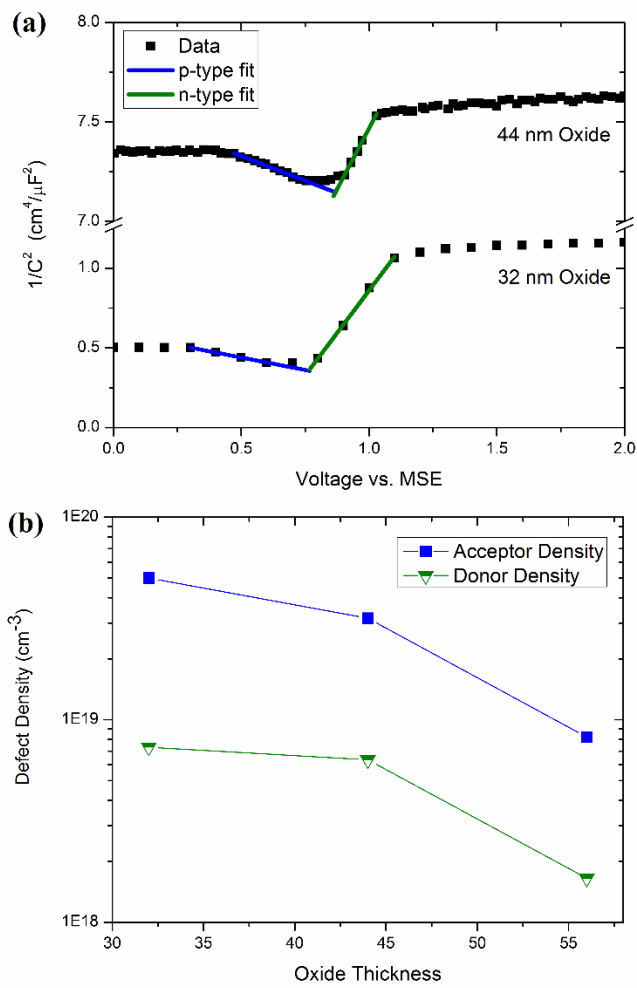


Figure 20: (a) Mott-Schottky plots of as-anodized aluminum oxide films at 32 nm and 44 nm. (b) Dopant density as a function of thickness

4.1.5 Electrolyte-Oxide-Metal Contacts

Current-voltage characteristics for EOM contacts were also recorded for oxide films of different thickness; the corresponding results are shown in Figure 21. It is noted that the asymmetry of the characteristics in this case is even more pronounced than with the MOM contacts.

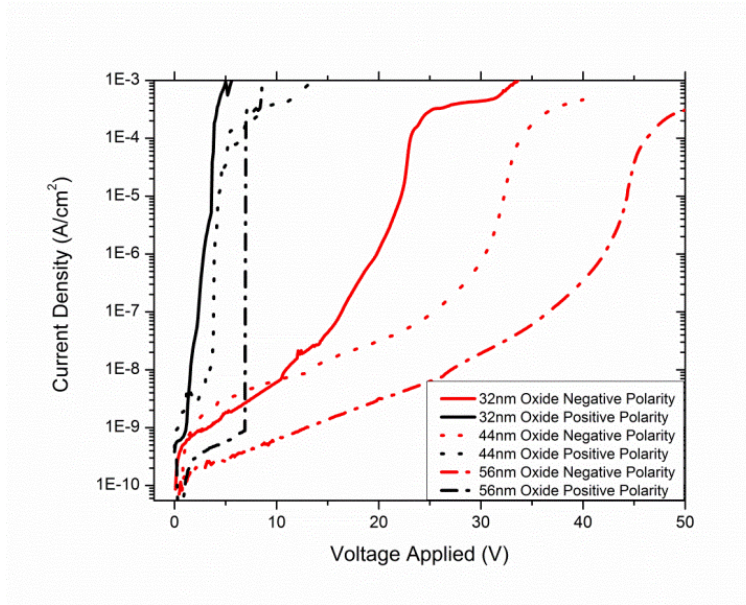


Figure 21: The characteristic I-V curves for Al_2O_3 layers of different thickness. Polarity refers to the voltage being applied to the .05M Na_2SO_4 electrolyte drop, with the ground being the base aluminum layer.

The I-V curve under negative bias reproduces in the low voltage range the trend observed with the MOM contacts; the current density at corresponding voltage however is about two orders of magnitude lower, probably due to the sluggishness of the charge transfer reactions necessary to generate ionic carriers in the electrolyte. Since the current in this region is very small, no significant potential drop is expected within the electrolyte, due to its high conductivity relative to the dielectric. This is consistent with the fact that this section of the characteristics can be fit through a combination of Schottky and PF emission, as shown in Figure 22(a). What are the charge carriers in this potential range? It is hypothesized that spurious oxidation reactions occur at the oxide/electrolyte interface, generating electrons that migrate through the oxide, reaching the base metal. Afterwards, the slope of the I-V curve increases and the sharp breakdown process observed in MOM contacts is replaced by a gradual current increase which eventually approaches saturation. The potential at which the slope increases corresponds closely to the anodization voltage. Taking into account that a negative bias for the EOM contact corresponds to an anodic bias for the oxide, we hypothesize that the observed current in this region is an ionic current I , with the relationship given in (Chp. 2, Eq 10) [42]; the anodization potential therefore roughly separates the potential regions where electronic and ionic conduction dominate, respectively (Figure 22(b)). By triggering ion transport, the high voltage should result in further oxide growth by anodization (Figure 22(c)). This is the process proposed by Dhindsa

et al.[19] to accomplish self-healing of dielectrics during electrowetting operation. The actual growth of the oxide was confirmed by applying a negative bias to a 56 nm thick oxide using an EOM contact, sweeping the voltage up to the saturation region for the ionic current. After rinsing the sample, its thickness was measured by ellipsometry and found to be 57-59nm, 5-8% thicker than before. The oxide thickness increased further when holding the current in the flat I-V region. At even higher potentials (above 40V in Figure 22(b)), an additional increase in current was observed, with concurrent gas evolution; this process corresponds to oxygen formation by water oxidation.

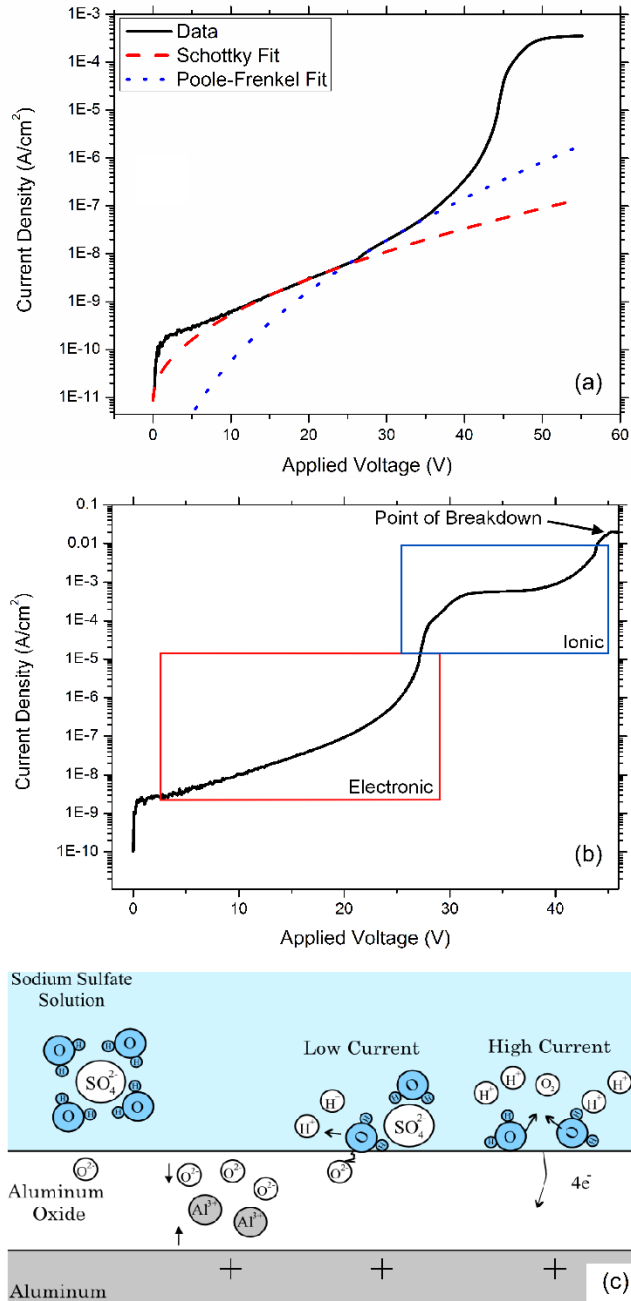


Figure 22: (a) Typical I-V characteristics from a negatively biased EOM contact consisting of a 56 nm of oxide and a .05M Na_2SO_4 droplet as the top contact. The dielectric current leakage models are fitted to the data using Equations 2 and 4 (b) two regions of the negative polarity curve are identified where the electronic and ionic current dominate, respectively; the transition corresponds roughly to the anodization voltage (c) schematic of the oxide/electrolyte interface for the negatively biased system.

The oxide growth and the onset of the breakdown process at negative bias can be monitored by sweeping the voltage on the same sample over several cycles while increasing the maximum applied value. Figure 23 shows the I-V characteristics of an EOM contact with a 38 nm thick oxide, up to the point where ionic current flows and the current saturates (Run 1). The second sweep is run up to the potential region where oxygen is evolved; in this case, the increase in current slope indicating the transition from electronic to ionic conduction occurs at a higher potential, suggesting that a thicker oxide has been formed. The third voltage sweep (Run 3), recorded after oxygen evolution on the electrode has occurred, shows a completely different behavior, with a large current and gas evolution occurring at much lower potentials, below 5 V. The onset of gas evolution cannot be determined precisely, therefore it is difficult to correlate gas evolution and oxide breakdown; qualitatively however it is possible to associate visible gas evolution with a relatively large current, which would trigger anodic breakdown.

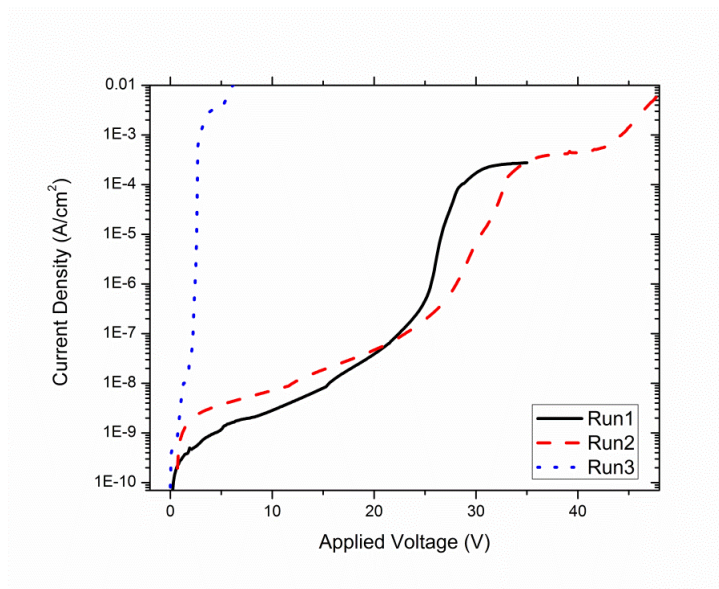


Figure 23: Three consecutive I-V characteristics recorded at a 38nm thick oxide surface using the same .05MNa₂SO₄ droplet for all curves. The curves were run (black to red to blue) immediately following one another without altering the configuration. Oxide thickening is observed between 1 and 2, breakdown between 2 and 3.

4.2 Tantalum Oxide

4.2.1 Oxide Growth

The growth of tantalum oxide starting from a 100 nm film of Ta sputtered on a silicon wafer was initially investigated using a variety of different anodization solutions, including phosphoric acid [92], [93], and sulfuric acid [94], [95], as popular literature solutions. However, similar to aluminum oxide, a 30 wt% ammonium pentaborate in ethylene glycol proved best based on measurements of the onset of breakdown and roughness. The resulting tantalum oxide films were not transparent, and their thickness could not be measured through ellipsometry; therefore, to characterize the thickness of films, x-ray reflectivity (XRR) measurements were used (See Chapter 3.3). Similar to aluminum oxide, oxide films at a variety of anodization voltages were grown in order to obtain a relationship between the anodization voltage and oxide thickness, which is given in Figure 24(b). The XRR technique additionally estimates the roughness of the resulting films, all under 1 nm for both the oxide and substrate. The resulting oxides were amorphous, with an anodization ratio of 1.5 nm/V. The analysis of conduction properties was carried out at the same anodization voltages as aluminum oxide, therefore, the tantalum oxide films are slightly thicker due to the higher anodization ratio for the material system.

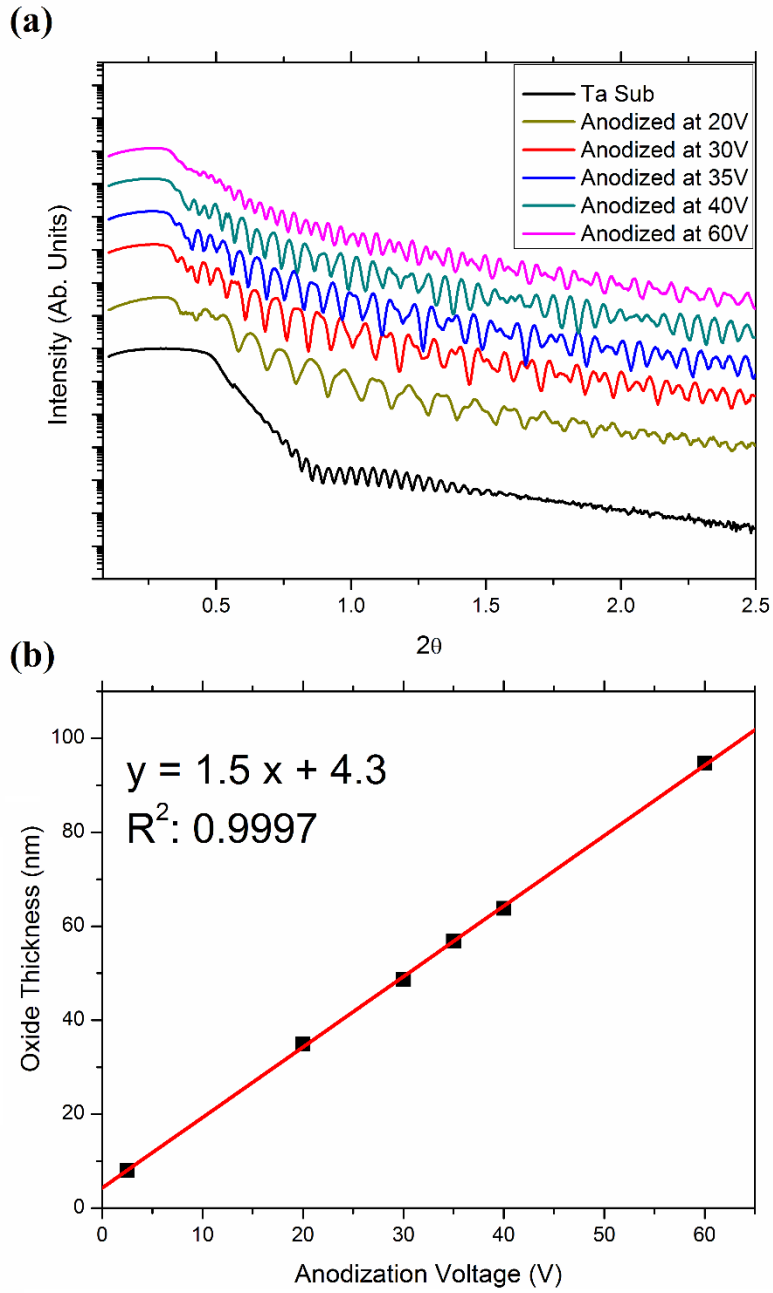


Figure 24: (a) XRR scans of tantalum oxide films ranging from the unanodized substrate to anodization at 60 V with (b) the resulting thickness calculated from (a).

4.2.2 Metal-Oxide-Metal Contacts

The MOM current-voltage characteristics for the anodized tantalum oxide films are given in Figure 25(a) for samples anodized at 20, 30, and 40 V. The current density increased rapidly in these films, with all oxides reaching greater than 10^{-5} A/cm² at a 5 V bias. After the initial current increase the final breakdown shifted to higher values, proportionally to thickness. As seen in the 64 nm film, the final breakdown occurred at very high currents, in excess of 0.1 A/cm². Thicker films proved difficult to measure, with the current reaching the compliance limit in several measurements without actually reaching the point of irreversible breakdown. An interesting feature of these films is the symmetry across polarity, in stark contrast to what was observed in aluminum oxide. The symmetry would suggest that defects concentrations are not as high in these films, which will be further discussed in the Mott-Schottky analysis (Section 4.2.4)

Figure 25(b) summarizes the breakdown voltage and field for each thickness as an average of at least 10 individual measurements with the exception in the 65 nm case, for which only 7 breakdown events could be obtained, due to reaching the compliance limit without breakdown. Therefore, the average breakdown value in the thicker oxides would likely be slightly higher than reported here as any higher breakdown voltage spots could not be included in the analysis. The breakdown field remained slightly above 3 MV/cm for both polarities regardless of thickness. The error bars are used to set the range to indicate the highly variable nature of breakdown in these films. This finding is consistent with what has been observed in similar tantalum oxide films during MOM measurements, with typical values ranging from 2.2 – 4 MV/cm [96]–[99].

In comparison to the aluminum oxide MOM breakdown characteristics (Figure 18(a)), significantly higher current and lower breakdown field are always universally observed. The trend in current density is consistent with the difference in band gap (see Figure 2); the lower band gap for tantalum oxide than aluminum oxide results in higher currents.

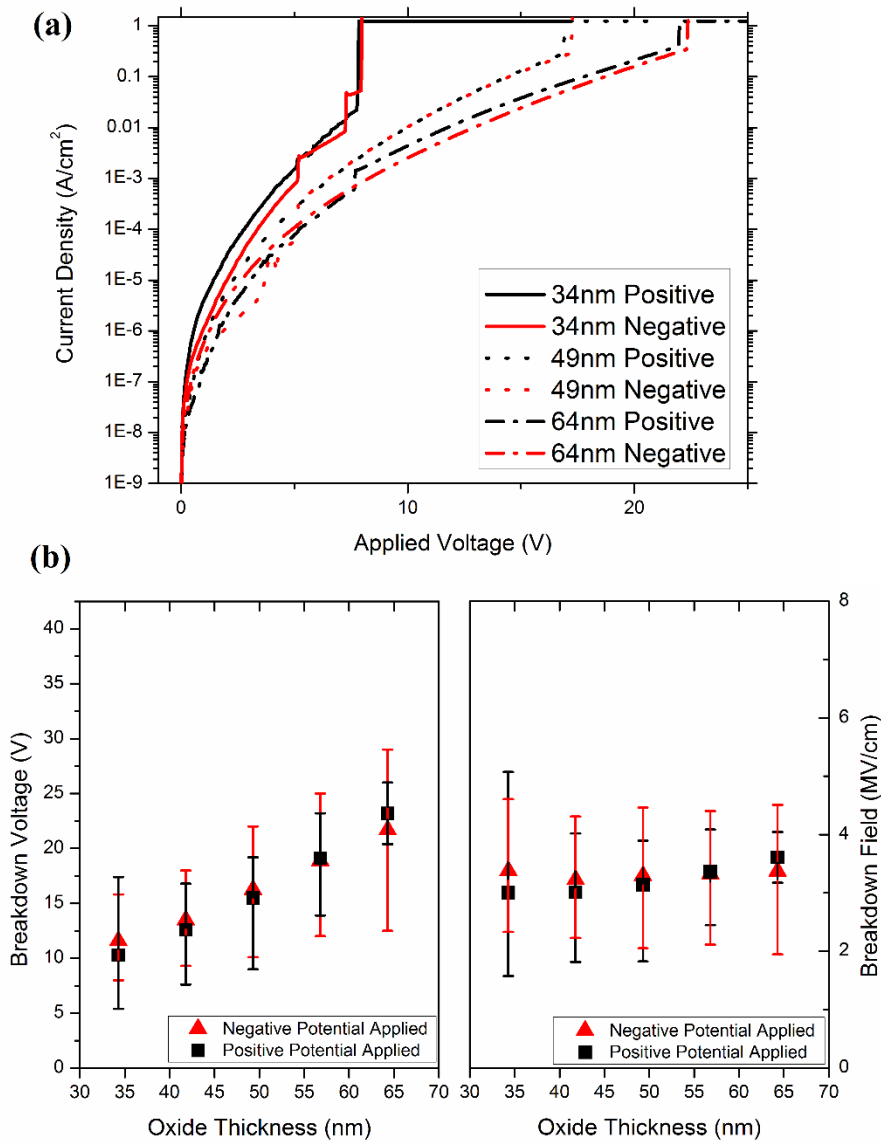


Figure 25: (a) I-V characteristics for tantalum oxide films of various thickness in a metal-oxide-metal configuration operating under both polarities (b) Breakdown voltage V_B and breakdown field E_B vs. film thickness for positive (black, square) and negative (red, triangle) polarity applied to the top contact. The error bars represent max and min values for the data scatter with the average value as the data point.

4.2.3 Electronic Processes

The anodized tantalum oxide films are amorphous and exhibit the conduction mechanisms discussed in Chapter 2.4, similar to those of Al oxide. As originally suggested by Frenkel [100], the potential barrier for thermoelectric emission at bulk defects is related to the dielectric constant of the material. As a result, the higher dielectric constant of tantalum oxide, $\epsilon_r = 25$ (confirmed in section 4.3), has a lower barrier to emission and therefore higher currents than what was seen in aluminum oxide. As shown in the MOM current measurements, the symmetry between polarities suggests that interfacial defect densities do not play a significant role for these films. Oxygen vacancies have been observed as the primary defect for the bulk conduction mechanisms in tantalum oxide films [101], [102], closely tied to the energies observed for Poole-Frenkel conduction [103].

Figure 26 shows the fit of conduction mechanisms to the current-voltage data for a 42 nm thick tantalum oxide layer. The total current was modeled as a combination of Schottky (Chp 2, Eq. 11) and Poole-Frenkel conduction (Chp 2, Eq. 13). The change in the conduction mechanism is noticed in the abrupt change, with roughly an order of magnitude increase in current. The change in mechanism was far from consistent across thicknesses, with no trend in thickness nor polarity. For example, as shown in Figure 25(a), the 64 nm curve under positive polarity, as well as those for 34 nm and 49 nm thickness under negative polarity, exhibit a change in conduction mechanism, but the other measurements only show a Schottky current. Out of the roughly 10 measurements per thickness, 3-5 measurements showed both conduction mechanisms, while the others did not. In contrast to AlO_x , no tunneling current was ever observed, likely due to breakdown occurring prior to the occurrence of barrier thinning (see Chapter 2, Figure 8(b)) to the length scale needed for tunneling.

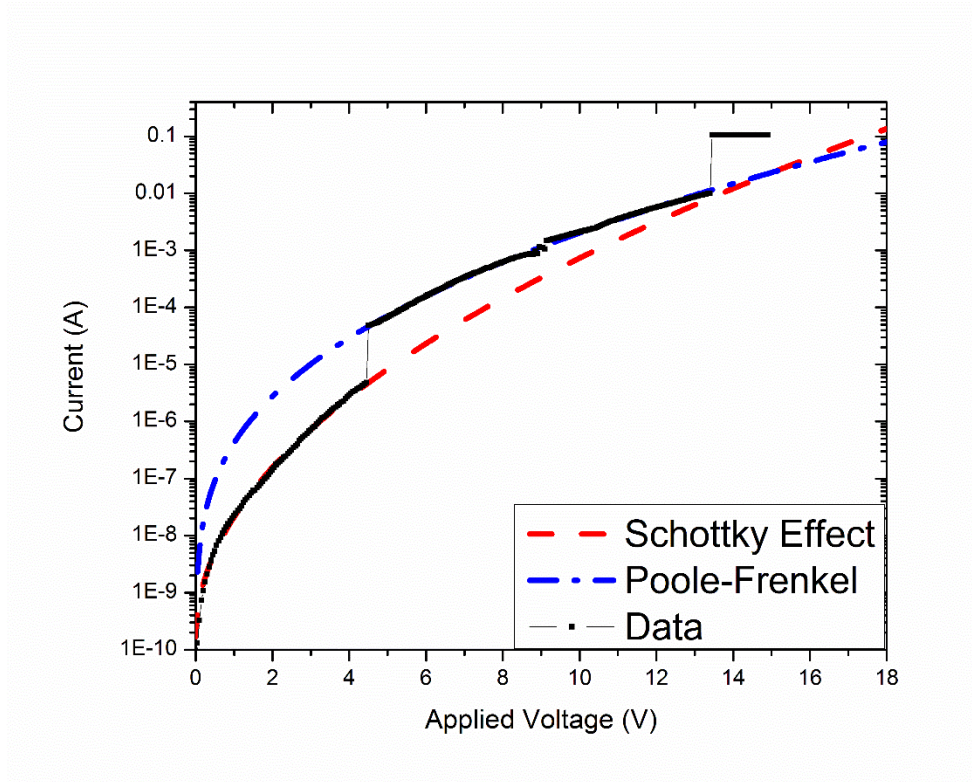


Figure 26: Fit of the experimental I-V characteristics of a 42 nm thick Ta oxide film to a combination of dielectric leakage mechanisms; each process in turn is assumed to dominate conduction in the voltage region where the corresponding characteristics applies: Schottky Emission (Red), Poole-Frenkel (Blue)

4.2.4 Mott-Schottky Analysis

Figure 27(a) shows the Mott-Schottky data for a 64 nm tantalum oxide film; only a positive slope is observed, indicating n-type doping. Tantalum oxide is indeed commonly known as an n-type semiconductor, with oxygen vacancies being the dominant defect [104], [105]. In contrast with aluminum oxide where metal and oxygen ion transport numbers are relatively close, tantalum oxide shows a metal ion transport number averaging around 0.3 [106], which results in excess oxygen vacancies at the metal/film interface. The calculated donor density for thicknesses of 34, 49, and 64 nm (Figure 27(b)) is roughly $7 \times 10^{16} \text{ cm}^{-3}$, several orders of magnitude lower than both the interfaces in aluminum oxide (Figure 20(b)). The flat band of -0.9 vs. MSE agrees very closely to the value of -0.95 V vs. MSE obtained in a photoelectrochemical study [107].

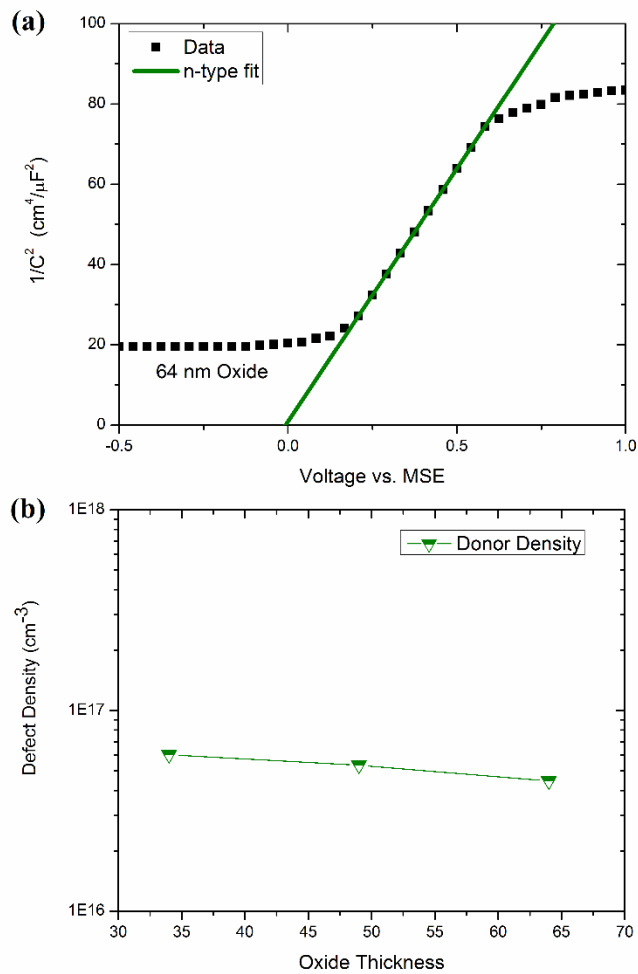


Figure 27: (a) Mott-Schottky plot of 64 nm tantalum oxide (b) summary of donor densities for 34, 49, and 64 nm oxides

4.2.5 Electrolyte-Oxide-Metal Contacts

The I-V characteristics for tantalum oxide using an EOM configuration is given in Figure 28, showing a strongly asymmetric current in the opposite polarities. The results are nearly identical to those for the aluminum oxide system with the oxide layer under cathodic polarization showing very little resistance to current flow. Hard breakdown and gas evolution occur at or below 5 V bias in all cases with little additional resistance observed at increased oxide thickness. The oxide layer is very stable under anodic polarization, with only electronic leakage current evident prior to the anodization

voltage. Exceeding the anodization voltage initially causes further oxide growth, followed by irreversible gas evolution. The tantalum oxide film thickness can also be estimated by the change in color. The measurements that induce further oxide growth upon exceeding the anodization voltage, show a uniform color change on the entire drop contact area.

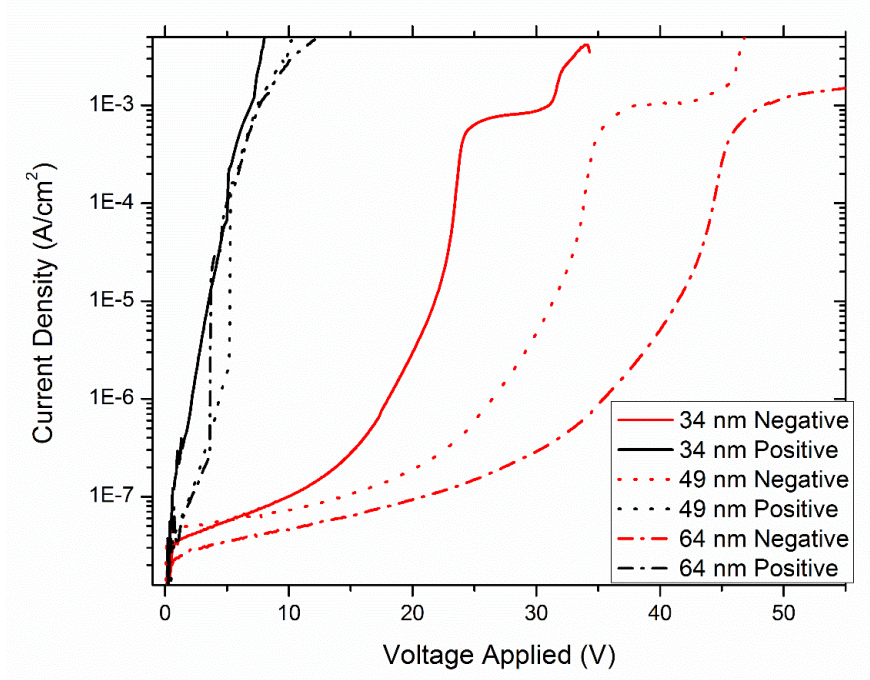


Figure 28: The characteristic I-V curves for tantalum oxide layers of different thickness. Polarity refers to the voltage being applied to the .05M Na_2SO_4 electrolyte drop, with the ground being the base tantalum.

Both aluminum and tantalum oxide in the EOM configuration follow the same behavior, with the oxide layer under anodic polarization. These measurements simulate an electrowetting measurement only on the oxide layer, with no significant contact angle change due to the low initial contact angle and high hysteresis surface. Under this configuration, it is clear that both systems allow for EWOD operation under the anodization voltage. Figure 29 shows the direct comparison of both oxides anodized at 20, 30, and 40V. The leakage current given by the electronic conduction mechanisms is significantly higher in the tantalum oxide system, which could negatively affect the long term performance during EWOD performance. The current converges at the anodization voltage, followed by gas evolution in both layers.

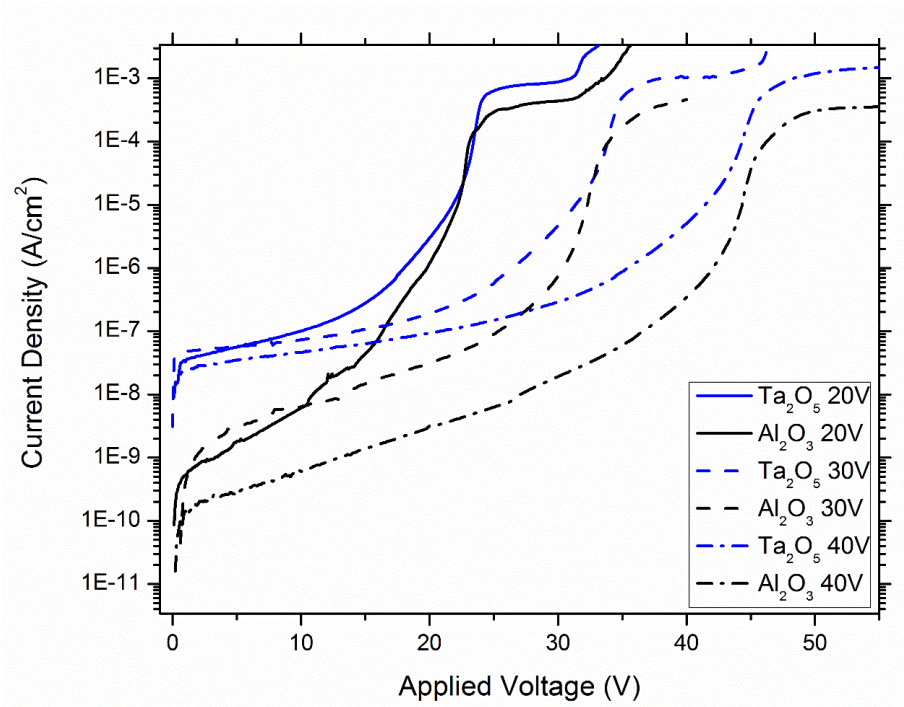


Figure 29 : Comparison of EOM I-V characteristics for tantalum and aluminum oxide under anodic polarization.

4.3 Dielectric Constant Determination

Solid state capacitance measurements were performed using the same configuration as the I-V measurements during the MOM evaluation. Varying both frequency and voltage, the system capacitance is measured, which is then transformed to dielectric constant values using the thickness of the layer and the area of the contact. Figure 30 presents the dielectric constant determination for both tantalum and aluminum oxide anodized at 30 V, 46 and 44 nm, respectively. The aluminum oxide dielectric constant values ranged between 8.87 and 9.11, with an average of 8.96, very close to the commonly used literature value of 9 [23]. Tantalum oxide showed more variation in comparison, ranging between 23.9 to 26.5 with an average value of 24.9. The higher dielectric constant values were measured at high frequency. The literature values of tantalum oxide show significantly variability, typically due to the use of different fabrication methods. Specifically looking at anodized tantalum,

values range between 18.5-30.2 [104], [108]–[110]. The capacitance was similarly characterized for different thicknesses of oxide in both systems, but showed slight to no difference in dielectric constant values, except for very thin layer (>10 nm) that are outside the scope of this work.

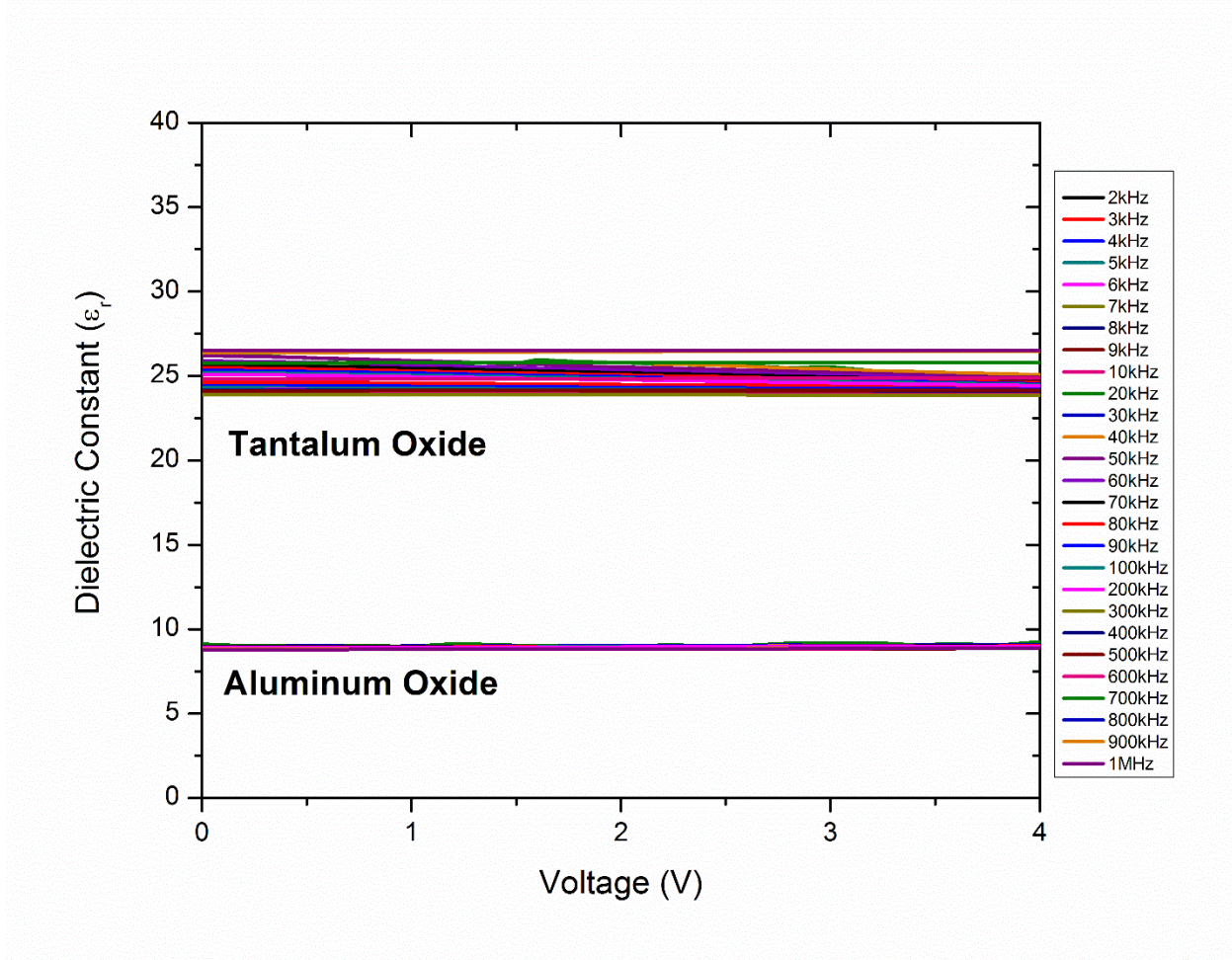


Figure 30: Dielectric Constant of aluminum and tantalum oxide films anodized at 30 V reaching a thickness of 44 and 46 nm, respectively.

4.4 Conclusions

The characteristics of metal oxide films for electrowetting systems were investigated using solid-state and electrolytic configurations. Both tantalum and aluminum oxide produced consistent amorphous oxide films through anodization of smooth metal substrates. The electronic leakage could be assigned to both Schottky and Poole-Frenkel emission, while aluminum oxide also showed Fowler-Nordheim tunneling at high voltage. The solid-state breakdown polarity dependence was a function of the interfacial defect densities generated during the anodization process; aluminum oxide results in the formation of a p-i-n junction, creating a strong polarity dependence that decreased with increasing

oxide thickness. In contrast, tantalum oxide showed n-type defects at low densities, causing no detectable polarity difference during MOM measurements.

Both systems performed nearly identically upon electrolytic conduction under anodic polarization, with the leakage current being determined by electronic mechanisms under the anodization voltage, followed by oxide growth and gas evolution. The primary difference between the metal oxides is the significant increase in leakage current prior to the anodization voltage for the tantalum oxide. Cathodically, both layers fail rapidly with gas evolution under 5 V, limiting operation to a single polarity.

Under EWOD operation, both systems provide a stable dielectric layer as long as operation occurs under anodic bias and below the anodization voltage. The information provided throughout this chapter will enable a better understanding of performance during EWOD measurements.

Chapter 5

Hydrophobic Layer Formation

Part of chapter reproduced from:

M. Mibus, X. Hu, C. Knospe, M. L. Reed, and G. Zangari, “ Octadecylphosphonic Acid Self-Assembled Monolayers in Low Voltage Electrowetting-on-Dielectric Systems,” *ECS Trans.*, vol. 61, no. 2, pp. 325–331, May 2014.

5.1 Overview

As evident through the discussion in Chapter 2 and 4, significant emphasis in this work is placed on the dielectric oxide layer. The oxide in fact serves as both the primary insulator and due to its high dielectric constant, can greatly affect the voltage dependence in EWOD. However, as the oxide layer becomes thinner, reaching the 30 – 60 nm range of films analyzed in Chapter 4, the oxide capacitance increases and the effect of the hydrophobic layer begins to dominate the EWOD response since the dielectric and hydrophobic layers act as two capacitors in series. The equivalent capacitance is given by Eq. 25:

$$C_{Total} = \left(\frac{t_{oxide}}{\epsilon_0 \epsilon_{oxide}} + \frac{t_{polymer}}{\epsilon_0 \epsilon_{polymer}} \right)^{-1} \quad \text{Eq. 25}$$

Three hydrophobic materials are discussed in this chapter: a commercial fluoropolymer Cytop, and two self-assembled monolayers, phosphonic acid and silane; their chemical formation and deposition methods are summarized in Figure 31. Cytop is spin coated and dried, while the latter two materials are assembled through solution methods. The formation process of the three materials is investigated and the sessile contact angle as well as contact angle hysteresis (CAH) characterized. The scope of the characterization is limited to (i) the achievement of reproducible fabrication with (ii) high initial water contact angles that (iii) do not hinder movement of the drop contact line for EWOD measurements.

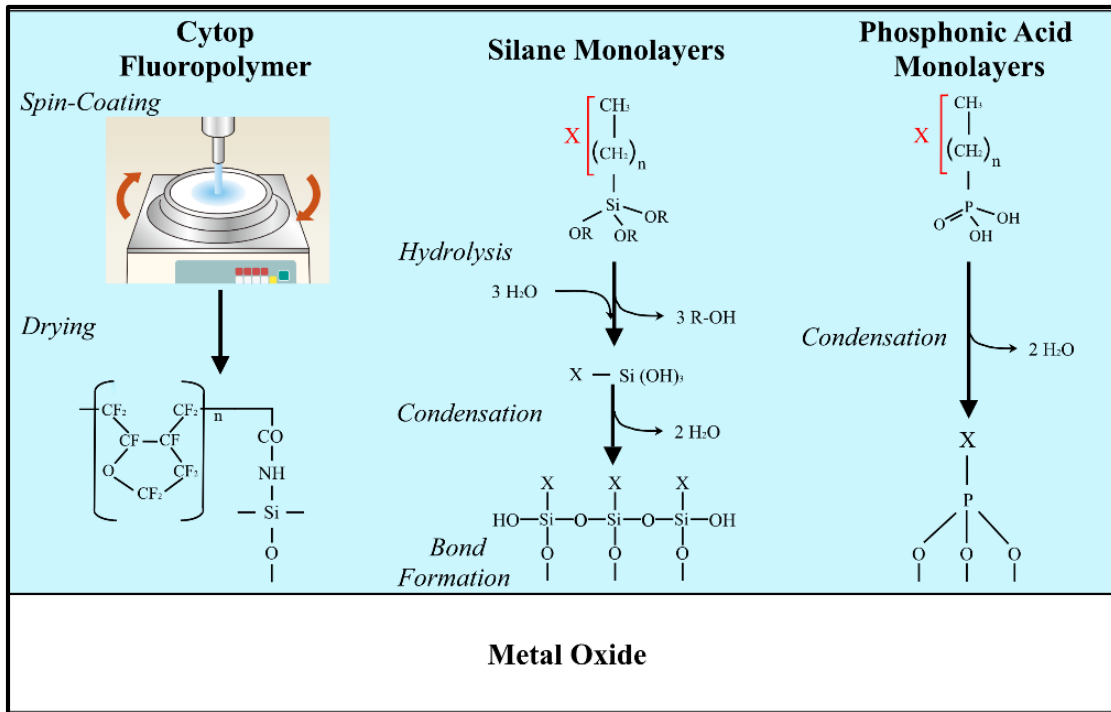


Figure 31: Summary of hydrophobic layer formation

These three described criteria can be easily met by applying polymer coatings (think Teflon on a pan) through dip or spin coating at thicknesses of several hundred nanometers to micrometers. However at this thickness, any advantage in EWOD generated from the metal oxide layer would be negligible. Figure 32, shows the L-Y curves (Eq. 6) using different hydrophobic layers, with properties of Cytop as the polymer layer with thickness of 400 and 30 nm chosen to highlight the thickness dependence. Fluoropolymers and conventional SAMs have a similar range of dielectric constants (1.8-2.2), but the SAM coating results in a dramatic decrease in the thickness of the layer from 30 nm polymer to approximately 2 nm. Assuming the same initial contact angle, the SAM addition minimally increases the contact angle-voltage dependence (red) from the expected dependence from an oxide only dielectric (in black), allowing for the performance of the high-k dielectric material to be the determinant of EWOD operation, rather than the hydrophobic layer. The work described in this chapter is to fabricate

hydrophobic layers that allow for EWOD satisfying the three outlined criteria at minimal thicknesses so that the metal oxide layer can enhance device performance.

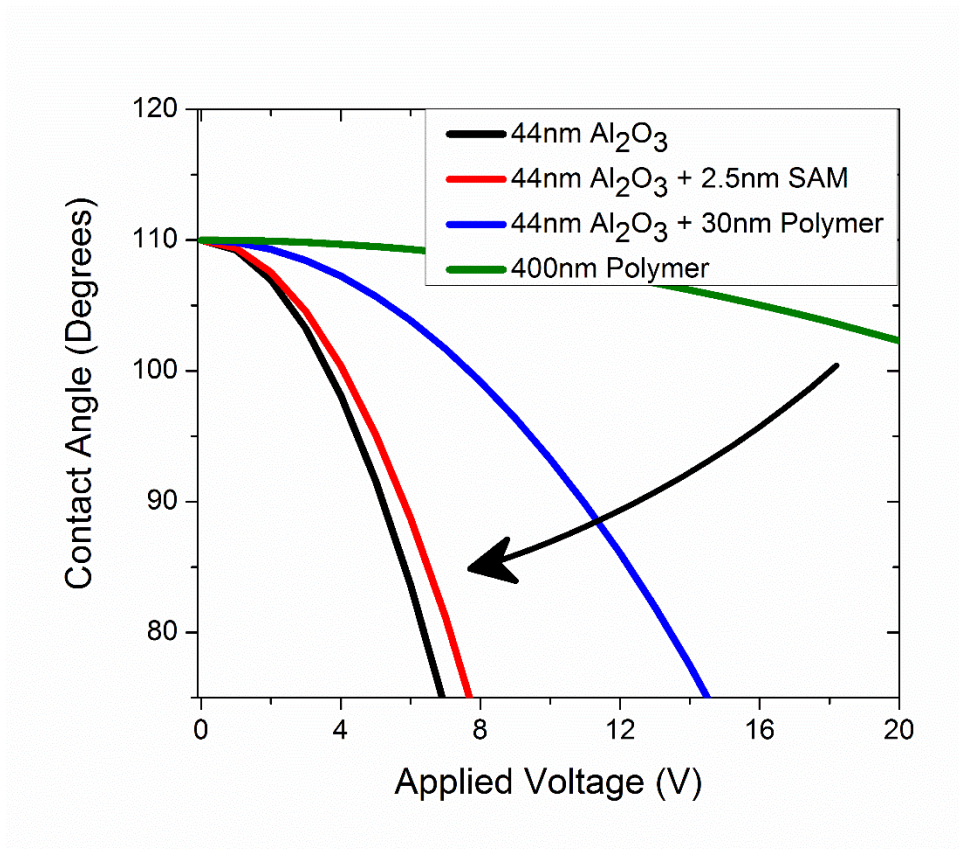


Figure 32: Simulated Lippmann-Young relationship using different thickness combinations of aluminum oxide and hydrophobic materials

5.2 Cytop

5.2.1 Synthesis

Developed by the Asahi Glass Co., Cytop is a completely amorphous perfluorinated polymer with the advantage of transparency and solubility. Cytop has become one of the most widely used hydrophobic surfaces in EWOD, due to easy formation and stable dielectric properties. The solubility in perfluorinated solvents proves to be a key feature and part of the wide spread popularity, as the layer can simply be spin coated, providing a simple method to reproducibly control thickness down to tens of nanometers. The polymer is available with different end groups, selected to achieve optimal bonding on the substrate of interest. We use an amidosilyl end group to attach to inorganic substrate materials, pictured in Figure 31.

Cytop is diluted from a stock solution, followed by spin coating, and drying. The exact conditions for the different films used within this work are as follows: Cytop CTL-809M was diluted to 0.5 wt% using CT-Solv. 180 (Asahi Glass Co) and spin coated at 2000rpm for 30s and then baked for 1 hr at 130°C to form a 23nm thick film. In order to obtain thicker layers, multiple spins of the solution were necessary. As an example, 2 wt% CTL-809M was spun for 30s at 2000 rpm, then baked at 90°C for 15 min followed by a second 30s, 2000 rpm spin and by baking at 160°C for 60min, resulting in a 210nm Cytop layer.

As described in Figure 32, the thickness of Cytop creates a functional challenge to lower the voltage dependence. Lowering the thickness was investigated in order to push down the voltage dependence even further. In Figure 33, more diluted polymer solutions than the recommended 0.5 wt% was used reaching a final thickness of ~10 nm, with Figure 33(a) showing tearing of the polymer layer of ~10 nm over the oxide surface. This 100 micrometer tear was one of many across the substrate, which could probably impact drop wetting. A similar approach was used in a study by electroplating copper onto a cytop + gold substrate. The experiment aimed to easily identify weak spots in the polymer film via pinhole decoration [111], but commonly for thin samples entire regions of bare substrate were exposed, showing lots of electrodeposited copper on the surface, as seen in Figure 33(b). As a consequence, layers of ~20 nm thickness were used as the thinnest reliable Cytop layer that didn't show any obvious discontinuity after fabrication.

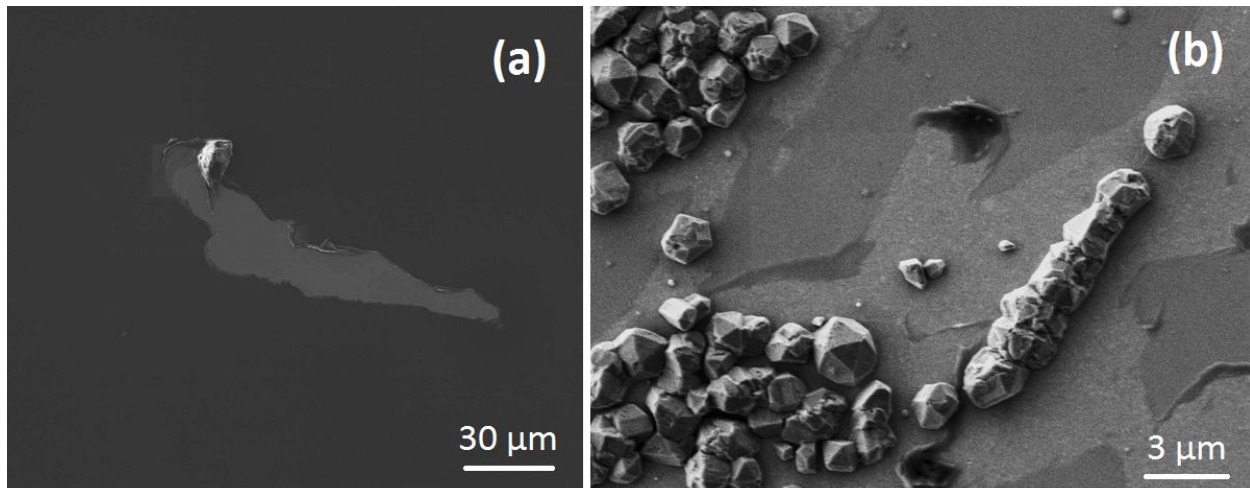


Figure 33: Thin film Cytop layers showing (a) tearing on aluminum oxide and (b) tearing on gold with electrodeposited copper on the bare gold substrate

5.2.2 Contact Angle

One of the primary appeals of Cytop is reproducibility of the contact angle. Under ideal conditions, the surface should exhibit a contact angle of 112° using pure DI water [112]. Throughout the thousands of measurements run within this study, contact angles of aqueous fluids was always between 106 - 112° , barring a defective film.

5.2.3 Contact Angle Hysteresis

CAH measurements are carried out as described by the dynamic contact angle measurements (Section 3.6). Figure 34 shows the force-depth curve for ~ 20 nm cytop on aluminum oxide, dipped into a 0.05 M Na_2SO_4 bath run for 5 cycles. The curve's reproducibility indicates that the solution doesn't modify the surface during measurement. Using Eq. 18 (Chp 3), the average advancing contact angle is 115.7° and the average receding contact angle is 103.5° giving a CAH of 12.2° . The result is typical for a freshly fabricated layer, with values ranging from $9.2 - 15.1^\circ$ considering all dynamic measurements on Cytop, comparable to other Cytop-air systems [113].

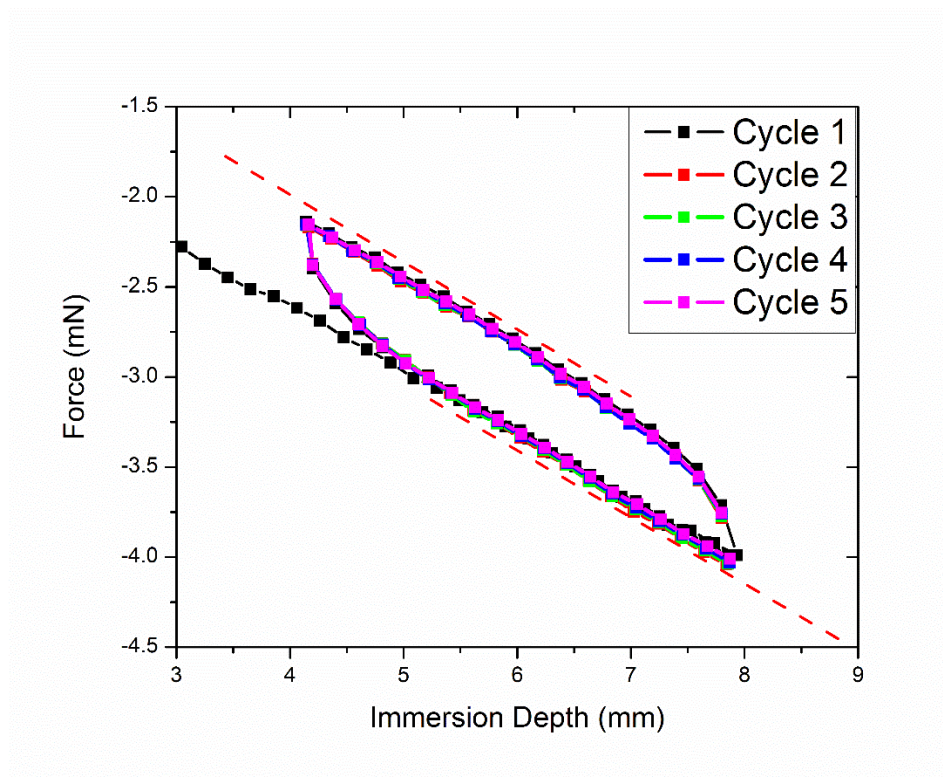


Figure 34: Force-depth curves of 20 nm Cytop film

In summary, Cytop provides an easily formed hydrophobic surface on the metal oxide substrates discussed in Chapter 4. The formation of 20 nm thickness films is highly reproducible without any tearing of the substrate. As will be discussed in detail in Chapter 6, 20 nm Cytop with a 34 nm metal oxide substrate allows for EWOD of 25° in 12 V, a substantial amount of electrowetting. To further lower the contact angle voltage dependence, a different hydrophobic materials is required.

5.3 Self-Assembled Monolayers

SAMs are attractive organic materials due to the widely tunable properties through alteration of specific functional groups. For example, the wetting properties can be altered through the endgroup from hydrophobic when CH_3 -terminated to hydrophilic when OH-terminated.

Preparation of the organic layers is commonly carried out by solution or gas-phase deposition, with the solution process more widely utilized due to ease and lower cost [114]. Solution formation simply consists in dipping a substrate into a bath containing dissolved SAM molecules, typically with μM - mM concentration in an organic solvent, for a certain duration of time, allowing the assembly of a monolayer. The self-assembly process utilizes the chemisorption of the headgroup with a specific

affinity to the substrate. For SAM formation with metal oxide substrates, organosilane and organophosphonic acid have been shown to readily form films [115]–[117], which are the targeted materials for this study.

A tremendous effort to characterize the initial steps of adhesion and layer formation of monolayers has been undertaken in the past by various research groups, particularly with alkanethiols on Au (111) [114], [118], [119]. Silane and phosphonic acid have both been investigated in a number of studies. Most prominently, octadecyltrichlorosilane (OTS) on SiO₂ was one of the first reported SAM structures [120], which underwent a significant amount of study due to their compatibility with CMOS fabrication [121]. Similarly, Schwartz et. al., studied the growth of phosphonic acid monolayers on mica in a series of papers, determining that monolayers form close-packed islands that eventually coalesce into a uniform film [122]–[127]. Both systems have a lot of similarities, with surface attachment by a condensation reaction between the surface hydroxy groups and the hydrolyzed SAM chain occurring in both systems.

5.3.1 Phosphonic acid SAMs

5.3.1.1 Formation and contact angle

Octadecylphosphonic acid (ODPA) layers were deposited on the metal oxide surface by submerging the films in a heated solution of toluene, detailed below. Several different solutions were investigated for delivering the ODPA monomers, varying the solvent from non-polar to strongly polar, the solution temperature, and ODPA concentration. For example, polar solvents such as ethanol readily form aggregates [128], [129] while non-polar solvents tend to form monolayers [130]. However, the fundamental studies of formation by the Schwartz group used tetrahydrofuran, a polar aprotic solvent [123]–[125], [131], [132]. From initially evaluating the range of solvents, toluene repeatedly showed the most promise in initial sessile angle [133]. The film's contact angles were evaluated over various immersion durations to determine the optimum fabrication conditions for use in EWOD measurements. Temperature proved to be key in monolayer formation. Figure 35 shows contact angle vs. time for room temperature, 45°C, and 65°C. Each data point is the average of 10 measurements across the sample, and the error bar indicates the data range.

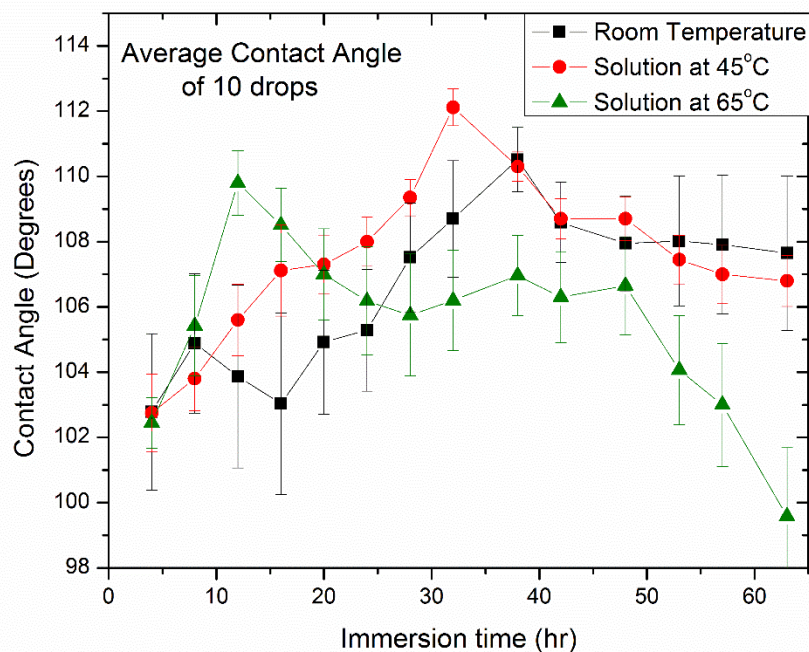


Figure 35: Contact angle vs. Immersion time for 1mM ODPA SAMs formed in Toluene at room temperature (black), 45°C (red), and 65°C (green)

The majority of the EWOD results discussed in Chapter 6 use phosphonic acid formation in 1mM ODPA in Toluene at 45°C as it was by far the most reproducible and consistent condition despite the variability observed in Figure 35. Additionally, discussed in 5.3.1.2, the hysteresis of the layers formed under these conditions almost reached the low values seen with Cytop. The formation follows the mechanism suggested through a simple cartoon in Figure 36 [119]. The generic description follows that adsorbate molecules travel through convective and diffusive transport to the solid-liquid interface with adsorption on the substrate. Islands of disordered adsorbed molecules grow and coalesce into ordered solid-phase islands.

From our observations of ODPA growth, initially at low immersion time, a large amount of scatter exists in the contact angle. As the immersion time increases the scatter in the data is drastically reduced, suggesting a SAM layer of high quality. The samples show the least scatter at highest angles between 28 and 42 hours; with longer immersion times however a decrease in contact angle occurs. The monolayer films likely progress from a disordered state at low immersion times to a continuous

monolayer, to a multilayer configuration with a large amount of stacking at high immersion times, which reduces the contact angle.

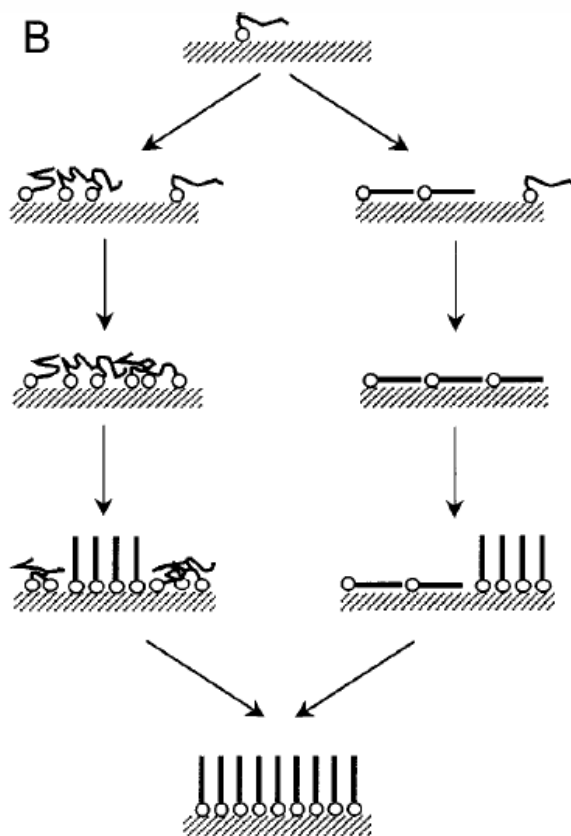


Figure 36: Sketch of SAM formation process progressing from a disordered “lying down” phase to Image reproduced from Ref. [119].

The quality of the monolayer films was assessed using an SEM at low acceleration voltage (500V) for imaging. Low accelerating voltage minimizes the interaction volume of the incident beam, allowing for more pronounced imaging of surface features. The method was used previously at 800 V to identify formation and stacking of phosphonic acid monolayers [134]. At low immersion times the films showed a generally flat surface without any discernable features with the exception of darker patches on the order of 100 μm . Even at low accelerating voltages, with the non-conductive layer, charging of the surface from the beam becomes a problem; therefore, imaging must be done quickly.

Figure 37 shows images of two samples at immersion time of 40 and 60 hours. The low accelerating voltage SEM found stacked regions beginning with 40 hour immersion and increased surface coverage by 60 hours. This was confirmed by energy-dispersive X-ray spectroscopy (EDS) measurements detecting strong Carbon and Phosphorus $K\alpha$ signals, suggesting that these regions are indeed covered by a relatively thick layer of the SAM. The method allows to quickly investigate a large area of the surface, which is very difficult for AFM or other in direct studies such as XRR, which would only give average properties over the entire film.

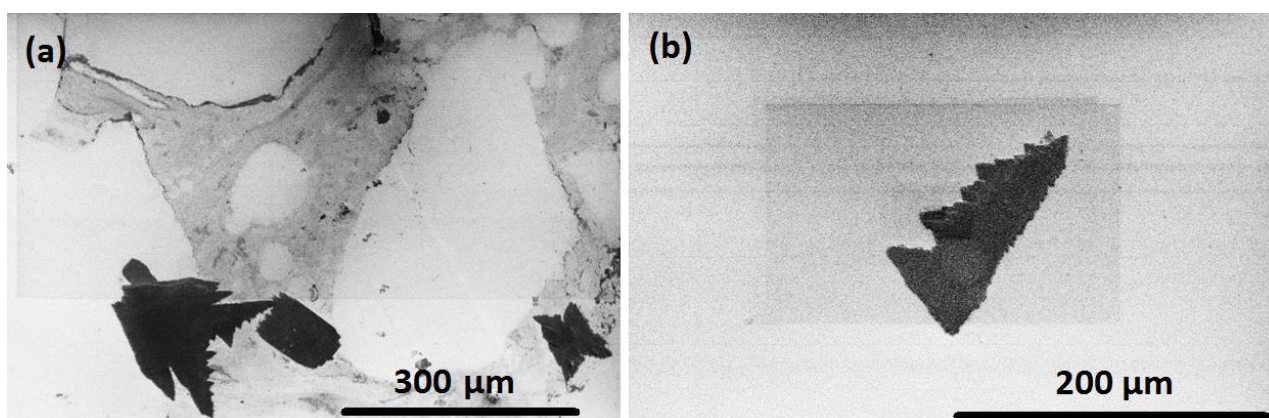


Figure 37: Low voltage SEM of oxide-SAM surface using 1mM ODPA in toluene at 45°C immersed for (a) 60 hours and (b) 40 hours. Dark regions show high C and P EDS signals

The 1mM ODPA 45°C – toluene layer was studied explicitly through XRR measurements. Three immersion times were selected from the contact angle measurements from Figure 35 to analyze the density, thickness, and roughness for each resulting sample. Figure 38(a) shows the complete XRR pattern from the bare aluminum oxide substrate and SAM immersion times of 24, 32, and 40 hrs. The aluminum oxide pattern is initially fitted using the PANalytical software, summarized in Table 1. The very wide Kiessig fringes in the measurement correspond to the titanium adhesion layer of 5 nm with the remaining oscillation being a combination of the aluminum and aluminum oxide layer. The alteration of the XRR pattern with the SAM layer is subtle as the density and thickness of the layer are quite small in comparison to the substrate, but as shown in Figure 38(b), differences can be observed. Each SAM layer was analyzed through careful fitting of each spectra, as summarized in Table 1. Similar XRR studies for pristine monolayers show a thickness of 2.59 nm, similar to the 2.602 nm value found in Table 1 for the 32 hr formation [135]. The results follow what was previously hypothesized. As

immersion time increases the layer transitions from a disordered state, to an ordered layer, finally reaching a multilayer configuration.

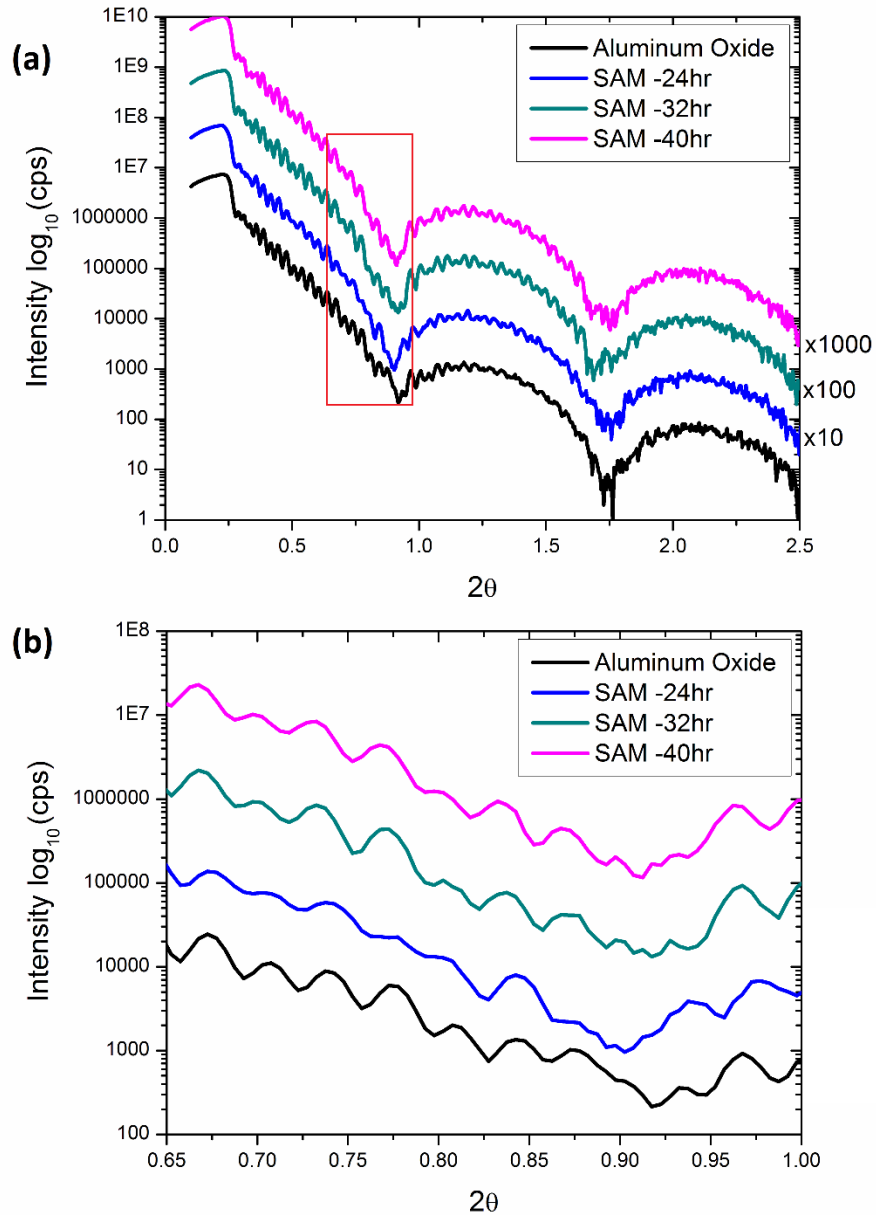


Figure 38:(a) XRR patters for aluminum oxide and various SAM immersion times, as indicated in plot. (b) zoomed in region from (a).

Layer	Density (g/cm ³)	Thickness (nm)	Roughness (nm)
SAM – 40hr	.798	2.928	1.214
SAM – 32hr	.403	2.602	.657
SAM – 24hr	.262	1.832	.722
Substrate Fit			
Al ₂ O ₃	3.1833	43.55	3.514
Al	2.6628	55.14	1.195
Ti	5.5037	5.091	.173
Si	2.231	-	.393

Table 1: Summary of XRR model fitting for 1mM ODPA layers formed in 45°C toluene on 44nm aluminum oxide substrates.

5.3.1.2 Contact Angle Hysteresis

The advancing and receding contact angles were determined through tensiometer measurements for various immersion times using the 1mM ODPA formation in 45°C toluene solution. Each measurement consists in dipping the plate shaped sample into Millipore water as the fluid. Figure 39 shows the dynamic contact angle measurements, with Figure 39(a) and (b) showing the raw force-depth data and (c) the calculated values of CAH. The sample after 4 hours of immersion, Figure 39(a) shows considerable variability throughout the measurement along with advancing angles changing with additional measurement cycles. The disordered layer is difficult to truly analyze through this method as the high variability in contact angle across the sample surface is averaged out as the technique requires to use the slope of the force-depth plot to calculate the advancing and receding angle. The changing position of the curve also indicates that the configuration of the surface is changed from the DI water bath.

The CAH for each surface is summarized in Figure 39(c). The disordered surfaces are considerably hysteretic, which should hinder EWOD performance as discussed in Chapter 6.3.1. The best films grown for 32 hours show the lowest hysteresis of $\sim 15^\circ$, still above the 12° observed in the Cytosol system. With additional immersion time and evident monolayer stacking, hysteresis again begins to increase.

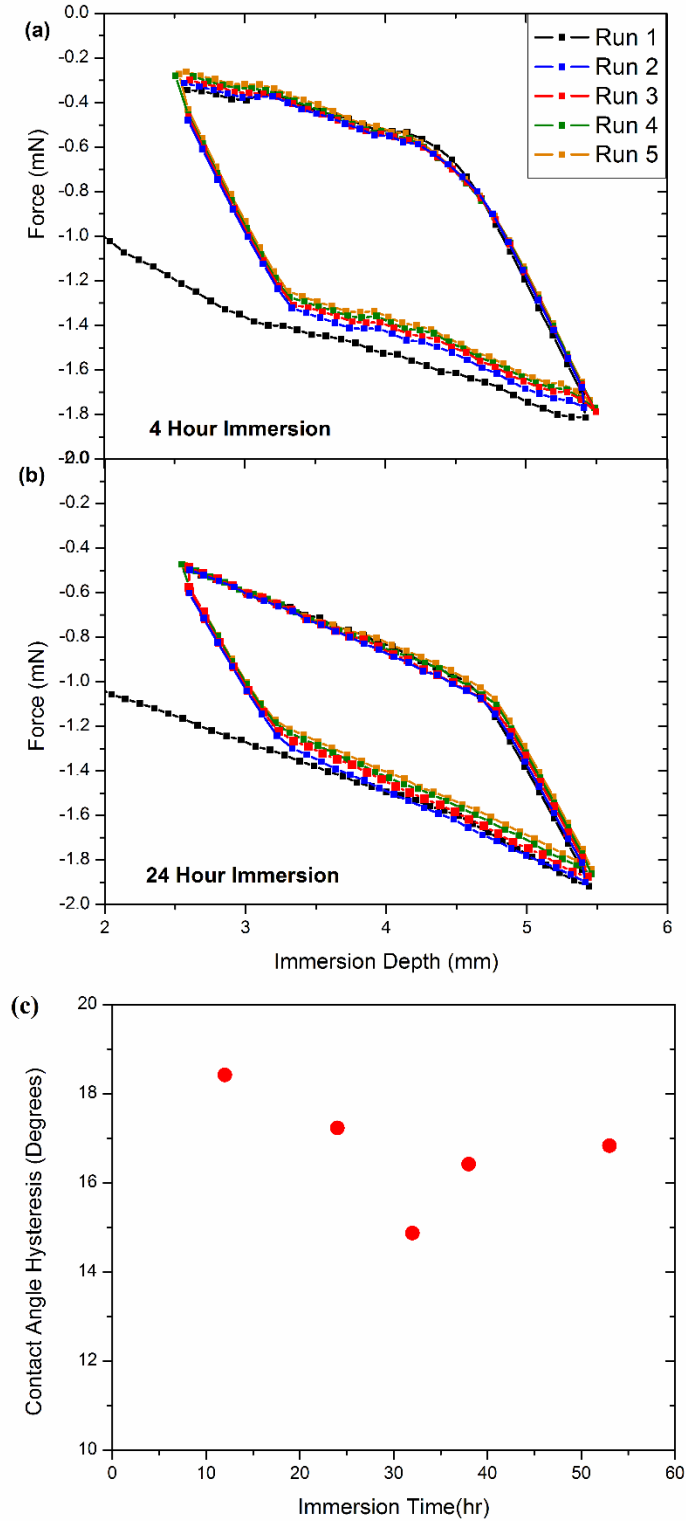


Figure 39: Dynamic contact angle measurements on 1mM ODPA in toluene at 45°C surfaces at various immersion times. (a)-(b) raw force-depth data and (c) calculated CAH values across immersion times

5.3.2 Silane SAMs

5.3.2.1 SAM Formation

Silane SAMs were selected as they also readily attached to metal oxide substrates, with the advantage of providing cross-linking. The ability to cross-link has given very contact angle low hysteresis layers (under 5°) [136], [137] with water contact angles around 110°. It is hypothesized that these cross-linked structures would be more stable to repeated EWOD.

The silanes used in this work are RSiX_3 type materials with X as different head group materials: Cl, OCH_3 , or longer chained alcohols with R as the molecular chain. Formation on the surface follows a three step mechanism for attachment [130], schematically shown in Figure 31. First, the organosilanes react with water or hydroxide through a hydrolysis reaction to create hydroxysilane (RSi(OH)_3). The water for reaction can either be on the surface of the oxide surface or added in 3:1 ratio to the SAM concentration. This step is vital to producing high quality layers, leading to either excessive or incomplete hydrolysis leading to polymerization in solution or incomplete monolayers, respectively [138], [139]. The reactivity of the head group also plays a key factor, with chloride being more reactive than the alkoxy groups. In the second step, the SAMs are aggregated by hydrogen bonding with the oxide surface and laterally ordered by van der Waals forces between chains. Lastly, the hydroxysilane reacts with the oxide surface through a condensation reaction with the surface and cross-linking with neighboring silanol groups producing many covalent bonds with the underlying oxide surface [130].

The formation of high quality silane films proved to be very difficult. Initially trimethoxy(octadecyl)silane was studied but the reactivity of the methoxy head group proved to be insufficient in the hydrolysis step for consistent layer formation. Next, trichloro(octadecyl)silane (OTS) was studied, greatly increasing the reactivity of the hydrolysis step so that the solution showed self-polymerizing in air over hours. Fadeev et. al, show that the wide variation in reactivity of silane SAMs may occur in absence of precise control of the solution/environment [140]. All the films formed in solution in an atmospheric laboratory environment proved to be both inconsistent and highly hysteretic (seen in Figure 45(a)). The main issue with SAM formation was that the films had robust sessile contact angles, all above 105°, but had such high CAH that drop motion was pinned under 5-10 V bias during EWOD evaluation. In order to consistently grow high quality SAMs, the preparation and formation of OTS SAMs had to be undertaken in a glove box under an inert atmosphere.

The exact procedure for the preparation of OTS SAMs was as follows. Glasswear and samples were cleaned by plasma cleaning prior to placing the materials in the glove box. The system was flushed

with high purity Ar, monitoring with a relative humidity meter, until the environment was inert. Next the OTS material was syringed from the as-purchased bottle to a beaker of anhydrous toluene at 2% (v/v). The solution was cooled by placing the OTS-toluene beaker into an ice bath. Ordering during OTS formation has been shown in several studies to be highly temperature dependent [119], [141]–[144]. Figure 40 shows the alkyl chain length dependence on monolayer order with solution temperature [141], which for the 18 carbon atom OTS SAM has a transition temperature at roughly room temperature. Once the OTS-toluene solution was chilled, the metal oxide substrates were placed in solution for various immersion times. The sample was then removed at the specified time, rinsed with toluene to remove any excess materials on the surface, and then dried on a hot plate, all still under inert atmosphere. This formation condition showed the most consistent results and is studied from hereon.

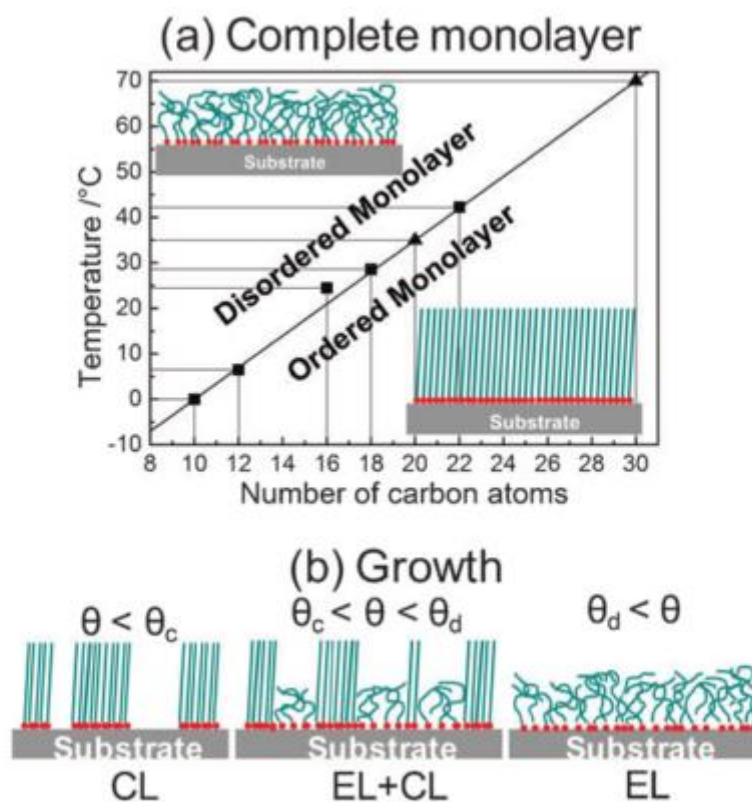


Figure 40: Temperature vs. alkyl chain length for molecular conformations in final monolayer [143].
Image from Ref. [141].

A series of AFM and low voltage SEM images for different immersion times on tantalum oxide were acquired to further understand the optimum conditions for film formation. Unlike ODP, a contact angle, didn't provide much insight into the quality of the surface. The layer forms rapidly with contact angle increasing from the nearly complete wetting on the oxide substrate to greater than 105° within 5 min. Figure 41(b), shows the AFM of a surface immersed for 5 min. The surface shows very minimal height variation with a z-scale of only 1.1 nm, compared to the tantalum oxide substrate (Figure 41(a)) with an image height scale of 1.6 nm. The SEM imaging couldn't pick up any feature for this low immersion time.

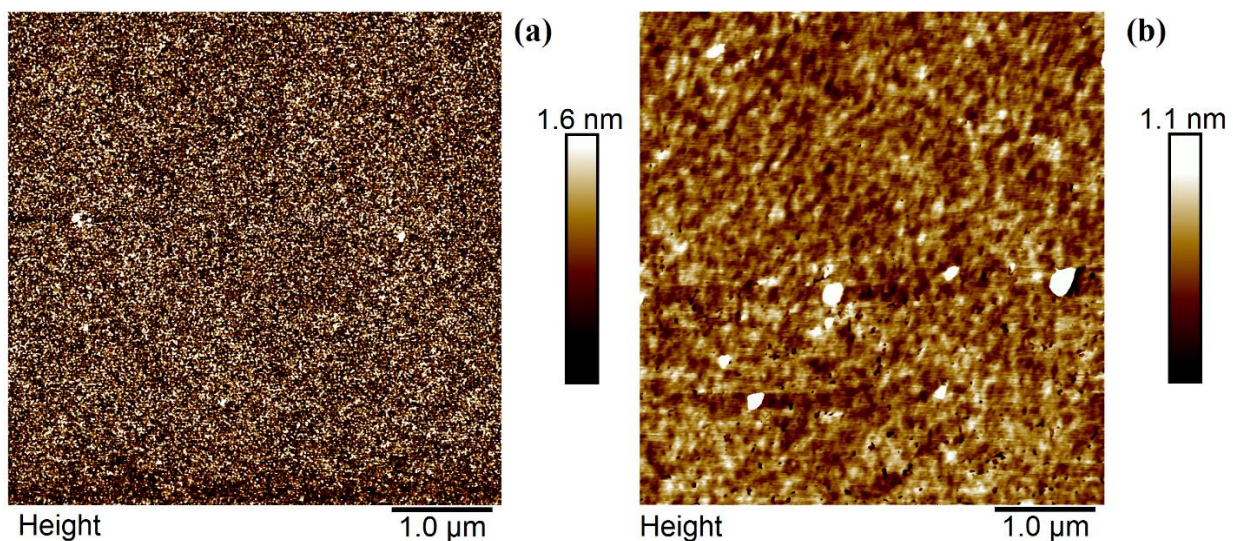


Figure 41: AFM image of (a) 44 nm tantalum oxide substrate and (b) 5 min immersion of 2 (v/v) OTS in toluene on 44 nm tantalum oxide

With increasing immersion time, the surface begins to show features in the SEM and AFM measurements. Figure 42 shows SEM and AFM for 1 hour immersion. The SEM image (Figure 42(b)) at the micron length scale shows generalized accumulation of excessive silane material attached to the surface. AFM scans (Figure 42(a)) didn't capture some of the larger formations observed in SEM, but showed more surface material with height increasing to 6 nm from the ~ 1 nm initial difference.

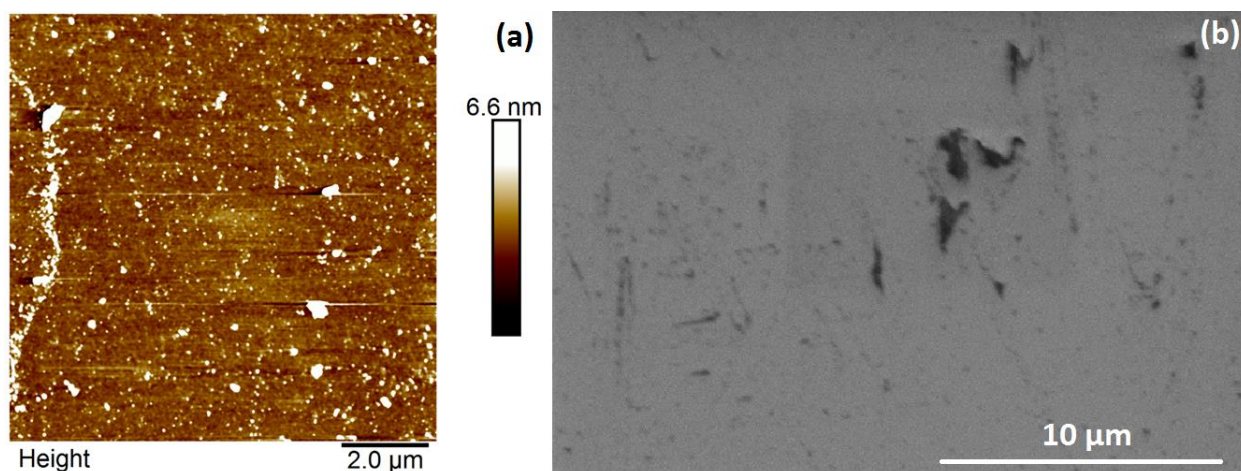


Figure 42: (a) AFM image and (b) SEM image of 60 min immersion of 2 (v/v) OTS in toluene on 44 nm tantalum oxide

By two hours of immersion time the surface became discolored, showing white spots. It has been hypothesized that these white regions are unreacted silane groups [140]. Imaging of the surface showed considerable accumulation of material. Figure 43(a)-(b), shows SEM images at different magnifications of the surface with significant coverage of carbon rich material. The corresponding carbon k-alpha signal is shown in Figure 13 (d) in teal matching the dark material in the SEM image. Finally, AFM scans (Figure 43 (c)) of the surface showed extreme height variation of over 140 nm. The highly disordered layer with variable topography causes significant hysteresis (see Figure 45), and should limit contact angle change at low voltage (as covered in Section 6.4.1).

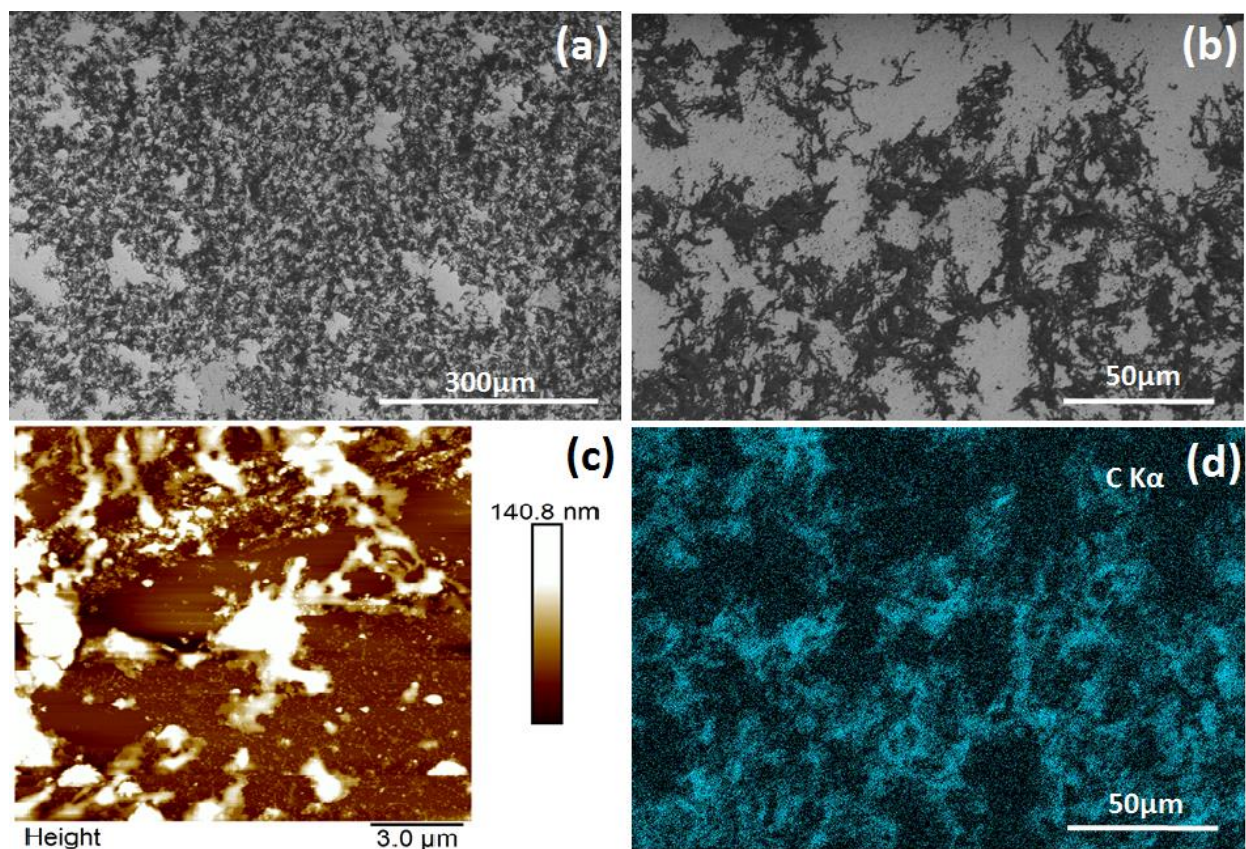


Figure 43: (a) and (b) SEM images at different magnifications and (c) AFM image of 120 min immersion of 2 (v/v) OTS in toluene on 44 nm tantalum oxide

XRR analysis of 30, 60, and 120 min films grown on 44nm anodized tantalum oxide films is shown in Figure 44. The tantalum films did not have an adhesion layer so the Kiessig fringes show similar oscillation frequencies for both the oxide and metal layers. The XRR patterns are dominated at low 2-theta angles by the very dense tantalum layer, which causes only very minor differences as seen in the black box excerpt. However, at 2θ values greater than 1.5° the differences between the films becomes very apparent seen, as in the magenta excerpt. Similar to ODPA, the substrate model is built and then the additional SAM layers are fit, as summarized in Table 2.

With increasing immersion time, the fitting to the data suggests increasing density, thickness, and roughness of the SAM layer. The XRR data are consistent with the AFM/SEM of the layers with higher immersion time increasing accumulation and stacking of silane material. Studies at lower immersion times were unable to show any substantial differences between the materials through the

model fitting. From the XRR evaluation and CAH, discussed in the next section, layers formed from 15 to 45 min were very difficult to distinguish. Previous XRR studies of silane showed thickness of 2.1 ± 0.3 nm with a densities ranging from $0.76 - 0.87$ g/cm³ for complete monolayer formation [145], [146], consistent with what we observe. Higher densities were shown to correspond to incomplete SAM formations [146]. Additionally, the AFM scan of the anodized tantalum oxide substrate showed a RMS roughness of 0.612 nm, the same as found from the XRR measurement.

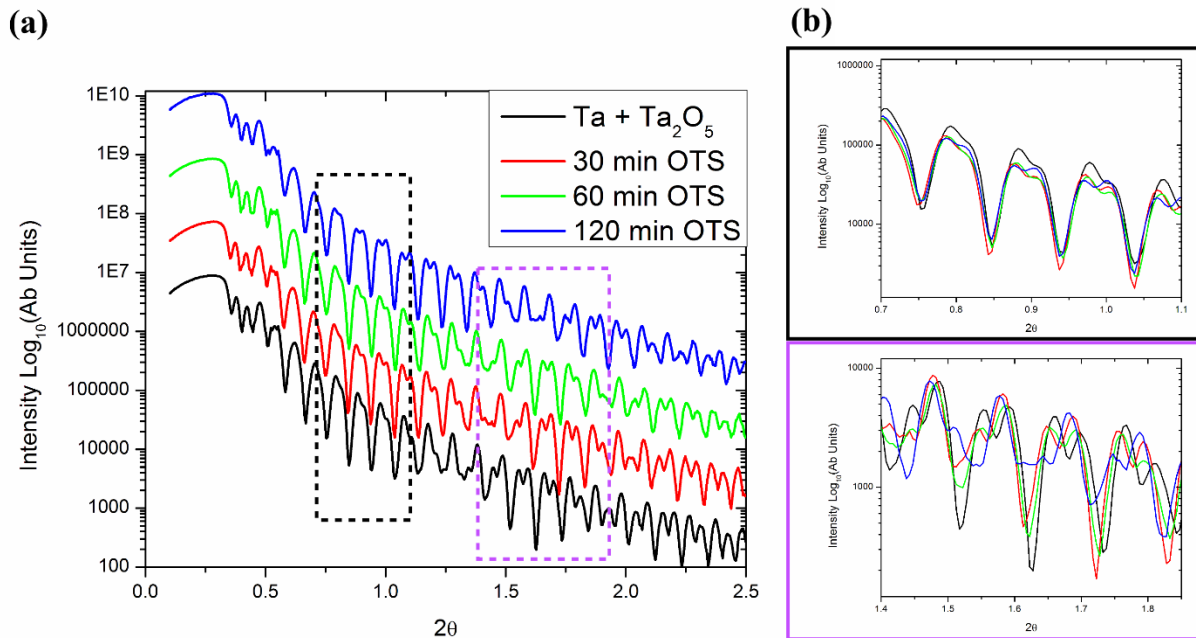


Figure 44:(a) XRR patterns for tantalum oxide and various silane SAM immersion times, as indicated in plot. (b) zoomed in region from (a).

Layer	Density (g/cm ³)	Thickness (nm)	Roughness (nm)
SAM – 120 min	1.12	3.21	2.1
SAM – 60 min	.872	2.60	.823
SAM – 30 min	.765	2.17	.702
Substrate Fit			
Ta ₂ O ₅	7.76	43.4	.568
Ta	16.49	75.5	.26
Si	2.241	-	.292

Table 2: Summary of XRR model fitting for silane monolayers on 44 nm tantalum oxide substrates

5.3.2.2 Contact angle Hysteresis

As previously discussed, the sessile contact angle for these materials was remarkably consistent, showing very hydrophobic values ($> 105^\circ$). However, the dynamic contact angles showed considerable variation with preparation conditions. Figure 45(a), shows the force-depth curve for a surface grown in lab air, and samples grown in the glove box with immersion times of 30, 60, and 120 min in 2 (v/v) OTS-toluene solution under Ar. The results are very linear and do not change with cycle number, suggesting that the layer does reach consistent contact angle and are very stable. The unreasonable hysteresis from the lab air measurement of 53° causes terrible EWOD response, as will be seen in 6.4.2. However, using the inert atmosphere, the hysteresis drops considerably to values of 11° , comparable with standard Cytop values. With increasing immersion time the hysteresis increases for these samples with the very rough 120 min layer showing a CAH of 25° .

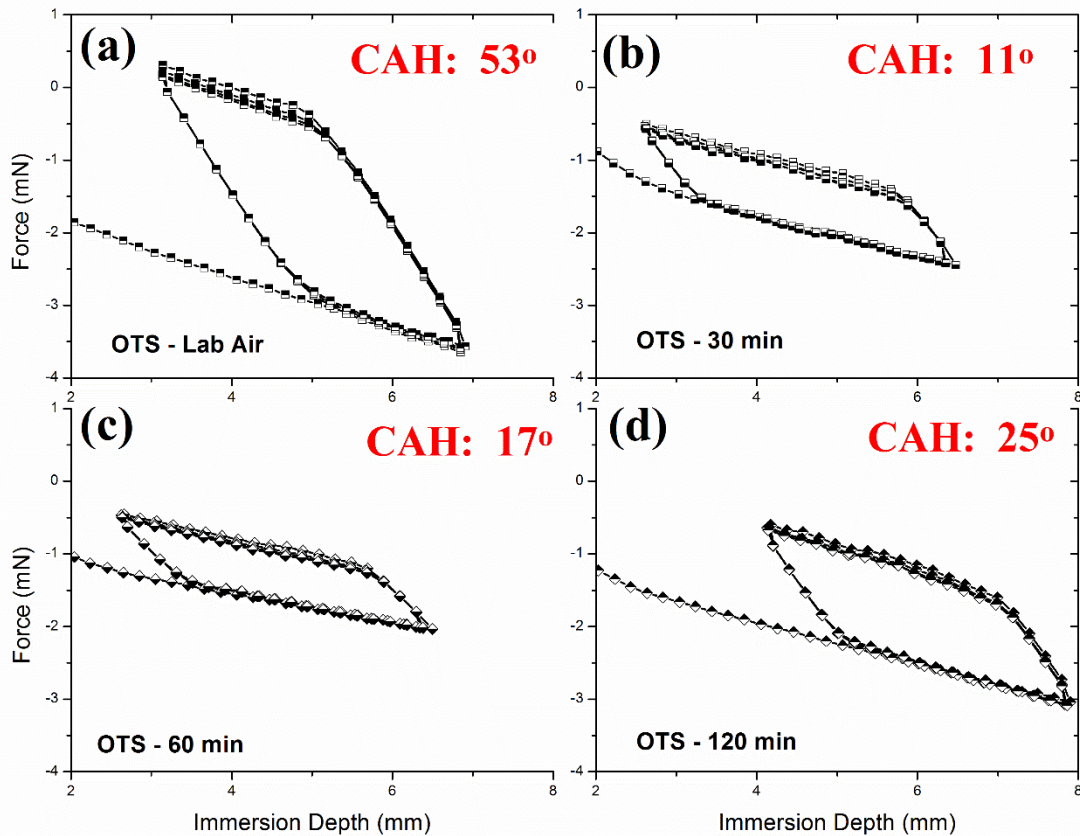


Figure 45: Force-depth measurements on silane surfaces at various immersion times (a) in lab air (b) under inert atmosphere immersed for 30 min, (c) 60 min, and (d) 120 min. Contact angle hysteresis values given in plot (red)

5.4 Conclusions

This chapter investigates the formation of thin hydrophobic layers on metal oxides for EWOD. Cytop provides a very consistent and easily prepared layer at 20 nm that would induce 30° of contact angle change with only 15 V. In order to further lower this voltage dependence, SAMs with silane and phosphonic acid headgroups were studied. Both layers, upon optimization of the formation process can similarly provide high contact angles, low contact angle hysteresis, and most importantly deposit at only 2 nm thicknesses, increasing capacitance and therefore contact angle change.

Chapter 6

Electrowetting

Part of this chapter is reproduced from:

M. Mibus, X. Hu, C. Knospe, M. L. Reed, and G. Zangari, "Failure Modes during Low Voltage Electrowetting," submitted.

The materials described in Chapters 4 and 5 are now integrated and evaluated with respect to EWOD performance. The electrowetting performance is studied through three types of characterization: static, cyclic, and dynamic. Static measurements monitor the contact angle vs. applied voltage by stepping at 1 V steps until failure of the layer. Cyclic measurements study the stability of repeated EWOD measurements on the surface, aiming to understand the causes of performance degradation. Dynamic measurements investigate electrowetting during externally controlled motion of the surface, thus estimating the reversibility of the EWOD process. Using the aluminum oxide + Cytop system, the importance of thickness for each layer and how reproducibility is altered over many applied voltage cycles are explored in detail. The comprehensive characterization of this system lays the foundation for studying how the tantalum oxide and different hydrophobic layers alter EWOD performance.

6.1 Aluminum Oxide + Cytop

6.1.1 Static Electrowetting

The contact angle vs. applied voltage characteristics was recorded by increasing the voltage stepwise and holding the value for 10 s, throughout the whole range of stable operation; this measurement is considered static since typical drop transport velocities are approximately 10-150 mm/s [147] and with typical drop response times under 15 ms [148]; the change in drop shape therefore occurs practically instantaneously. The thickness of both the Cytop and AlO_x layers were varied (Table 3), resulting in a variable overall capacitance; if the two capacitances in series are significantly different the smallest one will dominate. Table 3 shows the thickness of the two layers, and the calculated percentage of the total voltage drop across the polymer and the overall voltage V_T needed to exceed the breakdown voltage of the polymer layer. The calculation uses Eq. 26, discussed in detail later:

$$V_T = E_{Polymer} \left(t_{Polymer} + \frac{\epsilon_{Polymer}}{\epsilon_{Oxide}} t_{oxide} \right) \quad \text{Eq. 26}$$

where E is the breakdown field strength (V/nm), t the thickness (nm), and ϵ the dielectric strength.

T_{AlO_x} (nm)	$T_{Cytosol}$ (nm)	V_{drop} Cytosol (%)	V_T (V)
15	23	86.8	2.59
32	21	75.5	2.99
44	22	68.2	3.39
44	43	80.7	5.59
44	210	95.3	23.13

Table 3: Summary of sample configurations used in this study with the percentage of total voltage across the Cytosol layer and voltage needed to exceed the breakdown field of the Cytosol.

In order to achieve significant EWOD under 10 V, the overall capacitance must be maximized, which requires small Cytosol and AlO_x layer thicknesses. With increasing voltage, all the bilayers in Table 1 will exceed the breakdown field in the polymer layer first, in most cases at very low voltages, when the samples are still in the early stages of electrowetting. The sample with a thick Cytosol film, 210 nm, is added for performance comparison, allowing for a significant amount of electrowetting without exceeding the polymer breakdown field.

6.1.1.1 Effect of Oxide Thickness

Figure 46 shows the contact angle vs. applied voltage for three different aluminum oxide thicknesses (15nm to 44nm) while holding the Cytosol layer thickness approximately constant at ~20nm, within 2 nm, utilizing the same fabrication conditions. The applied voltage is increased until significant oxygen evolution occurs on the sample surface, indicated visually by the presence of bubbles during drop imaging and confirmed by the high current densities flowing through the bilayer ($10^{-6} - 10^{-5}$ A/cm²). Data are presented in double axis plots showing both the contact angle (left axis, black) and the current

flowing upon voltage stepping (right axis, blue) as a function of applied voltage. Each test exhibits three electrowetting regions: low voltage EWOD, saturation, and breakdown. Contact angle saturation at about $\sim 85\text{-}90^\circ$ is observed in Figure 46 (b) and (c) without incurring in gas evolution. Breakdown is observed after the onset of oxygen evolution from the oxide film, identified by a recession of the contact angle.

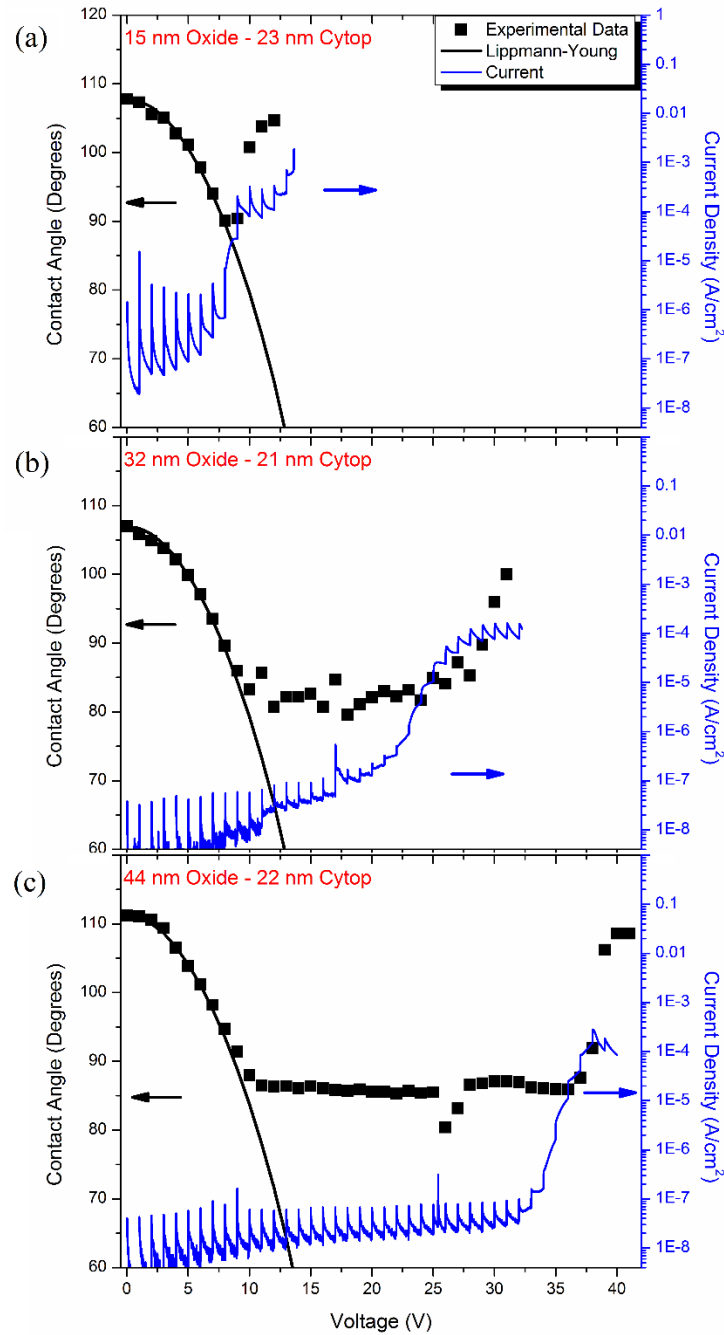


Figure 46: Electrowetting and leakage current measurements on bilayers of $\sim 22\text{nm}$ Cytop + Aluminum Oxide with thicknesses (a) 15nm (b) 32nm (c) 44nm . Contact angle data in black (left axis) with Eq. 6 modeled (black line) and measured current density in blue (right axis)

The *first stage of electrowetting* follows closely the Lippmann-Young relation (Eq. 6); experimental data in this range were fitted using the calculated series capacitance of Cytop (with $\epsilon_r=2.1$, and thickness

21nm) and aluminum oxide ($\epsilon_r = 9$, varying thickness, see plot labels). The relevant material parameters were experimentally validated using (i) XRR and ellipsometry as an independent thickness measurement and (ii) solid-state capacitance measurements for determination of the dielectric constant. Each sample showed minimal hindrance to contact angle change at low voltage, indicative of low contact angle hysteresis (i.e., a small difference between advancing and receding angles), with initial contact angles ranging from 107° - 111° across the samples. As discussed in Gupta et. al. [149], the initial motion of the contact line is often inhibited by contact line pinning, resulting in hysteresis of the surface and a voltage threshold to initiate deformation. In order to minimize contact angle hysteresis, electrowetting system designs may resort to drops immersed in oil [150], placed on an oil film [147], or may use an alternating current [151]; these approaches reduce hysteresis from 10 - 15° observed in air [113], at a cost of complicating design, operation, and modeling of the system. In particular, the influence of oil on the EWOD system has been discussed with regard to its effect on contact angle saturation [152] and breakdown voltage [153]. Our samples in contrast avoided these complications, since the bilayer system ideally followed the L-Y relation, probably as a consequence of the limited roughness (RMS roughness was 2 nm over a $1\mu\text{m} \times 1\mu\text{m}$ region – not shown) and surface defects in the polymer layer. As observed in Figure 46, no significant change from the ideal L-Y behavior, nor discontinuities in the current are observed when the voltage exceeds the polymer breakdown voltage (<5 V, see Table 1), suggesting that the leakage current is limited by the characteristics of the aluminum oxide [154].

The *second stage* of this process corresponds to CAS, the onset of which is defined by the initial deviation from the ideal L-Y curve. The phenomenon of contact angle saturation remains a point of ongoing discussion in the EW community, so far without a universal physical cause [152]. Several groups have suggested a fundamental reason for CAS, such as charge in the dielectric [155], charge in insulating fluid [152], gas ionization [39], contact line instability [39], [156] or electrochemical interpretation of reaching zero interfacial tension [157], [158]. CAS is observed in Figure 46(b) and (c), while the sample in Figure 46(a) underwent dielectric breakdown prior to CAS. In our polymer/oxide system, CAS occurs always at contact angles between 80 - 90° , with a minimum observed value of 79° . An interesting feature for these low thickness films is the relative instability of the saturation angle. For example, Figure 46(c) shows a constant angle up to 25 V, where a current spike is observed, resulting in a wetting angle increase of 6° . This remains stable during the voltage hold, but relaxes to the initial saturation angle during subsequent voltage cycling. Alternative evidence of such behavior is available later in the chapter (Figure 48(a)). This slight variation in wetting angle

in the saturation region is always observed during the measurements conducted in this study, and is likely caused by the strong voltage influence in the thin film system due to the larger overall capacitance, as discussed in the following. Specifically, under the electromechanical interpretation of electrowetting, the net force acting on the drop is given by the total capacitance times the applied voltage squared ($CV^2/2$) [38]. The instability of the saturation angle suggests that, rather than an absolute phenomenon limiting further wetting, a balance between opposing forces occurs that temporarily allows further wetting prior to returning to the initial saturation angle. For example, the calculated horizontal force exerted on the contact line, under ideal conditions, in Figure 46(c) increases from .041 N/m at saturation (10 V) to more than quadruple to 0.18 N/m during the enhanced wetting at 25V. These forces are significantly higher for thin film layers; in contrast, a 500 nm thick Cytop yields a much lower force of .011 N/m at 25V, a 16x decrease. The significantly stronger force acting on the thin films in Figure 46 could overcome the as yet unidentified opposing force that prohibits further contact line movement in thicker polymer systems, albeit temporarily, before instabilities occur and the system relaxes at the saturation angle. As will be discussed in the cyclic experiments, charge at the electrolyte-polymer interface appears to diminish EWOD performance. The return of the contact angle from the unstable wetted state to the saturation contact angle could be a consequence of charge incorporation on the newly wetted surface. Charge adsorbed or injected in the polymer would partially screen the electric field, reducing the driving force on the liquid, causing the system to return to the saturation angle.

The *third characteristic stage* occurs when the voltage applied through the oxide layer exceeds the anodization voltage, resulting in a shift from electronic to ionic conduction in the oxide, followed soon after by gas evolution [154]. Very small gas bubbles are observed at the center of the electrolytic drop concurrent with the onset of contact angle recession. This recession is likely caused by breakdown in the oxide layer occurring at voltages higher than the anodization voltage, which thus becomes unable to hold charge, causing the drop to reset to the initial sessile contact angle. This is demonstrated for each sample in Figure 46, even in the film that failed to saturate. With increasing voltage in the breakdown region, the contact angle begins to drop dramatically until nearly reaching complete wetting ($\theta < 15^\circ$). Figure 47 shows the surface of a Cytop/aluminum oxide sample following failure. After the drop recedes to the sessile angle upon gas evolution, the electrolyte begins to show a wetted out region next to the drop, highlighted with red arrows in the inset of Figure 47(a). With additional applied voltage the drop essentially falls out of contact with the needle probe onto the completely wetted surface. Imaging of the surface following the measurement shows removal of the

polymer across the entire drop area (Figure 47(a)), confirmed by the weaker Fluorine $K\alpha$ signal in yellow in the inner region (Figure 47(b)). The drop profile on the wetted area displays a sharp corner between the fluid and wetted section of the liquid drop, which should not be possible, as this configuration is incompatible with solutions to the hemispheroid Young-Laplace equation (Eq. 1). We hypothesize that in this case the oxygen evolution would generate a force sufficient to form a tear in the polymer layer, allowing for the liquid to seep under the Cytop film, until the eventual complete detachment. Similar observations were conducted to investigate the surface prior to the stage of complete wetting and polymer detachment, but no remarkable features were observed.

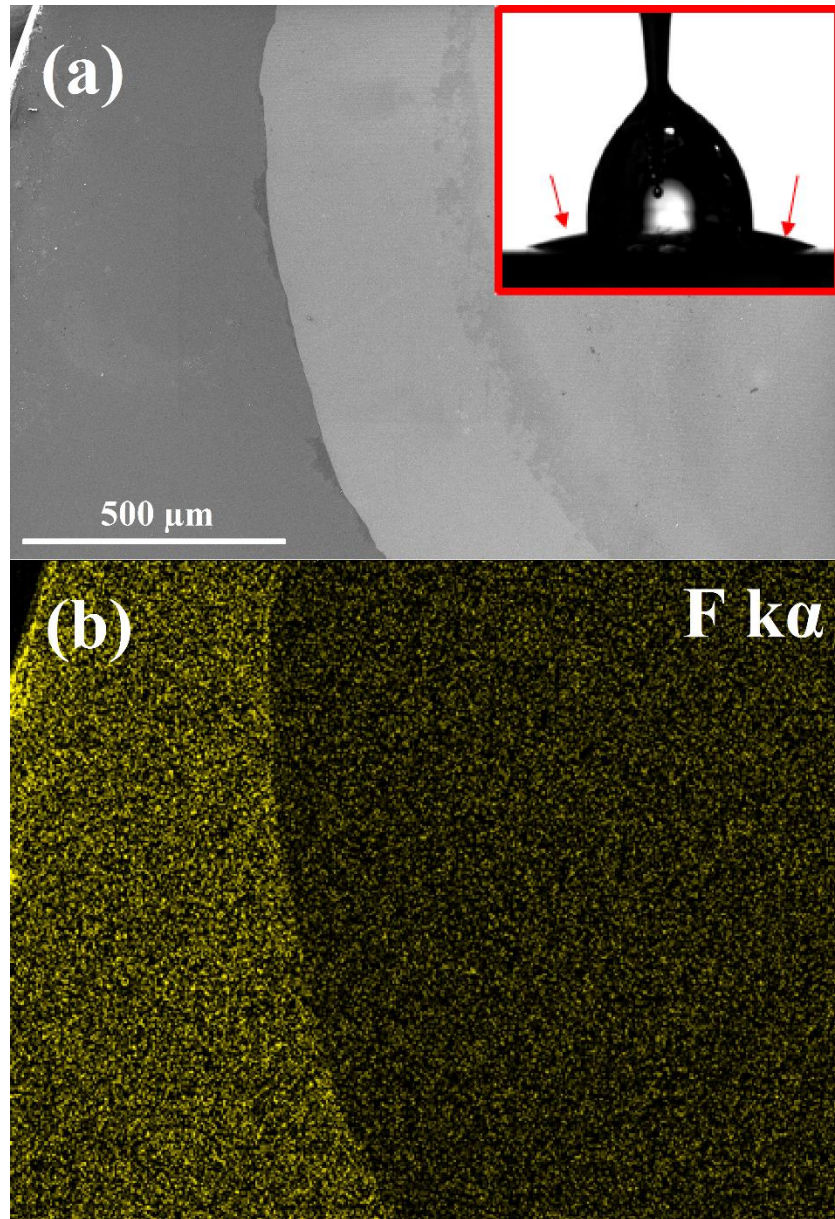


Figure 47: SEM image of Aluminum Oxide – Cytop layer showing the detachment of the fluoropolymer indicated by wetting out in the drop image inset. EDS map of Fluorine signal given in yellow.

6.1.1.2 Effect of Polymer Thickness

Samples with varying polymer layer thickness (43nm – 210nm) on top of 44 nm AlO_x exhibit the same three characteristic regions as discussed in the previous section. The bilayer capacitance is still

dominated by the polymer layer, due to the four times lower dielectric strength of the polymer layer compared to the oxide. Increasing the polymer layer thickness therefore causes a decrease in the total capacitance, weakening the initial low-voltage EWOD response. The rate of contact angle change with voltage is now lower, but the saturation angle remains approximately the same as the tests shown in Figure 46. Failure in these devices occurs via the same mechanisms of oxide breakdown, similarly leading to detachment of the polymer layer.

Figure 48 shows contact angle and leakage current data for two Cytop thicknesses: 43 and 210 nm, respectively. The region of contact angle saturation showed the same unstable behavior, described in reference to Figure 46, suggesting a significant influence of the balancing of opposing forces at the saturation angle. In Figure 48(a), the saturation angle regularly decreases until a discontinuous jump to a lower angle, prior to recession in the saturation regime. The process is particularly evident in the 210 nm layer, showing three instances of increased wetting prior to the apparent contact angle retreating to the initial CAS values. The increasing polymer layer thickness would increase the voltage drop therein, and shift the onset of ionic conduction transition in the oxide from 30 V at 43nm Cytop to nearly 40 V at 210 nm. Similar behavior is observed in these bilayers, resulting eventually in gas evolution at the oxide film, contact angle recession, and eventual polymer detachment. Interestingly, the voltage to exceed the Cytop breakdown field in the 210 nm case is nearly 23 V, with no particular difference in performance observed in comparison to the previous thin film polymer cases. This leads us to conclude that the oxide layer limits the leakage current, and controls performance independently of the polymer thickness.

In order to increase the contact angle dependence on voltage in these bilayer systems, the thickness of the polymer layer should be minimized. A ~20 nm thick polymer layer was utilized in the previous set of films, as this was the thinnest layer that our fabrication process could reliably synthesize; thinner layers in fact commonly show small gaps or tears as observed by SEM imaging. As demonstrated in Figure 48, a larger polymer thickness did not demonstrate any advantageous features in comparison to the 20 nm polymers for single run, stepped voltage measurements. Therefore we conclude that, from the standpoint of stepped static electrowetting, the polymer should be applied as thin as possible to form a consistent and uniform surface, providing sufficient hydrophobicity while minimizing the contribution of the polymer to the overall capacitance.

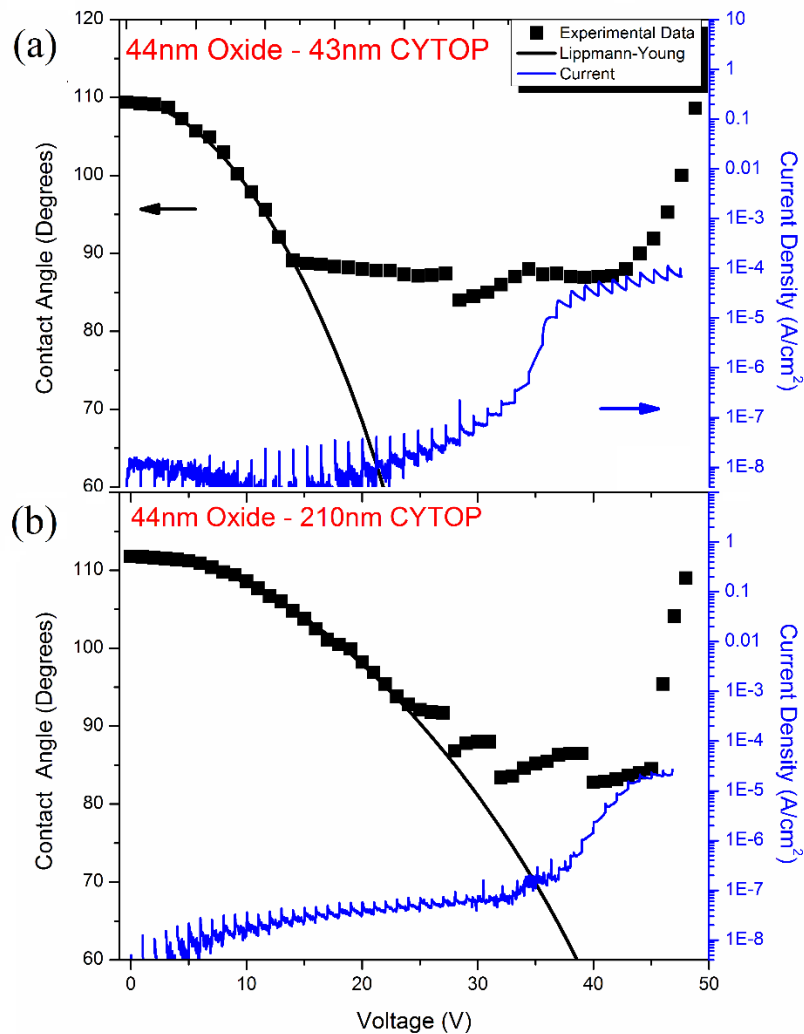


Figure 48: Electrowetting and leakage current measurements on bilayers of Aluminum Oxide - Cytop of (a) 43nm and (b) 210nm. Contact angle data in black (left axis) with EQ.1 modeled (black line) and measured current density in blue (right axis)

6.1.2 Cyclic Electrowetting

The previous measurements evaluated electrowetting performance at one sample location through all the electrowetting stages until breakdown and failure. These measurements resulted in polymer detachment, losing the EWOD function. In contrast, similar samples tested at a voltage lower than the AlO_x anodization voltage showed a reproducible characteristics for several cycles. It has been reported however that significant degradation of electrowetting performance would occur over many actuation cycles, showing a continuous decrease in the contact angle change [16]. The most common

explanation for such degradation over time has been the injection of charges into the fluoropolymer during voltage bias. These materials have been shown to hold charge permanently, in contrast to the transient function of capacitors. Fluoropolymers with thickness on the order of microns have experimentally shown to hold charge up to 3.9 mC/cm^2 , functioning as electrets [159]–[161]; Cytop in particular was shown to reach charge densities up to 1.5 mC/cm^2 [161], with charge storage maintained for at least 4000 hr. The concept of trapped charges diminishing the response of the layer was proposed long ago [155], following observation of a threshold for irreversible electrowetting response. Berry et. al., furthered this theory by developing an empirical model based on the breakdown voltage of the fluoropolymer as the threshold for charge injection [162]. For the oxide-polymer bilayer system the threshold voltage for charge injection (Eq. 26) is the point when the voltage drop across the polymer layer, modeled through the series capacitance, exceeds the breakdown field of the polymer layer.

The reversibility of the contact angle change (CAC) was investigated for the polymer – oxide bilayer configurations evaluated in Figure 46. The saturation angle was observed as 86° at 11 V during the sweeping measurements (see Figure 46(c)), leading to a selection of 15 V for the maximum applied voltage for the “on” state, ensuring saturation while remaining below half the anodization voltage (30 V), thus minimizing undesirable degradation in the oxide layer. A cycle is defined as one 10 s “on” period at the specified voltage and a 10 s “off” period at 0 V. Figure 49 shows the resulting CAC from a 21 nm polymer/32 nm oxide bilayer, Figure 49(a), and 21 nm polymer/44 nm oxide, Figure 49(b). The threshold voltage (Eq. 26) in both cases was below 5 V due to the polymer layer thickness, leading to a rapidly degrading CAC in both cases. A higher oxide layer thickness does slightly increase the amount of reversible CAC, with a 44nm oxide reaching 50 cycles compared to only 30 cycles for 32nm, but doesn’t significantly enhance reversibility for any long term operation.

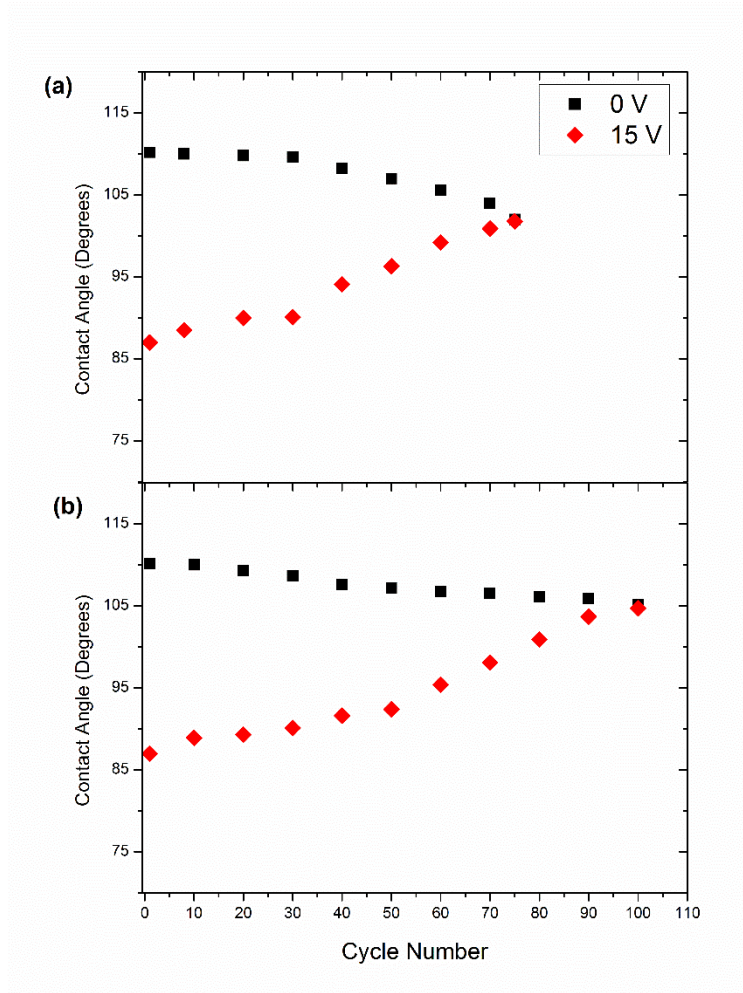


Figure 49: Contact angle vs. Cycle number are shown for cyclic measurements of (a) 32nm aluminum oxide – 21nm Cytop and (b) 44nm aluminum oxide – 22nm Cytop bilayers until no wetting was observed

‘ In order to better understand the effect of V_T , a 210 nm Cytop/44 nm aluminum oxide bilayer was chosen, allowing significant EWOD while not exceeding the polymer breakdown field. For this sample V_T was 23.13 V, and EWOD was investigated at an applied voltage above (25 V) and below (20 V) V_T . Figure 50 shows contact angle data at roughly 25 cycle intervals for both “on” and “off” states. The stepped voltage characteristics for this bilayer was presented in Figure 48(c), showing that at 20 V the expected contact angle was 98.2°, while at 25 V it was 92.1°. The initial contact angle closely matched the stepped experiment for each applied voltage, with the 25 V case having a lower wetted angle due to variability in the CAS region. A stark difference is evident between the two tests as a function of cycle number; below the voltage threshold no significant degradation occurred to the

contact angle during 300 cycles, maintaining a contact angle change (CAC) of $\sim 11^\circ$. In contrast, above V_T , the contact angle rapidly degraded after 100 cycles decreasing from a CAC of 23° to 9.5° , with the difference continually decreasing until almost no change was observed at 300 cycles. In the trapped charge model [162], a voltage term V_c is added to the L-Y expression (Eq. 27) to estimate the effect of trapped charge density σ_c (Eq. 28) on the decrease of the applied voltage on the electrowetting effect.

$$\cos(\theta) = \cos(\theta_0) + \frac{C(V_{app}-V_c)^2}{2\gamma_{LG}} \quad \text{Eq. 27}$$

$$\sigma_c = CV_c \quad \text{Eq. 28}$$

The 25 V experiment results in zero contact angle change at the end of the measurement, making $V_c = V_{app} = 25V$; using the above equations an injected charge density of $2.11 \times 10^{-4} \text{ mC/cm}^2$ was calculated. In contrast, the contact angle during the 20 V test increases from 97.5° to 98.3° , estimating a charge density of $1.4 \times 10^{-5} \text{ mC/cm}^2$. Similar values on the order of 10^{-5} mC/cm^2 were obtained using the same methodology [162], while a value of 10^{-4} mC/cm^2 was found using a charging-discharging method [163]. The charge densities measured here are well below the values found for the polymers used as electrets $\sim \text{mC/cm}^2$, with the charge limited to contact angle degradation measurements.

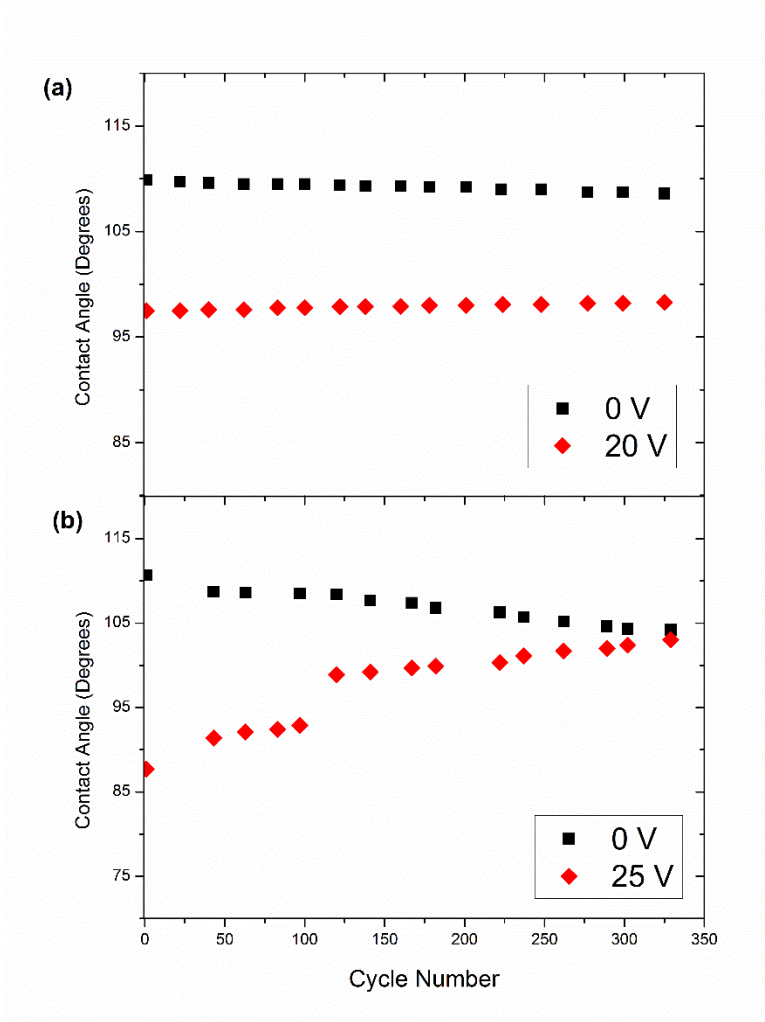


Figure 50: Contact angle vs. Cycle number cyclic measurements are shown on 44nm aluminum oxide /210nm cytop bilayer with applied voltages of (a) $V_{on} = 20\text{ V}$ and (b) $V_{on} = 25\text{ V}$

Leakage current has been monitored closely in similar electrowetting systems [18], [19], [164] attempting to link performance degradation to underlying changes in the films. Figure 51 shows the current vs. time transients of the cyclic measurements extracted from the contact angle variation reported in Figure 50, showing cycles 125 to 130. Figure 51(a) from the 20 V test shows a stable leakage current, limited to the range between $\pm 7 \times 10^{-7}\text{ A/cm}^2$ depending on the “on” or “off” cycle. A similar value of current is observed from the 25V test if we neglect the large initial current spike, due to the larger applied voltage. The result is noteworthy as the current during the $V_{on} = 25\text{ V}$ case (Figure 51(b)) remains relatively constant around $1.6 \times 10^{-6}\text{ A/cm}^2$, while the contact angle change varies drastically during these cycles. The current transients show a very different behavior than those

reported in Figure 46 and Figure 48 during failure, where the current reached $\sim 10^{-4}$ A/cm² along with gas evolution. We suggest that the leakage current per se is not a proxy to estimate the extent of degradation towards failure, but it depends strongly on the mode of failure the system is undergoing increasing voltage vs. cycle voltage bias. Although the current-time characteristics from Figure 51(b) show the same current densities values and shape from the initial cycles to the end of measurement, we note that the slope of the V_{on} response shows an increasing trend once the contact angle degradation in Figure 50(b) begins. This potential correlation between degradation and the increasing slope feature is only a preliminary hypothesis at this stage (but explored further in Future Work, Section 7.2).

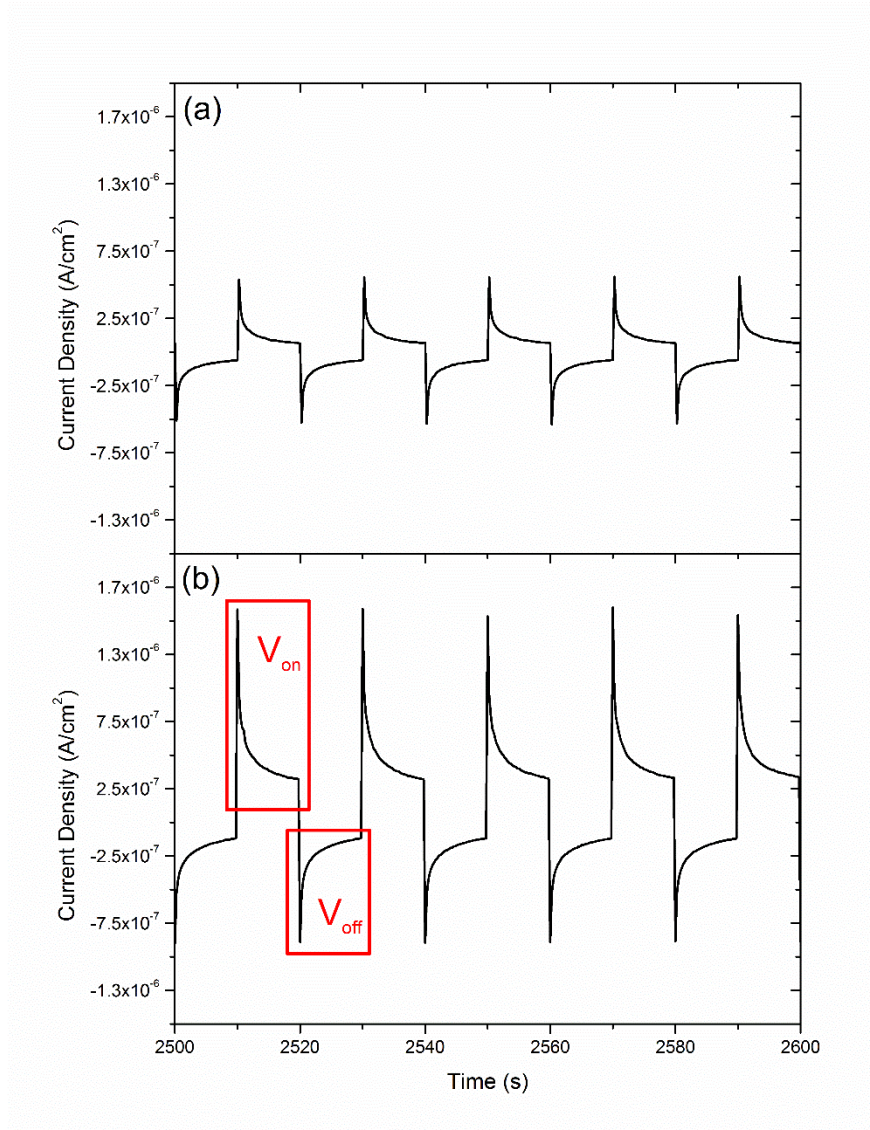


Figure 51: (a) Current-time transient for cycles 125 to 130 from the Fig. 5 contact angle measurements with (a) $V_{on} = 20$ V and (b) $V_{on} = 25$ V on 44nm aluminum oxide/210nm Cytop bilayer.

6.1.3 Scanning Kelvin Probe

SKP measurements were conducted in order to evaluate the amount of damage during cyclic EWOD measurements. Scans across the sample surface provide a contact potential difference (CPD) map that could be used to provide a possible correlation between the local surface potential and the contact angle degradation. Figure 52 displays the CPD measured at the 44 nm oxide-20 nm Cytop after 13, 25, 50, and 125 cycles at 15 V on a single large area substrate. As established in Figure 51(b), CAC rapidly degrades after 50 cycles, as the Cytop layer is subjected to a voltage significantly above V_T , thus

providing minimal resistance to charge incorporation. After 13 cycles the substrate already showed a measurable amount of degradation, which increased significantly with progression of the cyclic stress. After 50 cycles a CPD of 1000 mV was measured, which corresponds to the stage where the bilayer loses the ability to electrowet. After 125 cycles no CAC occurred, with the CPD reaching 1600 mV.

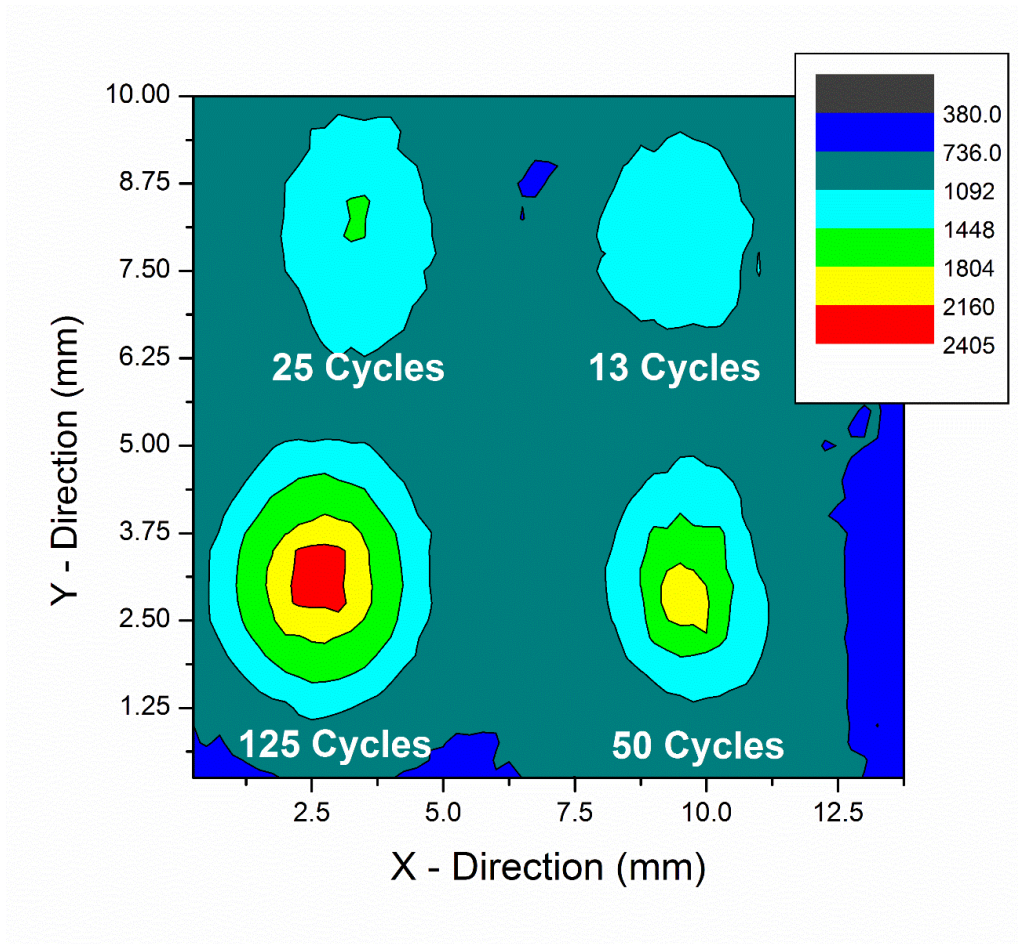


Figure 52: Contact potential difference maps of 44 nm Al_2O_3 – 20 nm Cytop surfaces total cycle, numbers indicated in the figure. Colors correspond to mV in legend

The Kelvin probe scan is particularly informative in the thick polymer bilayer 210nm Cytop – 44nm aluminum oxide system. The degradation of the material after 325 cycles reported in Figure 50 was evaluated with the SKP, as shown in Figure 53. The two cyclic tests show the dramatic difference in the polymer damage for V_{on} of 20 V and 25 V, with 20 V showing a max CPD of 1626 mV while 25 V reaches 6583 mV. A scan of the pristine substrate maintains a consistent CPD of $\sim 530 \pm 100$

mV throughout the surface. The striking difference is consistent with what was previously observed in the 20 V case, which revealed a constant CAC, while the amount of damage at the 25 V site limits the ability of the drop to further electrowet. However, under the concept of the threshold voltage for charge incorporation, the 20 V case should be indistinguishable from the untested substrate as the threshold was not exceeded. This indicates that with $V_{on} = 20$ V some charge is still introduced into the polymer layer, which should over many cycles similarly degrade the CAC repeatability.

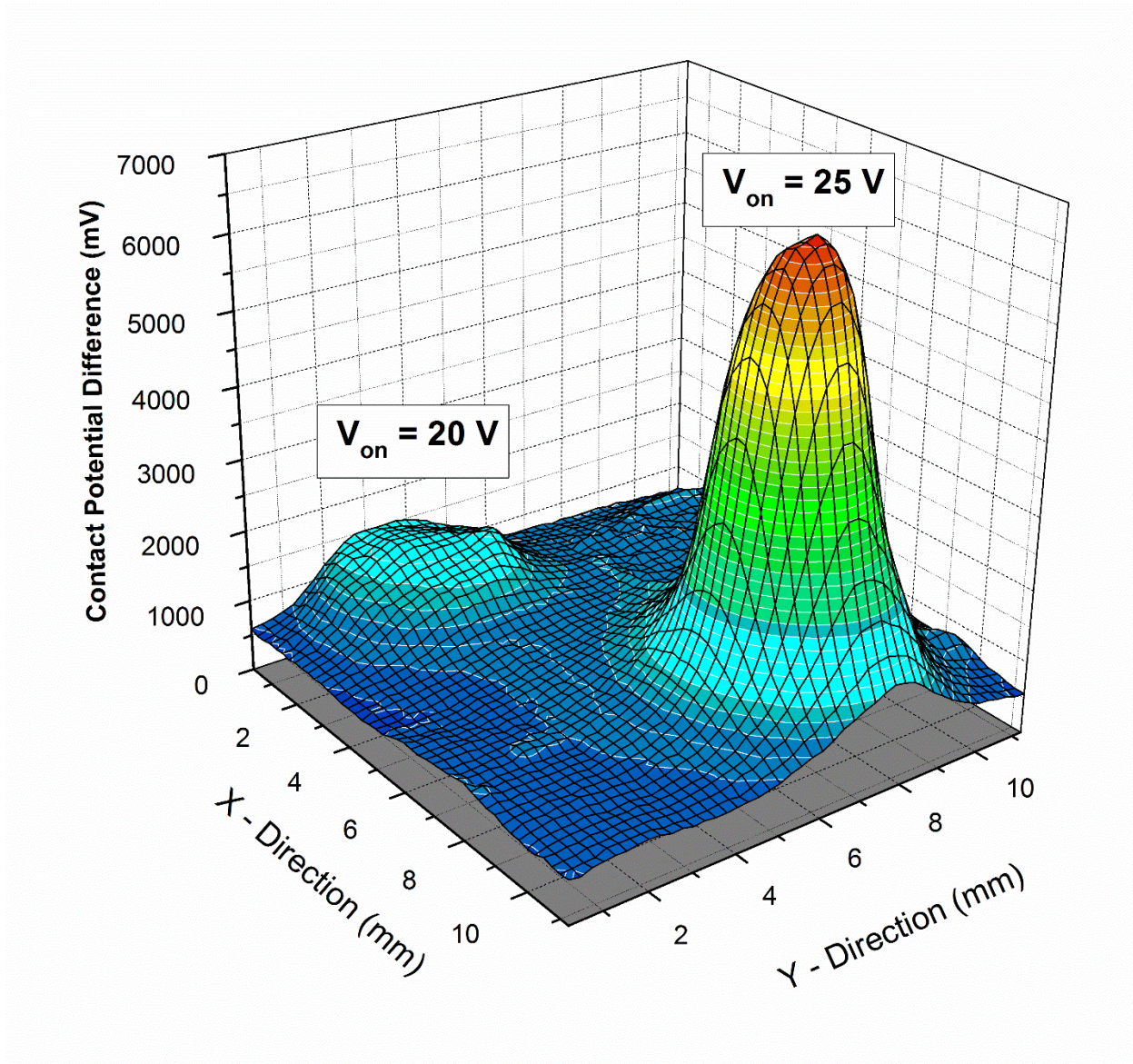


Figure 53: Contact potential difference map of 44 nm Al_2O_3 – 210 nm Cytop surface with cycle applied voltage values for cyclic spots, numbers indicated in the figure.

A charge injection technique is commonly used to determine the integrity of gate oxides in semiconductor fabrication by depositing charge through a corona discharge [165]. If the trapped charge is located within the polymer layer and is significantly larger than the native charge in the aluminum oxide and interface, the charge density is simply given by the potential drop due to the capacitance of the polymer [166], [167]. Under this assumption, the charge derived from the CPD values is estimated to be $5.359 \times 10^{-5} \text{ mC/cm}^2$ at 25V and $9.704 \times 10^{-6} \text{ mC/cm}^2$ at 20V. Both values however underestimate those derived from the trapped charge model discussed in regard with the cyclic measurements. It is possible that the assumptions and simple analysis of the SKP charge may not provide a complete picture, or that the trapped charge EWOD model overestimates the charge injected, as it assumes that all the degradation in the contact angle is a consequence of charges in the film. However, these results confirm qualitatively what was observed in the cyclic measurement and the importance of the threshold voltage concept. Thus, prolonged cyclic measurements in low voltage EWOD systems may inevitably lead to thin film polymer degradation, as V_T will always be well below the applied voltage necessary for useful EWOD. In order to improve the long term stability of these bilayer systems, it is instead necessary to limit charge incorporation into the polymer film, for example by altering ion size [18], [154], or using non aqueous electrolytes [168].

6. 2 Tantalum Oxide + Cytop

6.2.1 Static Electrowetting

The EWOD performance of tantalum oxide was also studied, using the same measurement configuration used for investigation on aluminum oxide,. Figure 54, shows a theoretical Lippmann-Young plot comparing the aluminum and tantalum oxide layers coupled with 21 nm of Cytop. The total applied voltage necessary to obtain a theoretical CAS angle of 85° decreases by only about 1 V. Both oxide and polymer thickness were varied in order to assess of EWOD performance, but only using thin films of Cytop could any difference between the metal oxide's performance be observed. Tantalum oxide has a dielectric constant of 25 compared to 9 for aluminum oxide, but this increase in dielectric constant has limited effect as the polymer layer dominates the overall capacitance as discussed using Eq. 25 in Chapter 5. With increasing polymer thickness, the difference between the curves becomes indistinguishable.

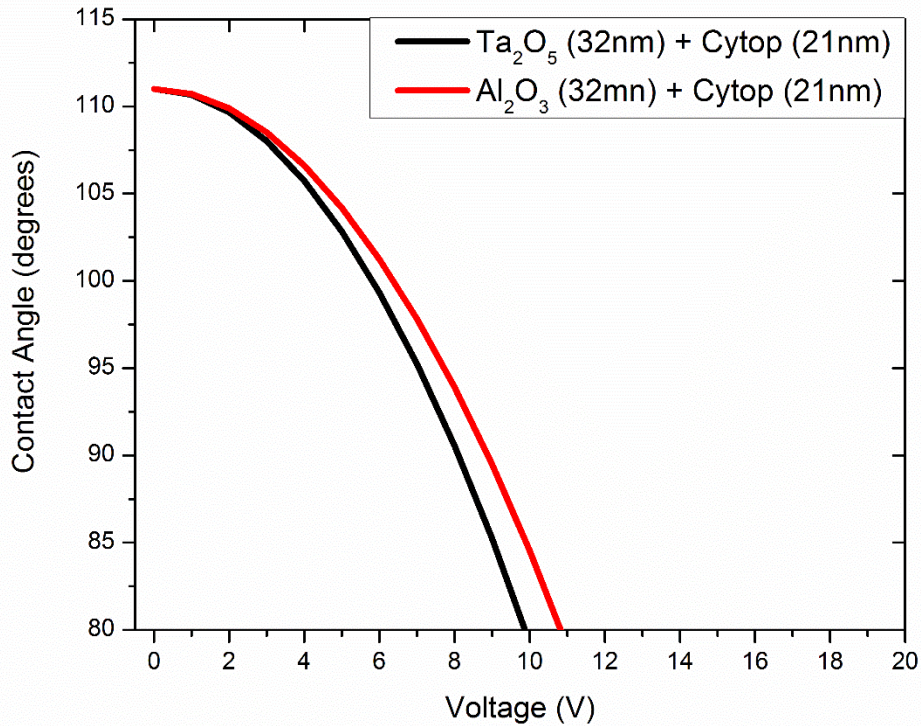


Figure 54: Theoretical contact angle vs. voltage Lippmann-Young curves for 21 nm Cytop + 32 nm Ta₂O₅ (black) and Al₂O₃ (red)

Full static EWOD measurements are shown in Figure 55, for 32 and 44 nm tantalum oxide with a 21 nm Cytop layer. The response mimics the same three region response shown in Figure 46 of ideal L-Y, CAS, and breakdown. The change from electronic to ionic conduction takes place at the anodization voltage, which occurs at slightly lower values than in aluminum oxide due to the different thickness dependence on anodization voltage of the materials. For example, 44 nm aluminum oxide is anodized at 30 V while 26.5 V are needed to grow 44 nm tantalum oxide making the change from electronic to ionic conduction occur sooner. The breakdown occurs identically; after the onset of gas evolution, the contact angle returns to the initial value. With additional voltage steps the polymer layer detaches and the surface is wetted.

The largest difference between the aluminum and tantalum oxide systems is observed in the current density during the measurement. In the CAS region, the tantalum oxide current is approximately 10^{-6} A/cm² while the aluminum bilayer system averaged $\sim 5 \times 10^{-7}$ A/cm². This

difference is consistent with what was shown in Chapter 4, with tantalum oxide showing more leakage current due to a smaller band gap. The significant increase in current during the measurement did not alter the performance of the single stepped voltage curves, but would likely affect cyclic tests, as will be discussed in 6.2.2.

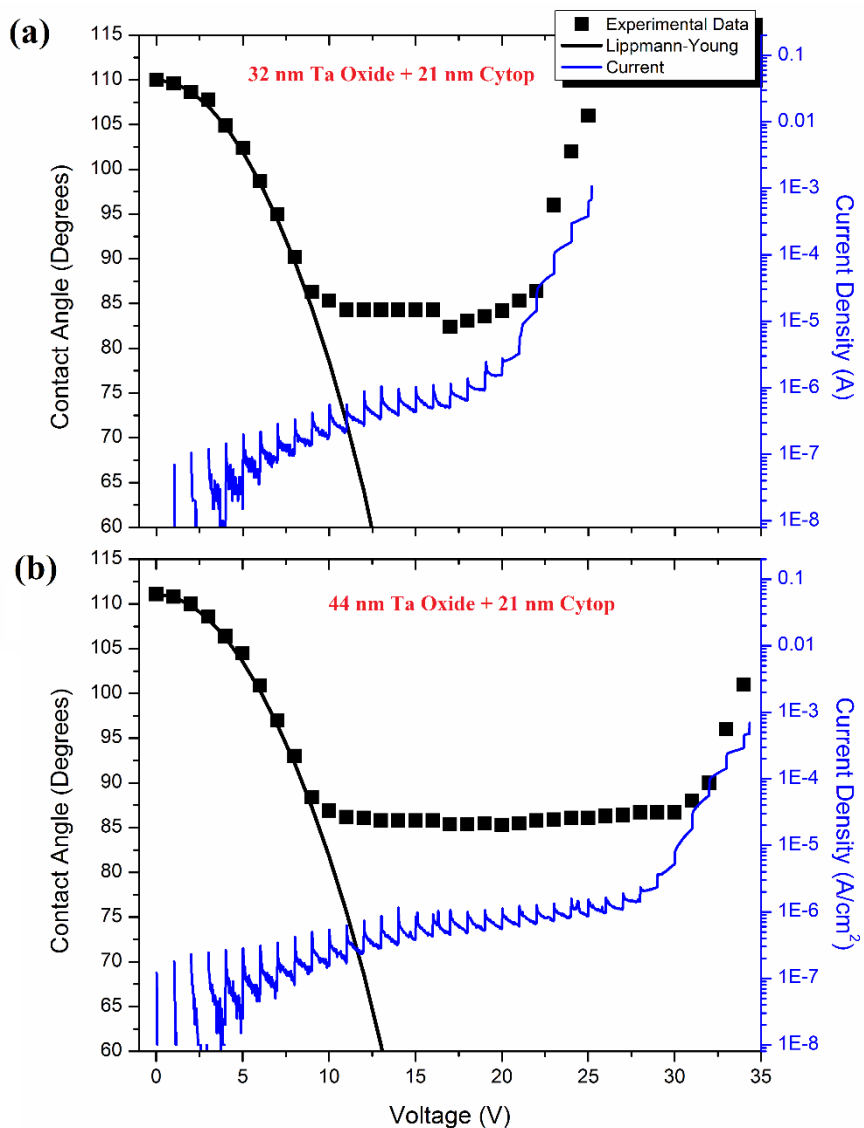


Figure 55: Electrowetting and leakage current measurements on bilayers of $\sim 22\text{nm}$ Cytop + tantalum oxide with thicknesses (a) 32nm and (b) 44nm . Contact angle data in black (left axis) with Eq. 6 modeled (black line) and measured current density in blue (right axis)

6.2.2 Cyclic Electrowetting

The same oxide/polymer thickness combinations were tested for cyclic performance as in Figure 49, using tantalum oxide in place of aluminum oxide in Figure 56. The cyclic tests used $V_{on} = 15$ V for both cases, well within the CAS region for both the 32 nm (Figure 55 (a)) and 44 nm (Figure 55 (b)) films, as seen in the static electrowetting measurements. The 32 nm tantalum oxide case, from an initial CAC of 22.9° , rapidly decreased to less than 5° after 15 cycles. Several measurements on the same sample surface (fresh spots) showed a very consistent number of total cycles needed for CAC to go to zero CAC. In comparison to Figure 49 (a), the aluminum oxide samples saw relatively stable CAC till 40 V, with no CAC occurring after 80 cycles, a significantly larger window of reusability. The 44 nm tantalum oxide case showed a considerably more stable CAC performance, as shown in Figure 56 (b). Initially, the CAC showed 26.4° , but readily decreased to 15.3° after only 10 cycles. This CAC remained fairly stable until 30 cycles, with complete degradation by 55 cycles. Again, in comparison to the same thickness AlO_x system, the performance shows significantly less reproducibility cutting the amount of cycles in half.

As was suggested in the previous section, the higher leakage current would suggest more charge injection and quicker degradation of the layer. For thin films (~ 20 nm Cytop), the applied voltage remains well above the V_T voltage, indicating that the field across the polymer is well beyond the breakdown. Therefore, the less resistive tantalum oxide films lead to quick degradation of EWOD performance.

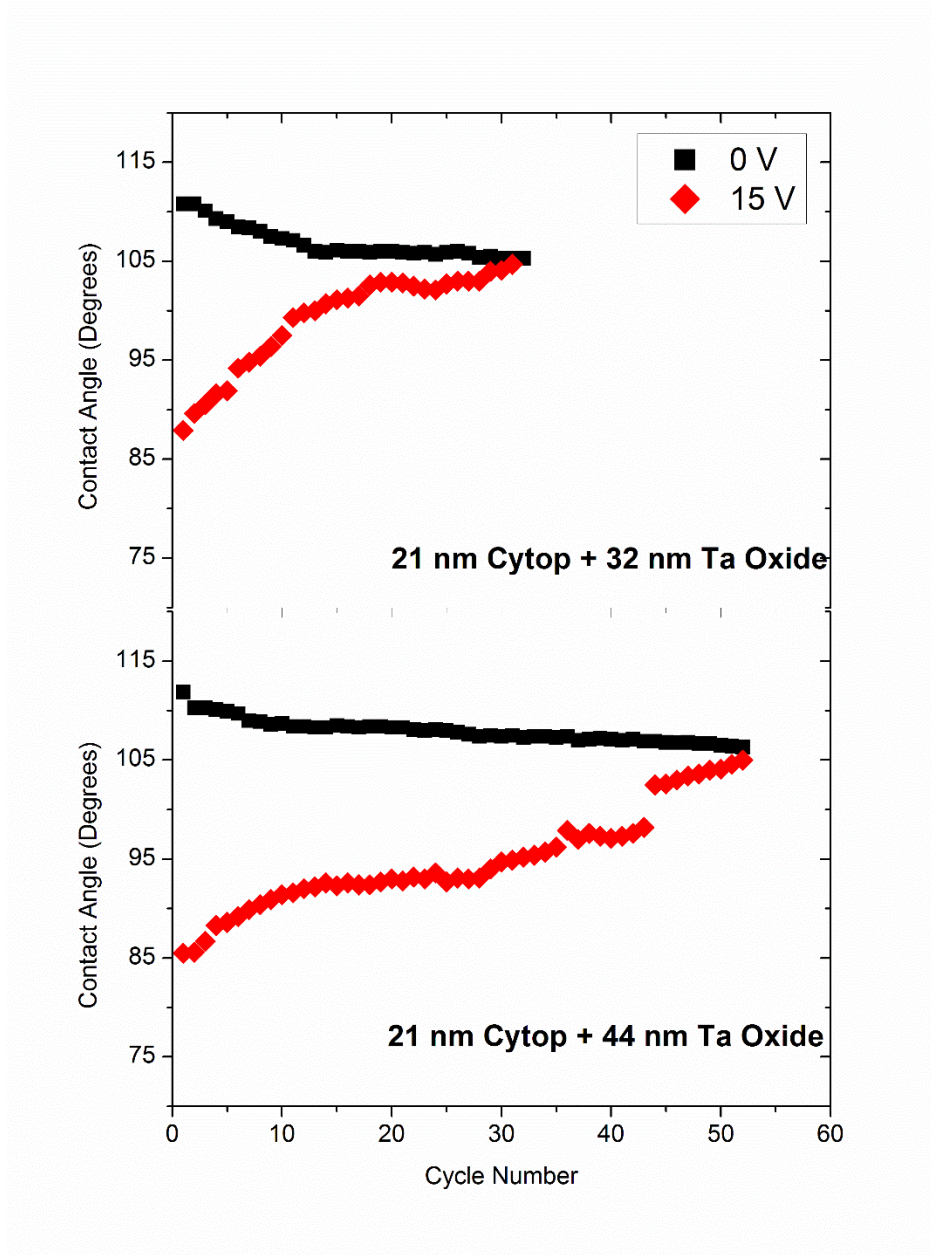


Figure 56: Contact angle vs. Cycle number are shown for cyclic measurements of (a) 32nm tantalum oxide – 21nm Cytop and (b) 44nm tantalum oxide – 22nm Cytop bilayers until no wetting was observed

The damage to the surfaces due to cyclic contact angle changes was assessed using the SKP system measuring the CPD of the surface for a single 21 nm Cytop + 44 nm tantalum oxide substrate. Figure 57 displays the CPD measured after 20, 40, and 60 cycles at 15 V. The plot uses the same color thresholds indicating the CPD in mV as shown in Figure 52 for aluminum oxide. The background

CPD of the substrate is similar to the previous system at a value of 827 mV. The tantalum based bilayers show higher CPD values, with the final CPD at no CAC reaching a value of 1980 mV compared to 1600 mV in aluminum oxide. Although higher for tantalum oxide, the overall CPD values for the two systems remain fairly similar to the point of no further CAC.

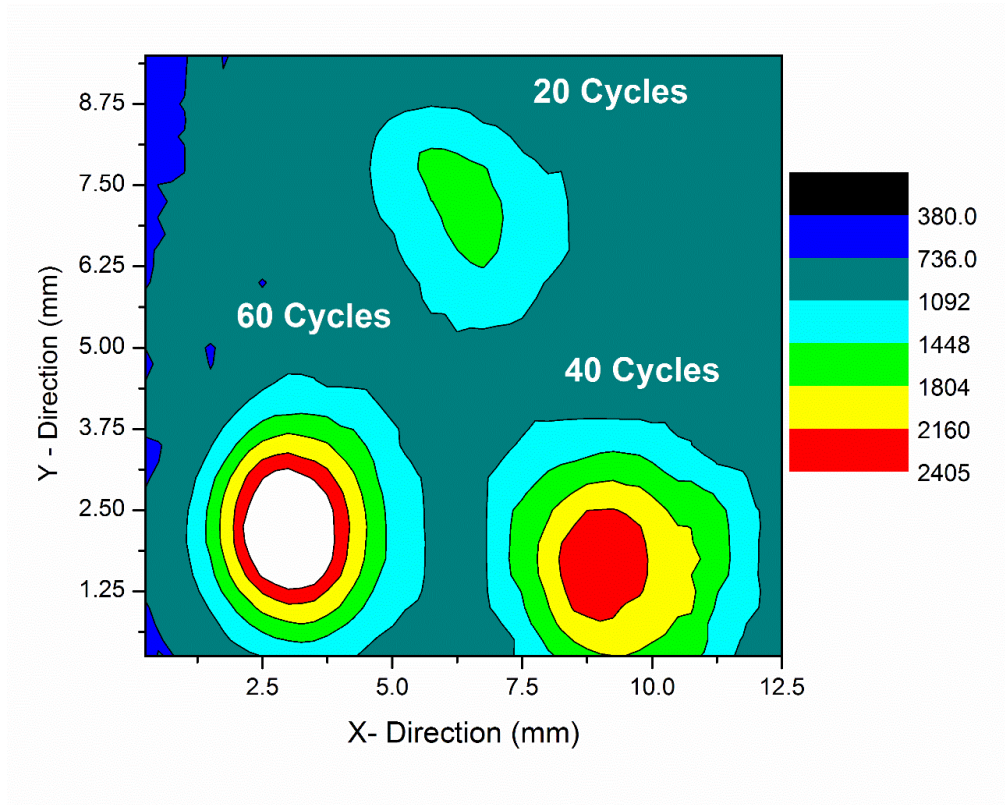


Figure 57: Contact potential difference maps of 44 nm Ta₂O₅ – 21 nm Cyttop surfaces, total cycle numbers indicated in the figure. Colors correspond to mV in legend

The results from Figure 57 in tantalum oxide are very interesting in comparison to the same 21 nm Cyttop surface covering aluminum (Figure 52). When we considered the trapped charge values estimated for the thick aluminum oxide – Cyttop system (Section 6.1.3), the trapped charge model and SKP were used. The trapped charge model uses Eq. 27 and Eq. 28 to estimate the charge using the entire dielectric capacitance while the other model only considers the SKP CPD as the voltage drop over the polymer layer ($V = \sigma/C$). In the latter case, it makes sense that the measured CPD doesn't change between the aluminum and tantalum oxide systems.

At 15 V, the tantalum oxide still shows only electronic conduction mechanisms (Section 4.2.2) and functions as the primary insulator in the polymer-oxide dielectric stack. Figure 58 shows the same number of 15 V cycles being applied to the oxide layer as in Figure 57, applied to only 44 nm tantalum oxide layer without the hydrophobic layer. The drops unsurprisingly didn't show any electrowetting as the surface shows an initial contact angle below 30° and the oxide surface is highly hysteretic. The SKP evaluation at the same Z-scale as Figure 57 demonstrated minimal measured charge (Figure 58(a)). Upon rescaling the Z-scale (Figure 58(b)), the damage from the repeated cycles could be observed, but with CPD value much lower than that of the same Cytop system. This is further explored in the thick polymer case.

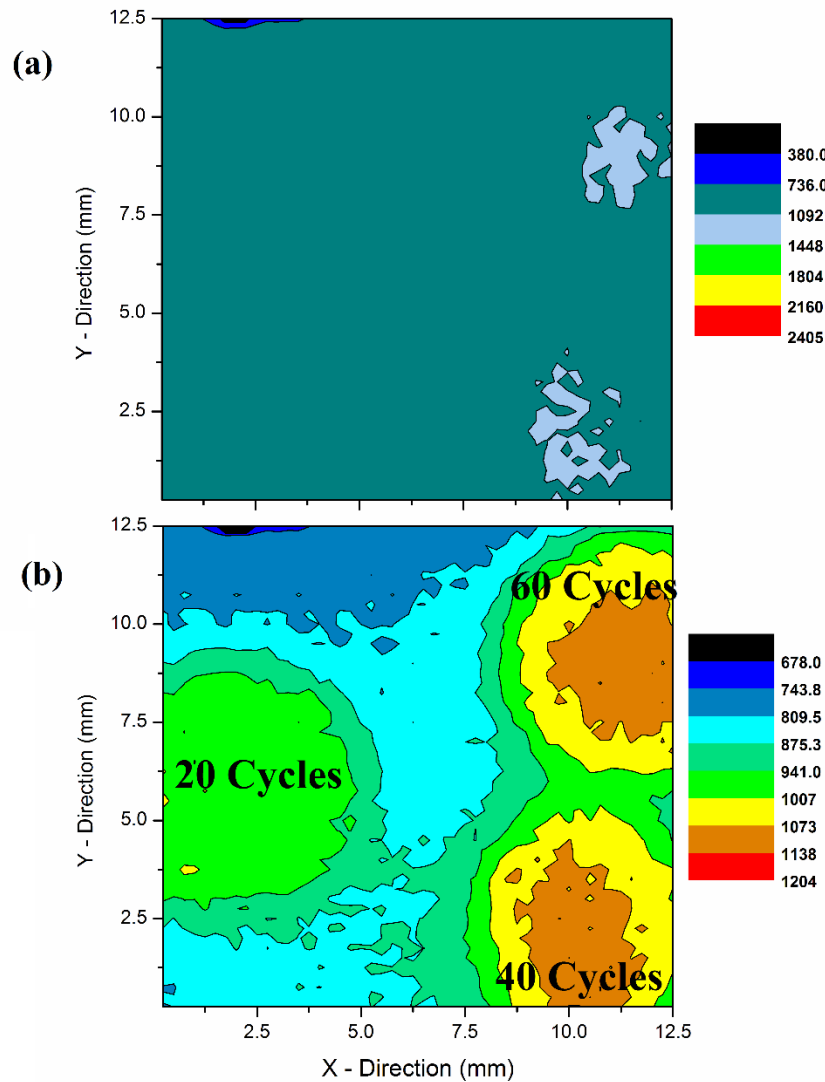


Figure 58: Contact potential difference map of 44 nm Ta₂O₅ surfaces, total cycle numbers indicated in the figure. (a) & (b) are the same surface at different scales, in mV indicated by the legend

To further test the V_T concept [162], 44 nm tantalum oxide is used in conjunction with the 210 nm polymer layer. Theoretically, if staying under the voltage threshold, no difference should be observed between the tantalum and aluminum oxide system according to the model [162]. Changing the oxide alters the V_T slightly (Eq. 26), for this system to $V_T = 22.44$ V. Therefore, we again compare the cyclic performance above, $V_{on} = 25$ V, and below, $V_{on} = 20$ V, the voltage threshold, as shown in Figure 59. Below V_T the contact angle change remains fairly stable, with CAC changing from 13.1 initially to 7.8 after 350 cycles. The ideal L-Y contact angle for 20 V for this system would be 97.4°

(also experimentally confirmed through stepped voltage measurement, not shown), close to the initial value of 97.9° . At 25 V, the drop should theoretically electrowet to 89.9° , with the initial value in Figure 59(b) of 91° . The CAC from 20° rapidly degrades to less than 8° after 56 cycles, reaching no CAC at 106 cycles.

The results above V_T for this system are not as stable as previously observed for aluminum oxide. Over the first 100 cycles slight ongoing decreases for both V_{on} and V_{off} are observed prior to settling. The results still show a fairly reproducible and reliable response, as is expected for polymer layers at this thickness. For the case below V_T , the rapid decrease in CAC (Figure 59(b)) with cycle number follows the same rationale as with the stepped case, the higher leakage current in the tantalum oxide layer leads to quicker reduction in reversible EWOD.

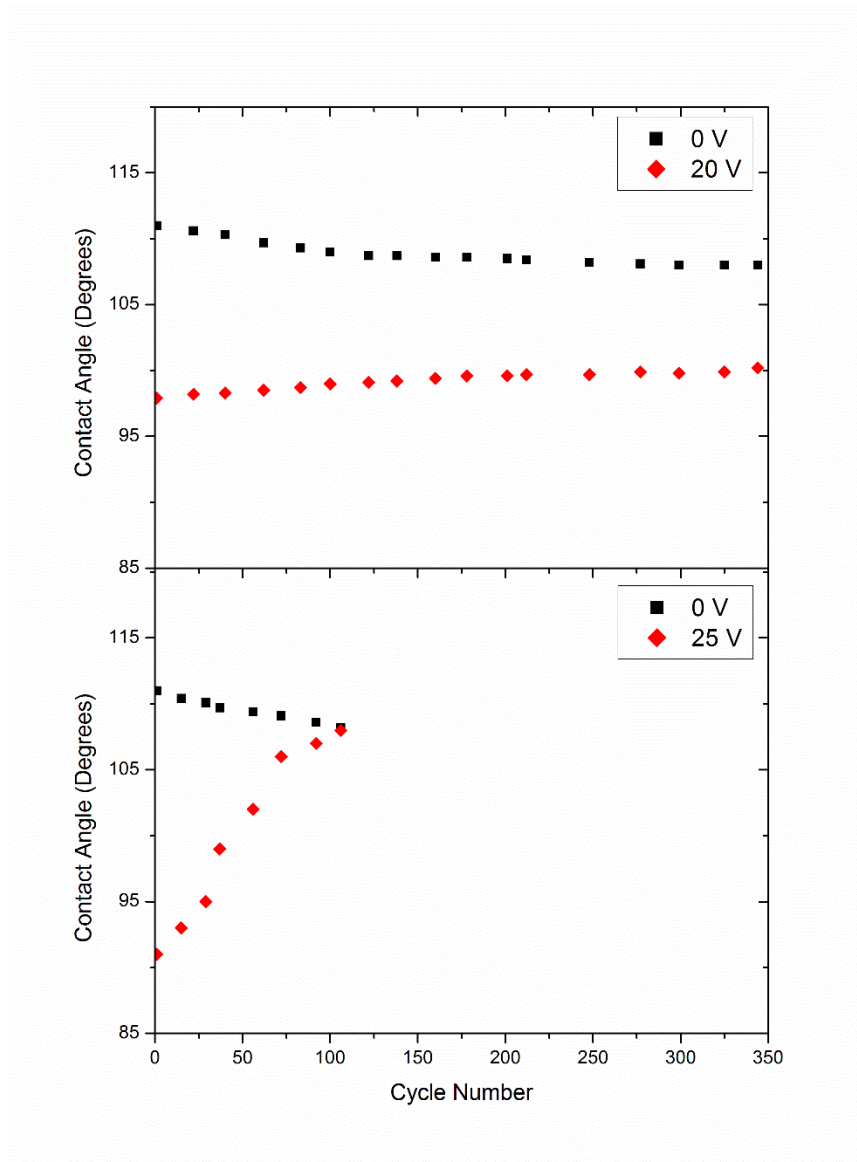


Figure 59: Contact angle vs. Cycle number cyclic measurements are shown on 44nm tantalum oxide /210nm cytop bilayer with applied voltages of (a) $V_{on} = 20\text{ V}$ and (b) $V_{on} = 25\text{ V}$

The resulting CPD of the two cyclic measurements above (25 V) and below (20 V) the $V_T = 22.44\text{ V}$ for the 210 nm Cytop + 44 nm tantalum oxide is shown in Figure 60. From the background of 747mV +/- 80 mV, the $V_{on} = 25\text{ V}$ reaches a peak CPD of 6134mV, comparable to the value observed in Figure 59. However, the number of cycles required to reach zero CAC is only 106 cycles versus over 300 cycles in aluminum oxide.

It is very interesting that the measured CPD for both metal oxides systems at the point of no CAC is so similar. Using the charge density interpretation from the corona charge measurements, the charge density is only given through the potential drop due to the capacitance of the polymer [166], [167]. This suggests that the observed value of charge for zero contact angle change is independent of the underlying oxide layer. In the tantalum oxide system, the value of charge is reached with significantly less cycles, but a similar final value. A complete summary of the data is provided later in this chapter in Table 4.

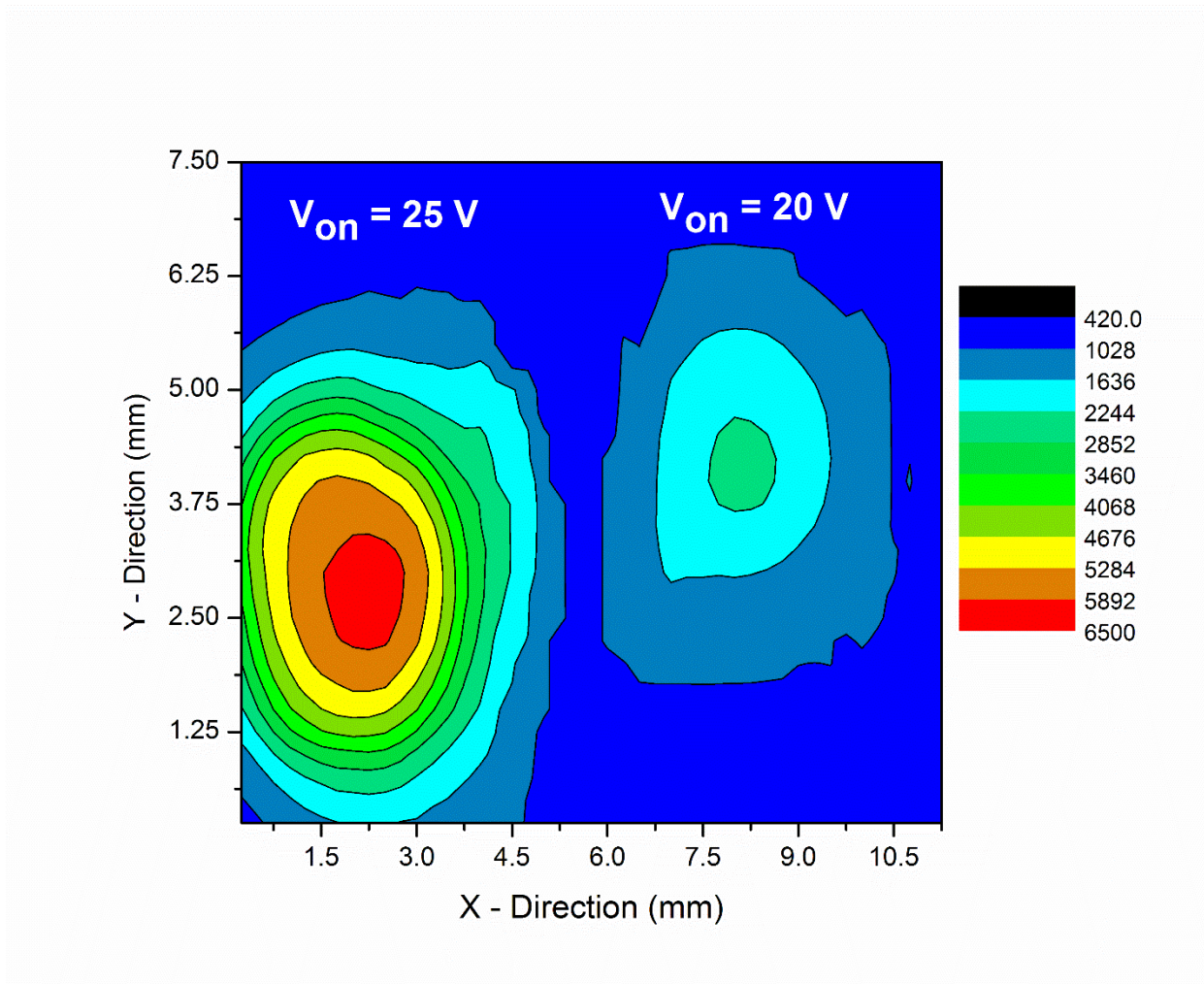


Figure 60: Contact potential difference maps of 44 nm Ta₂O₅ – 21 nm Cytosol surfaces total cycle, numbers indicated in the figure. Colors correspond to mV in legend

6.3 Oxides + ODPa

6.3.1 Static Electrowetting

The static electrowetting of the ODPa monolayers, the formation of which was discussed in Chapter 5, is characterized for both aluminum and tantalum oxide substrates while varying immersion times in 45°C toluene. Figure 61 shows the contact angle and current density vs. applied voltage for 1mM ODPa assembled by immersion for times of 4, 24, 32, and 60 hrs on 44 nm aluminum oxide. The EWOD shows three general regimes similar to what is observed in the polymer system. The current density measured through the EWOD measurements closely follow what is expected for the aluminum oxide substrate, with the SAM layer showing no alteration to the current transients.

The initial electrowetting region doesn't show ideal L-Y EWOD, due to the high hysteresis observed for the different immersion times, as summarized in Chapter 5, Figure 39. The L-Y simulated curve for the modeled system (black line) is offset for all immersion times except for 32 hr to the initial point of appreciable contact angle change. The sample at 4 hr immersion shows several pinned regions where the contact angle doesn't change until jumping resulting in a new pinned state. At low immersion times it is possible that this effect is a combination of hysteresis and discontinuity in the layer. The sample grown at 32 hr immersion time resulted in the highest contact angle (112°) and lowest CAH (15°) during evaluation of the layer formation. Unsurprisingly, this formation condition lead to the best EWOD response given in Figure 61 (c), with 25° CAC by applying only 7 volts.

Contact angle saturation varied between 80-90° for each layer combination, similar to the values observed in polymer system. The CAS behavior was more variable than the Cytop films with pinned angles (4 hr) or a broader response (60 hr). Even the ideal 32 hr immersion time showed a more random variation during CAS, suggesting instability during the voltage stepping measurement.

The final region corresponds to a condition where the voltage exceeds the breakdown field of the aluminum oxide layer. This results in a current flowing through the aluminum oxide surface at high voltage, inducing gas evolution. Simultaneously, the monolayer desorbs from the oxide film, causing an irreversible decrease of the contact angle. Therefore, we see the contact angle plummet rather than the initial receding contact as in the Cytop system. It is interesting that the monolayer remains stable, indicated by the contact angles, even though the voltage drop over the SAM becomes considerable before the breakdown of the oxide film. This is observed throughout all the SAM systems studied in this work.

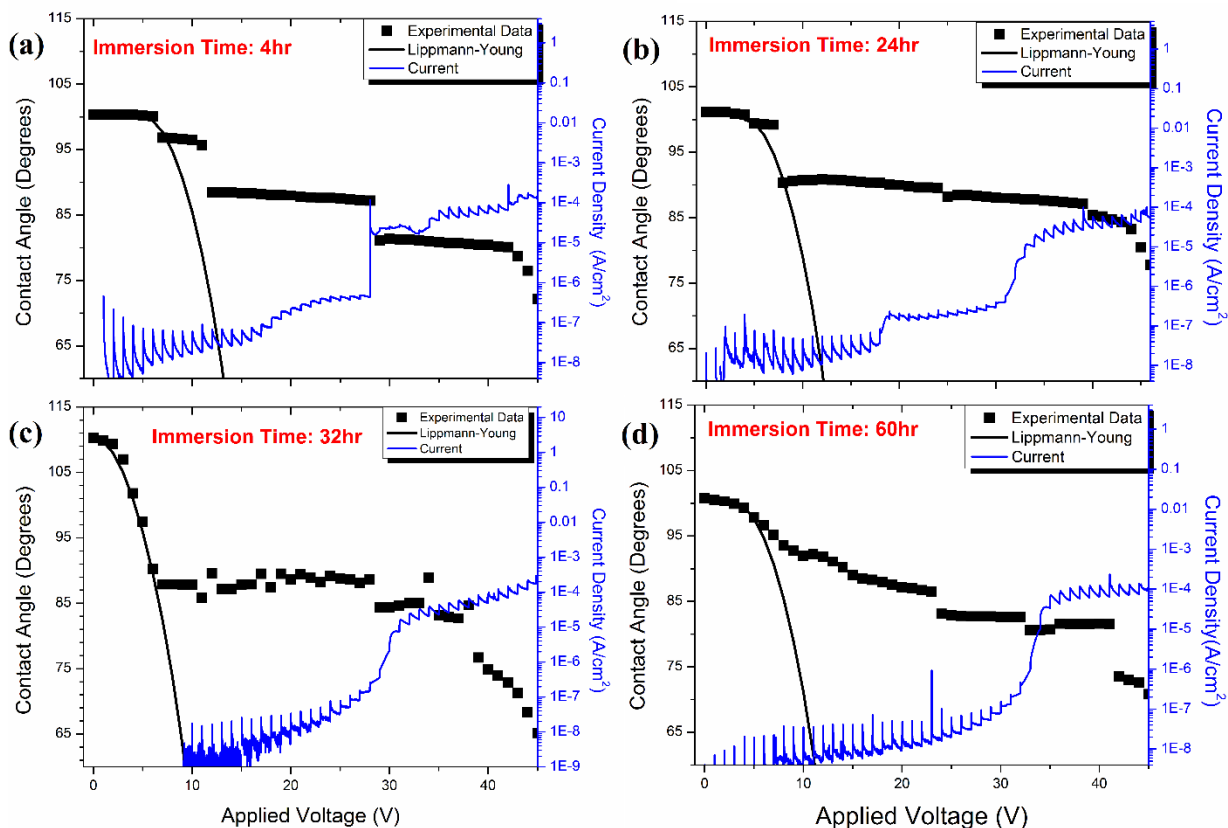


Figure 61: Electrowetting and leakage current measurements of ODPA (formation times in plot) + 44nm aluminum oxide. Contact angle data in black (left axis) with Eq. 6 modeled (black line) and measured current density in blue (right axis)

The SAM formation on tantalum oxide didn't show any appreciable difference in monolayer formation characteristics. The EWOD behavior in Figure 62, shows the contact angle and current density vs. voltage for 1mM ODPA films formed at 24, 32, and 40 hr in 45°C toluene. The same three regime response is seen as was observed in the ODPA-aluminum oxide. The difference between the systems is primarily the higher current density during the measurement due to the tantalum oxide layer and the rapid contact angle vs. voltage change in ideal L-Y response due to the higher dielectric strength. The ideal response occurs again with the formation at 32 hr providing over 20° using 5 V.

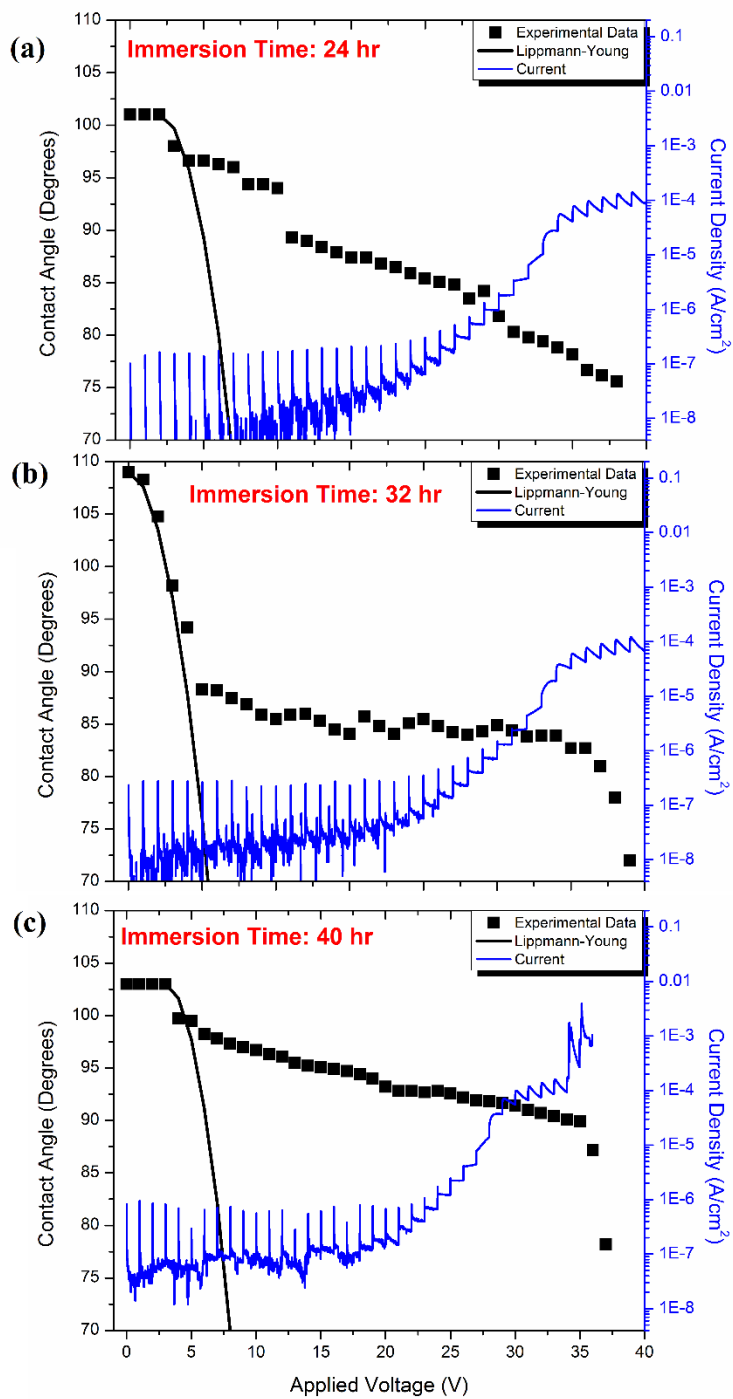


Figure 62: Electrowetting and leakage current measurements of ODPa (formation times in plot) + 44nm tantalum oxide. Contact angle data in black (left axis) with Eq. 6 modeled (black line) and measured current density in blue (right axis)

6.3.2 Cyclic Electrowetting

Cyclic tests on ODPA films grown on both metal oxide substrates showed inconsistent results, with wide variability. Cyclic measurements appeared to modify the surface during measurement making the contact angle change erratic. Figure 63 shows the contact angle vs. cycle number for measurements on 32 hr immersion ODPA on aluminum oxide. This is one of many different measurements on this hydrophobic surface configuration showing erratic results. For example, in Figure 63, the initial cycles go fairly as expected but see lots of fluctuation in the contact angles during $V_{on} = 15$ V ranging between 84° and 92° with the $V_{on} = 0$ V returning $\sim 108^\circ$, but then the contact line became pinned at 20 cycles at an angle of 95° . This remained stable for a couple of cycles until the contact angle dropped to 80.1° returning to 102° when the voltage was switched off again. This measurement is obviously a single run on the surface and this exact response isn't repeated, but the general behavior was consistently observed. Commonly, the contact line became pinned and saw no CAC for several cycles or didn't move again permanently. Imaging with low-voltage SEM and AFM didn't show any obvious changes to the film. With AFM it is difficult to find the edge of the contact line where the alteration would occur, so it cannot conclusively be stated that the layer remains unchanged.

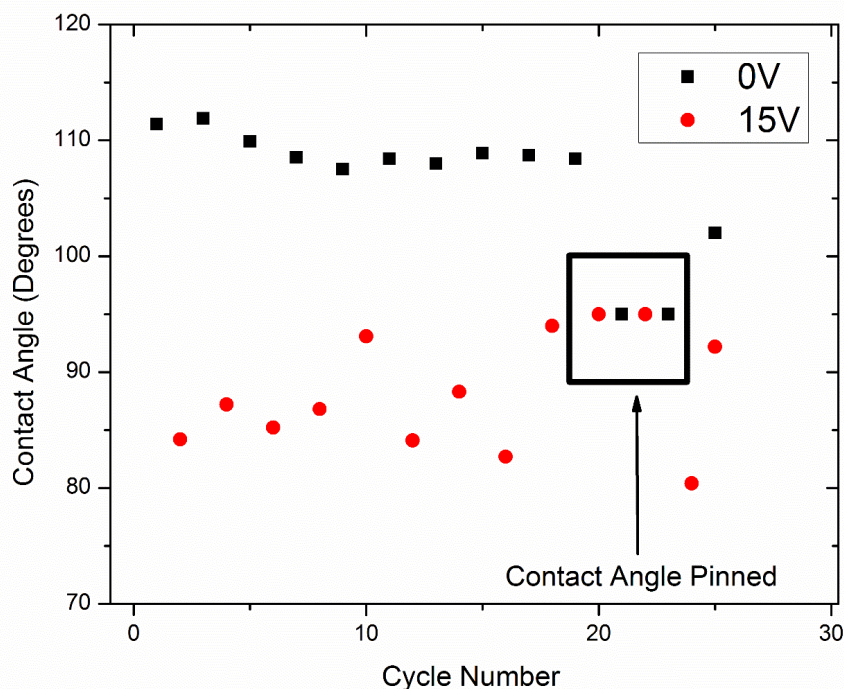


Figure 63: Contact angle vs. Cycle number are shown for cyclic measurements of 44nm tantalum oxide with ODPA monolayer immersed for 32hr in 45°C toluene

6.4 Tantalum Oxide + Silane

Silane SAMs were chosen as potentially providing a more stable surface for cyclic EWOD measurements due to the cross-linked and low hysteresis surfaces. As detailed in Chapter 5, the formation of the layer proved to be quite difficult, with only a couple of static EWOD measurements being in agreement, showing the high hysteresis of the film limiting EWOD performance. However, under the optimal EWOD formation we observe very good performance.

6.4.1 Static Electrowetting

Figure 64 shows the contact angle v. applied voltage dependence for four silane films on 44 nm anodized tantalum oxide. The four SAM formation conditions were specified in Chapter 5.3.2 with XRR patterns in Figure 44 and contact angle hysteresis values in Figure 45. Figure 64(a) shows the silane layer formed in lab air for 30 min. The contact angle change was far from ideal due to the

considerable CAH of 53° , an enormous value. Initially the contact angle slowly decreased from the sessile angle of 105° to 101° until a jump in wetting at 9 V to 90° occurred, with slowly decreasing angles throughout the measurement. Similar behavior was observed in other silane formation in air, with the high hysteresis preventing low voltage EWOD. Figure 64(b-d) shows silane formation under the inert atmosphere conditions (5.3.2) at increasing time in 2% OTS (v/v) toluene solution. The best layer formation was found to be 30 min of immersion time with a CAH of only 11° , a value that is comparable or better than measured on Cytop, with only 2.17 nm thickness and a roughness of 0.702 nm (see Table 2). The corresponding film performance in static EWOD followed the ideal L-Y relationship until saturation at 84° , remaining stable until breakdown in the underlying tantalum oxide film, and eventual layer desorption. The result shows the best overall EWOD performance within this work, over 25° of contact angle change using only 5 V.

Increasing immersion time to 60 and 120 min (Figure 64(c) and (d), respectively) shows inferior performance to the 30 min case. The 60 min case saw good initial contact line motion at the initial voltage steps changing from the sessile angle of 111° to 96.1° with 5 V, but saw a very high angle CAS. Over the remaining voltage range without failure, the contact angle continued to drop a significant amount to 80° . A similar type of response is seen in the 120 min immersion sample with the nearly 20° of increased wetting under 10 V. The response however was highly hysteretic initially, as seen by no change for the first 5 V. This follows the increasing CAH with immersion time in Chp. 5, Figure 45 reaching 25° for the 120 min immersion. With increasing field the contact angle shows an unstable behavior with increasing and decreasing angle reaching a final angle of 86° before failure.

The main issue for the silane electrowetting is to limit the formation of the hydrophobic layer to an ordered monolayer. As seen in Figure 43 (Chapter 5), increasing material is deposited with increasing immersion time, especially by 120 min with AFM images showing 120 nm height differences. Without an inert atmosphere the silane SAMs react readily in solution and white clumps of partially and unreacted SAMs cover the surface. However, under precisely controlled conditions, the layer can form a low hysteretic thin film surface, allowing substantial EWOD at very low voltages as in Figure 64 (b).

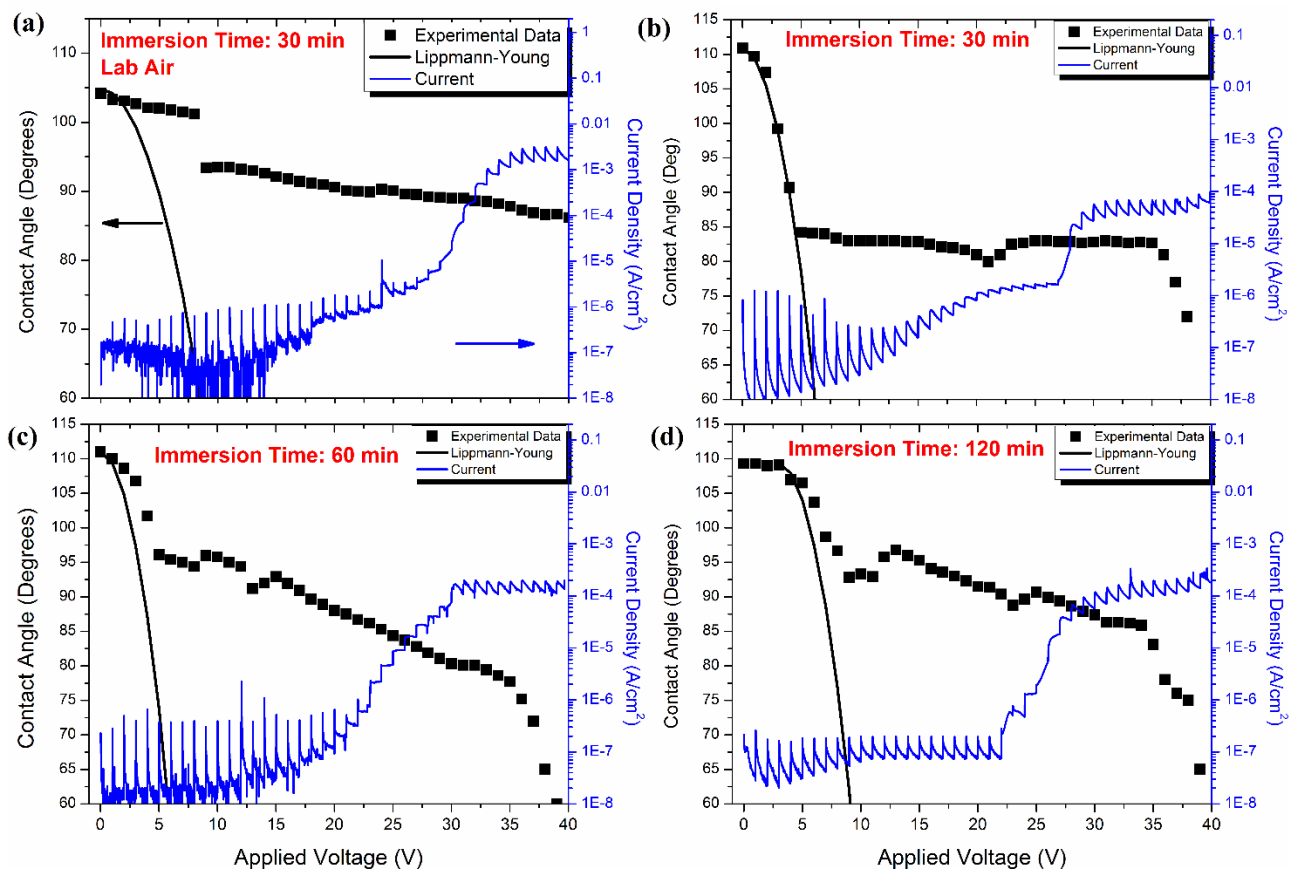


Figure 64: Electrowetting and leakage current measurements of Silane SAMs (formation times in plot) + 44nm tantalum oxide. Contact angle data in black (left axis) with Eq. 6 modeled (black line) and measured current density in blue (right axis)

6.4.2 Cyclic Electrowetting

The cyclic performance of the 30 min silane SAM under Ar on 32 and 44 nm tantalum oxide layers is shown in Figure 65. The performance on both dielectrics show a narrow amount of cycles with reproducible CAC. Both cases showed a very good initial EWOD as expected from the static evaluation (Figure 64(b)) with the initial 110° contact angle decreasing to ~84° with the applied 15 V. A $V_{on} = 15$ V was selected to directly compare the performance to the cyclic Cytop + tantalum oxide in Figure 56. In the Cytop system, the 21 nm Cytop + 32 nm tantalum oxide layer had no CAC after 30 cycles with significant change limited to under 10 cycles. With the SAM on 32 nm tantalum oxide, only 20 cycles could be run before no change could be observed, with substantial EWOD only occurring under 8 V. Similarly, the 44nm tantalum oxide case goes from 50 total cycles in the polymer

with over 20° of contact angle change limited to 30 cycles, while the SAM reached 20 cycles of 20° CAC with no change by 40 cycles.

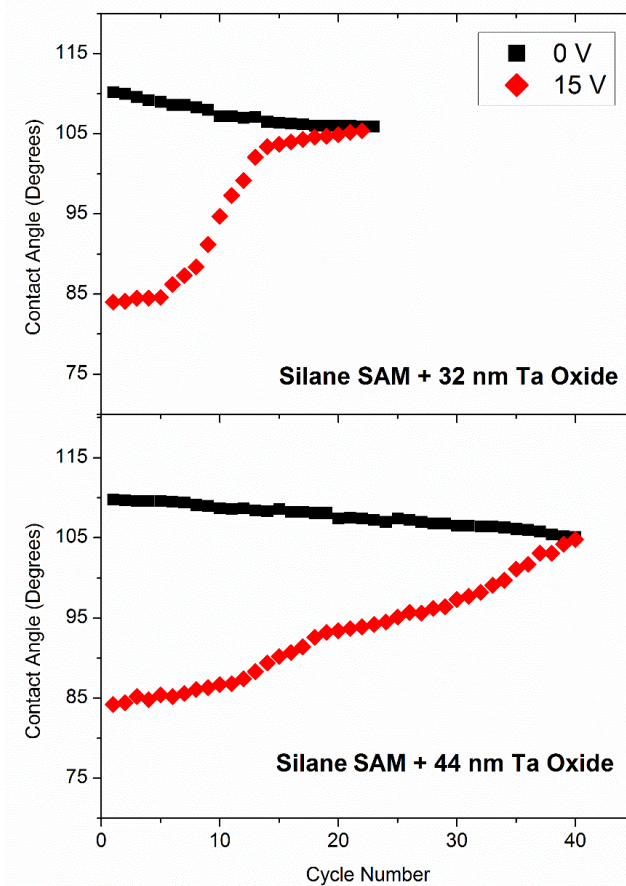


Figure 65: Contact angle vs. Cycle number are shown for cyclic measurements of 32nm and 44nm tantalum oxide with 30 min formation of Silane SAMs 2% (v/v) in toluene under Ar.

SKP scans of the SAM layers for the cyclic conditions for the 32 nm and 44 nm tantalum oxide + 30 min silane, discussed in Figure 65, are given by Figure 66 with (a) 32 nm and (b) 44 nm tantalum oxide layer. Figure 66(a) shows the surface after the 25 cycles without further CAC and Figure 66(b) shows both 20 cycles, where the CAC started to considerably decrease and 40 cycles, where no CAC occurred.

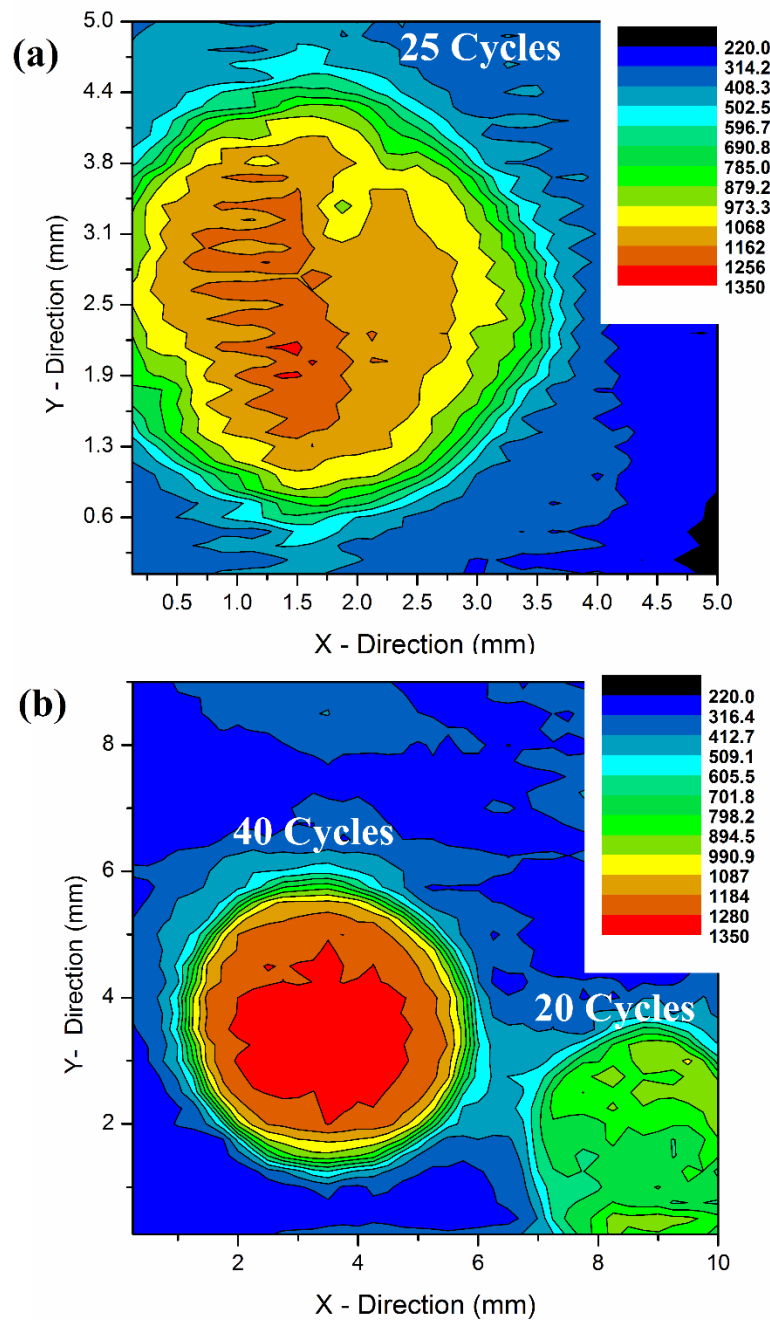


Figure 66: Contact potential difference maps of (a) 32 nm and (b) 44 nm Ta₂O₅ + 30min formation of Silane SAMs 2% (v/v) in toluene under Ar. Total cycle numbers indicated in the figure. Colors correspond to mV in legend

Both plots are shown on the same color scale from the substrate value of average 287 mV, reaching 1338 mV. These CPD values are substantially different from what was observed in the Cytos systems.

The performance for this combination of SAM and oxide shows great promise for large scale contact angle change at very low voltages, but is limited to low voltage use applications due to the limited CAC described in Figure 65. Eq. 1 is reproduced here for the Silane SAM evaluation as the result is both very important and instructive to understanding the cyclic performance.

$$V_T = E_{SAM} \left(t_{SAM} + \frac{\epsilon_{SAM}}{25} 44 \text{ nm} \right)$$

The appropriate values for the tantalum oxide dielectric constant and thickness are inserted into the equation. The E_{SAM} term refers to the breakdown field of the silane, which has been measured in many organic transistor systems. The breakdown field values range from 4 - 9.5 MV/cm, with ~6 MV/cm the most common value for OTS layers [169]–[172]. The breakdown process follows the same conduction mechanisms covered in Chapter 2, using primarily FN or direct tunneling current [173], [174] due to the thickness of the SAM layer, but hopping transport has been observed [175], [176]. The dielectric constant is approximately the same as the oxide layer i.e., ~2 [170]. Using these values, the V_T values range from 4.9 to 11.6 V, all values being below the applied voltage used in the cyclic measurements. The SAM provided the key advantage in LY analysis (Eq. 6) of providing a layer of minimal thickness for EWOD, but is still limited by charge incorporation.

As a result, even though the silane SAM has a considerable higher breakdown field than Cytop, using thicknesses of 2 nm limits the calculated V_T to low applied voltages. This becomes a very important consideration for designing systems to operate at very low voltages. The hydrophobic layer requires a large thickness to mitigate charge incorporation and allow for stable long term performance.

A summary of the material systems and the calculated charge loading through both the trapped charge model (TCM) and the charge estimated through the SKP measurements is given in Table 4.

Oxide	44 nm Aluminum Oxide		44 nm Tantalum Oxide		
Hydrophobic	21 nm Cytop	210 nm Cytop	20 nm Cytop	210 nm Cytop	2.17 nm Silane
TCM	8.94×10^{-4}	2.11×10^{-4}	1.13×10^{-3}	2.18×10^{-4}	4.76×10^{-3}
SKP	1.44×10^{-4}	5.36×10^{-5}	1.75×10^{-4}	4.82×10^{-5}	9.01×10^{-4}

Table 4: Charge density (mC/cm²) calculated for the different material combinations evaluated through the Trapped Charge Model and the Kelvin probe measurements.

The amount of charge that is present to reach zero CAC through the kelvin probe measurement is nearly equivalent for both 21 nm Cytop + 44 nm aluminum oxide and 21 nm Cytop + 44nm tantalum oxide at 1.6×10^{-4} mC/cm². Similarly, the amount of charge in the 210 nm Cytop case on both metal oxide substrates was 5×10^{-5} mC/cm². Having the same measured charge in the SKP system for both cases in combination with the SKP measurement on the bare substrate in Figure 58, shows that the charge is located in the polymer layer.

6.5 Dynamic Electrowetting

The final EWOD characterization performed in this work evaluates electrowetting during dynamic measurements. The measurement allows for a unique investigation as the contact line is dramatically altered from a small drop on the order of a millimeter to a two large planar interfaces (See Chapter 3, Figure 15) with a total > 20 mm wetted width. Along with a significantly larger area, the shape of the contact line now is also changed to a line rather than just the circular drop. EWOD during external surface motion was carried out previously by Nelson. et. al., by monitoring the contact angle in a parallel plate configuration with the bottom plate motion externally controlled. They show that the contact angle change triggered by electrowetting can be drastically altered by the capillary number ($Ca = \mu v / \gamma_k$) with μ the dynamic viscosity and v the immersion speed [177]. The tensiometer allows for direct control of plate movement using a rate of 3 mm/min giving a $Ca = 6.25 \times 10^{-7}$, allowing the measured contact angle change to be solely electrowetting based.

Figure 67, shows both the force vs. immersion depth data (Figure 67 (a)) and the corresponding advancing (black) and receding (red) contact angles (Figure 67(b)) at two voltage intervals with the ideal L-Y curve for both measurements. The contact angle follows the theoretical L-Y dependence for both the advancing and receding angle with the sessile angle offering the only difference in between the curves. Therefore, the measured data show that the hysteresis is clearly independent of the applied field with a value of 14.3° , similar to 12.2° measured without EWOD (Chapter 5, Figure 34). The CAH for this surface didn't show any impact on contact line motion during EWOD measurements with drops, and this measurement didn't show any issue either.

Interestingly, CAS showed unique behavior during the dynamic measurements. In Figure 67, (b), the CAS on Cytop occurs at an angle lower (both advancing and receding) than the majority during individual drop EWOD measurements. During experimentation, the contact line can be visually observed in the tensiometer test system while capturing the force-depth data. At low-voltages the

contact angle is uniform across the contact line, but around the saturation voltage, some regions continue to see increased wetting while others remain unchanged. Therefore, the calculated contact angle shows a smeared response instead of the more typical invariant saturation angle from a drop measurement. The measurement provides an interesting probe into CAS, showing the variation of saturation angle on the same surfaces. This is discussed more in the proposed future work section in Chapter 7.

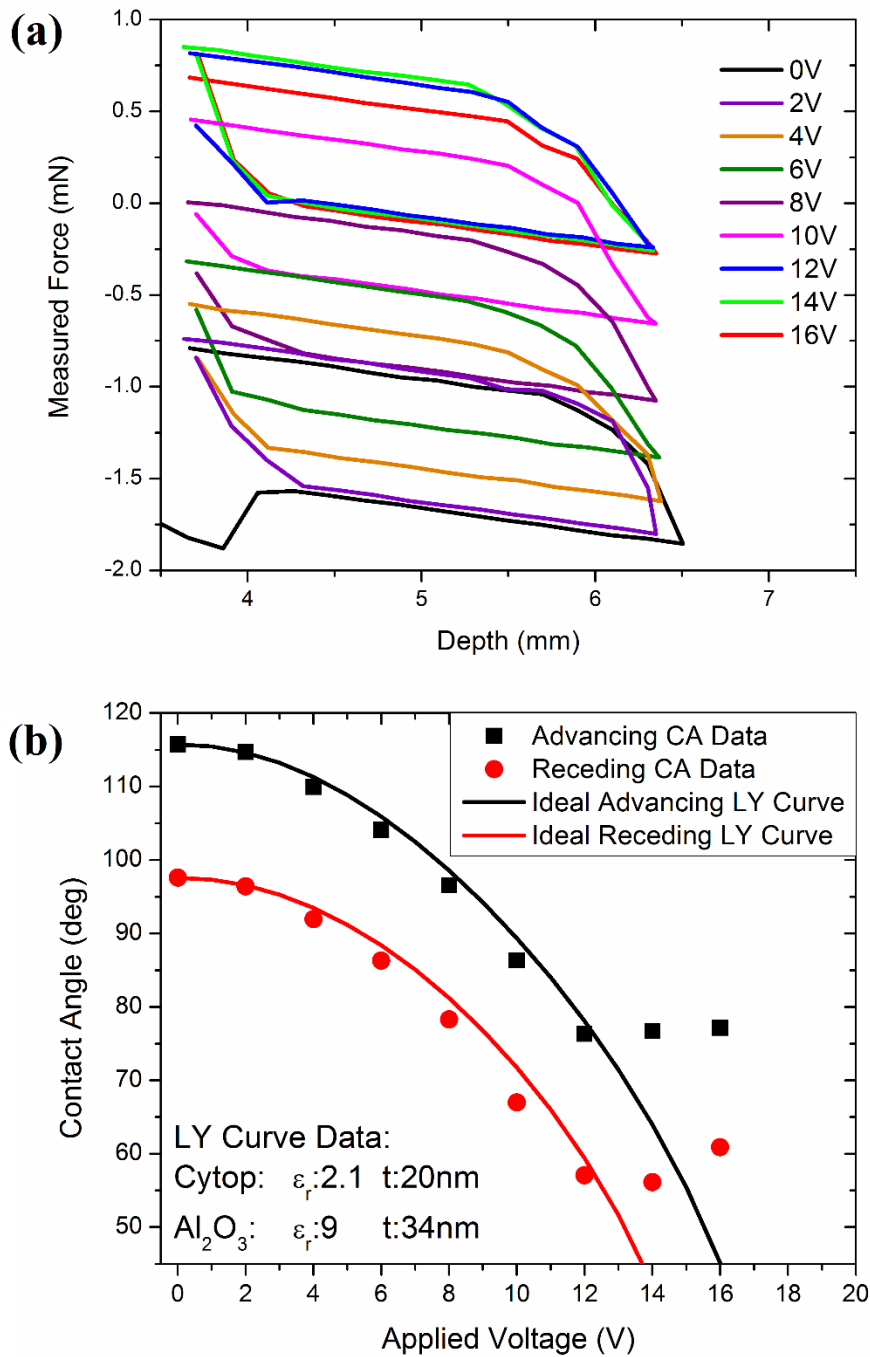


Figure 67: Dynamic EWOD measurements on 21 nm Cytop + 34 nm Aluminum oxide using a .05M electrolyte with (a) the force-depth curves and (b) the resulting advancing and receding contact angles

Chapter 7

Conclusions and Future Work

7.1 Conclusions

The work presented in this dissertation studied electrowetting systems designed to function at low applied voltages. The total change in contact angle is limited to 25-30° from the hydrophobic sessile contact angles of 110° until the limit of contact angle saturation between 80-85°. The primary focus of this effect was to create material bilayers to achieve this increase in wettability at applied voltages under 20 V and below. In order to achieve this result, a simple hydrophobic polymer couldn't be used as is commonly done in initial work within the field; therefore, bilayer materials were studied comprised of a high dielectric strength, highly insulating metal oxide layer and a hydrophobic layer.

The tantalum and aluminum oxides were chosen for this study as the metal oxide layers. Both metal layers allow for simple and controllable oxide formation through the anodization process, providing a highly reproducible oxide film. Aluminum oxide provides an insulating layer with an electronic breakdown field of ~6 MV/cm for the polarity under study with a dielectric constant of 9. The layer has a bandgap of ~8 eV, but presents a large density of donor and acceptor interfacial states, aiding electron conduction processes and eventually causing failure. Tantalum oxide allows for improvement in the dielectric strength with a dielectric constant of 25, but reduces the breakdown field to ~3 MV/cm. The most important characteristic for the electrowetting analysis, was how the oxide functions in conjunction with electrolytic fluids. Both systems under anodic polarity showed electronic dominated leakage current until exceeding the anodization voltage, followed by a small region of oxide growth before gas evolution occurred. Under cathodic polarization, both oxides failed rapidly below 5 V. The analysis establishes that these materials can serve as high dielectric strength layers for electrowetting systems under anodic polarization while remaining at voltages below the anodization voltage.

Hydrophobic layers were studied as the topcoat on the anodically grown metal oxide layer. The goal was to form a layer that could be easily reproducible, with high initial water contact angles that did not hinder the contact line movement during electrowetting testing. Three materials were studied, a commercial fluoropolymer Cytop, and two self-assembled monolayers (SAMs), phosphonic

acid and silane. Cytop layers were formed by spin-coating, allowing for highly reproducible film formation, with precise thickness control and reproducible dielectric properties. The layers consistently gave water contact angles $> 107^\circ$ with an average contact angle hysteresis (CAH) of 12.2° . Reproducible films were limited to thicknesses greater than 20 nm, introducing a limitation to further reduce the electrowetting voltage dependence. SAMs were formed through solution deposition in an organic solvent. A wide variety of solutions conditions were evaluated for reproducible layer formation, with high contact angles and low values of contact angle hysteresis. Phosphonic acid films formed in 1mM octadecylphosphonic acid in 45°C toluene for 32 hr on both metal oxides, showed sessile angles of 112° with a CAH of 15° , meeting the contact angle and hysteresis requirements. Similarly, Silane layers formed with 2 % (v/v) trichloro(octadecyl)silane – toluene under Ar for 30 min, gave a 2.17 nm layer with a sessile angle of 111° and a CAH of only 11° . As a result, all three studied materials showed that they could function as hydrophobic films for electrowetting study.

The electrowetting performance of the combination of metal oxide and bilayer was assessed using a stepped, increasing voltage, up to failure, and cyclic conditions. Three regimes during stepped voltage were observed: ideal Lippmann-Young behavior at low voltages, contact angle saturation, and failure. The initial wetting occurred reversibly until reaching a saturation angle between $82\text{--}89^\circ$. Ultimate failure occurred upon oxide breakdown, leading to the onset of oxygen evolution. Upon failure, the Cytop polymer initially shows contact angle recession from the initial sessile angle, until complete detachment of the polymer. Both SAM layers show decreasing contact angles with the SAMs detaching once the oxide has begun gas evolution. This study successfully showed ideally modeled electrowetting of greater than 25° under applied voltages of 12 V for Cytop, 6 V for phosphonic acid, and 5 V for silane.

Cyclic wetting experiments tested the long term stability of the system, focusing on the contact angle change. Both tantalum and aluminum oxides were studied using a variety of thicknesses of Cytop coatings. Thin (< 50 nm) Cytop layers show decreasing wettability with applied voltage cycles, until no contact angle change occurs. Studying the voltage (V_T), which equates the voltage drop over the polymer to the layer's breakdown strength, elucidates the ability for repeated electrowetting performance. When V_T exceeded the breakdown field, significant charge was injected into the film, minimizing the ability to electrowet, while below V_T highly repeatable electrowetting occurred. The surface potential maps using the Kelvin probe related the decrease in contact angle change to the incorporated charge. Cyclic evaluation of the phosphonic acid SAMs gave very poor reproducibility, with the contact angle commonly getting pinned during the evaluation. Silane SAMs showed rapidly

diminishing contact angle change, similar to the Cytop system, due to the applied voltage exceeding the V_T for the bilayers.

Significant electrowetting is possible at voltages as low as 5 V, for the investigated materials. Anodic metal oxides provide simply fabricated films that provide a large amount of stable electrowetting, limited to one polarity. The properties of the anodic oxide, especially the anodization voltage, control the failure in stepped voltage measurements. For single use systems, such as a disposable one test lab-on-chip device, the required electrowetting can be achieved with only a battery. However, based on cyclic studies, the bilayers will not function for applications requiring many actuations of the fluid. The voltage threshold concept from the trapped charge model [162], predicted the voltages for reproducible contact angle change. The relationship should be used in future design of low-voltage electrowetting systems for repeated use.

7.2 Suggestions for Future Work

The dissertation study was limited to anodic metal oxides as the primarily dielectric layer. As a consequence of the film polarity dependence under electrolytic conditions, measurements could only be run applying a positive voltage to the base metal layer. Using alternative formation methods for the metal oxide films or through modification of the anodized layers, the dielectric could be operated using bipolar voltages. This could potentially reduce the amount of charge in the polymer layer, greatly increasing amount of cyclic electrowetting.

An additionally key feature in the electrowetting system, the electrolytic fluid could possibly greatly change the response of the bilayers. Literature as well as our own studies have shown the dependence of ion size to electrowetting failure [18], [154], [168]; however, these measurements were still limited to aqueous systems. Our initial studies of an ionic liquid, 1-butyl-3-methylimidazolium tetrafluoroborate, showed total electrowetting of 13.1° from a sessile angle of 86.4° to saturation at 73.1° on 21 nm Cytop + 44 nm tantalum oxide. The fluid did however show consistent cyclic contact angle change for 250 cycles, with minimal contact potential difference measured by the Kelvin probe system. Expanding the set of fluids under study could greatly enhance our understanding of the system and provide additional ways to provide reproducible electrowetting.

Significant amount of effort was placed on understanding the electronic and ionic conduction processes occurring in the system, with the stepped current in Chapter 4 clearly fit to known conduction mechanisms. The current during the electrowetting measurements in Chapter 6 however did not fit a simple explanation. Figure 68 shows an examination of the current-time data for 44 nm

aluminum oxide + 56 nm Cytop with a power law fit. The current – time data in (a) is fit through a power law relationship $I = \alpha t^{-\beta}$ described in (b) using a normalized $\log(\text{current})$ vs. $\log(\text{time})$ plot. The slope of each data series in the log-log plot gives the power law exponent (β). This power law exponent is then monitored in (c) at each voltage step during the electrowetting measurement, with an exponential fit of the power law data in red. The increasing slope for the current with each voltage step provides an interesting relationship that may give further insight towards understanding of the underlying processes occurring in the dielectric layers.

The power law exponent shows a clear relationship in the cyclic measurements. Figure 69 shows the current – time transients of the cyclic measurements from V_T analysis in the 210 nm Cytop + 44 nm aluminum oxide system from Chapter 6, Figure 50. The current transients follow a power law dependence for each cycle interval (all data fitted with $R^2 > 0.95$), with Figure 69(a) and (b) revealing the power law exponent over the entirety of the current-time data for 20 V and 25 V cases, respectively. In the case of $V_{\text{on}} = 20$ V (Figure 69(a)), the power law exponent quickly reaches a consistent value between -0.53 and -0.55 for both the on and off state after the initial 15 cycles, with V_{off} remaining below V_{on} . In contrast, $V_{\text{on}} = 25$ V sees the power law exponent values dramatically increase from 100 to 150 cycles followed by a slow decrease to near the initial value of -0.5 at 300 cycles. The alteration in the exponent matches closely to when the V_{on} contact angle saw significant reduction in value, see Figure 50. The current from these measurements can provide more information about the underlying processes.

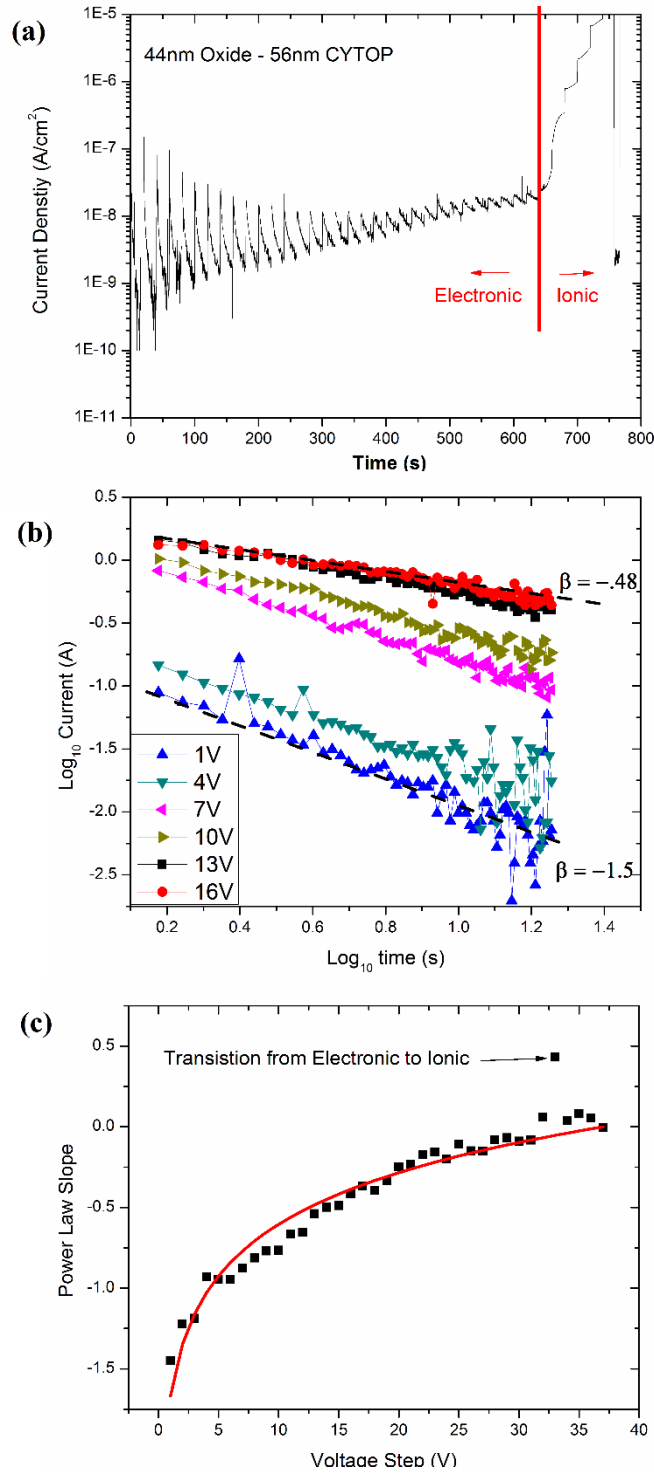


Figure 68: (a) Current Density vs. time for stepped electrowetting measurements on 44 nm aluminum oxide + 56 nm Cytop, (b) current – time data plotted on log-log scale with beta indicating the slope of each voltage step, and (c) the power law exponent at each voltage step, with an exponential fit in red.

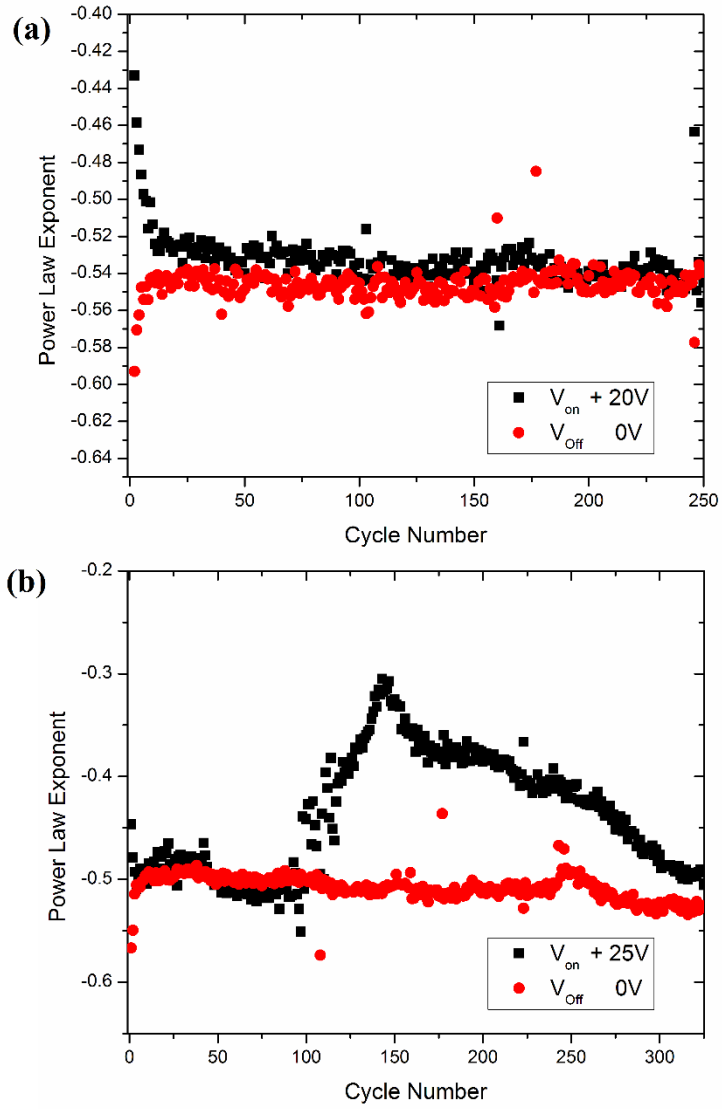


Figure 69: (a) power law exponent for $V_{on} = 20V$ and (b) power law exponent for $V_{on} = 25V$ for 44nm aluminum oxide + 210nm cytop bilayer.

References

- [1] S. K. Cho, H. Moon, and C. Kim, "Creating, transporting, cutting, and merging liquid droplets by electrowetting-based actuation for digital microfluidic circuits," *J. Microelectromechanical Syst.*, vol. 12, no. 1, pp. 70–80, Feb. 2003.
- [2] T. Squires and S. Quake, "Microfluidics: Fluid physics at the nanoliter scale," *Rev. Mod. Phys.*, vol. 77, 2005.
- [3] S. Berry and J. Kedzierski, "New Methods to Transport Fluids in Micro-Sized Devices," *Lincoln Lab. J.*, vol. 17, no. 2, 2008.
- [4] N.-T. Nguyen, X. Huang, and T. K. Chuan, "MEMS-Micropumps: A Review," *J. Fluids Eng.*, vol. 124, no. 2, p. 384, 2002.
- [5] C. Kim, "Micromachines driven by surface tension," in *30th AIAA Fluid Dynamics Conference*, 1999, pp. 1–6.
- [6] J. Lee, H. Moon, J. Fowler, T. Schoellhammer, and C.-J. Kim, "Electrowetting and electrowetting-on-dielectric for microscale liquid handling," *Sensors Actuators A Phys.*, vol. 95, no. 2–3, pp. 259–268, Jan. 2002.
- [7] B. Berge, "Electrocapillarity and Wetting of Insulator Films by Water," *Comptes rendus l'Académie des Sci. Série II, Mécanique, Phys. Chim. Astron.*, vol. 317, no. 2, p. 157, 1993.
- [8] F. Mugele and J.-C. Baret, "Electrowetting: from basics to applications," *J. Phys. Condens. Matter*, vol. 17, no. 28, pp. R705–R774, Jul. 2005.
- [9] J. Feenstra and R. Hayes, "Electrowetting Displays," Technical Report 2009.
- [10] B. Berge and J. Peseux, "Variable focal lens controlled by an external voltage: An application of electrowetting," *Eur. Phys. J. E*, vol. 3, pp. 159–163, 2000.
- [11] R. A. Hayes and B. J. Feenstra, "Video-speed electronic paper based on electrowetting," *Nature*, vol. 425, no. 6956, pp. 383–5, Sep. 2003.
- [12] R. Shamaï, D. Andelman, B. Berge, and R. Hayes, "Water, electricity, and between... On electrowetting and its applications," *Soft Matter*, vol. 4, no. 1, p. 38, 2008.
- [13] H. Moon, S. K. Cho, R. L. Garrell, and C.-J. "Cj" Kim, "Low voltage electrowetting-on-dielectric," *J. Appl. Phys.*, vol. 92, no. 7, p. 4080, 2002.
- [14] E. Seyrat and R. a. Hayes, "Amorphous fluoropolymers as insulators for reversible low-voltage electrowetting," *J. Appl. Phys.*, vol. 90, no. 3, p. 1383, 2001.
- [15] M. Khodayari, J. Carballo, and N. B. Crane, "A material system for reliable low voltage anodic electrowetting," *Mater. Lett.*, vol. 69, pp. 96–99, Feb. 2012.
- [16] B. Koo and C.-J. Kim, "Evaluation of repeated electrowetting on three different fluoropolymer top coatings," *J. Micromechanics Microengineering*, vol. 23, no. 6, p. 067002, Jun. 2013.

- [17] S. Berry, J. Kedzierski, and B. Abedian, "Low voltage electrowetting using thin fluoropolymer films," *J. Colloid Interface Sci.*, vol. 303, no. 2, pp. 517–524, Nov. 2006.
- [18] B. Raj, M. Dhindsa, N. R. Smith, R. Laughlin, and J. Heikenfeld, "Ion and liquid dependent dielectric failure in electrowetting systems.," *Langmuir*, vol. 25, no. 20, pp. 12387–92, Oct. 2009.
- [19] M. Dhindsa, J. Heikenfeld, W. Weekamp, and S. Kuiper, "Electrowetting without electrolysis on self-healing dielectrics.," *Langmuir*, vol. 27, no. 9, pp. 5665–70, May 2011.
- [20] W. Parkes, L. I. Haworth, A. Ross, J. Stevenson, and A. J. Walton, "Room-Temperature Fabrication of Anodic Tantalum Pentoxide for Low-Voltage Electrowetting on Dielectric (EWOD)," *J. Microelectromechanical Syst.*, vol. 17, no. 6, pp. 1481–1488, Dec. 2008.
- [21] T. Krupenkin and J. A. Taylor, "Reverse electrowetting as a new approach to high-power energy harvesting.," *Nat. Commun.*, vol. 2, no. May, p. 448, Jan. 2011.
- [22] J. D. Plummer and P. B. Griffin, "Material and process limits in silicon VLSI technology," *Proc. IEEE*, vol. 89, no. 3, pp. 240–258, Mar. 2001.
- [23] J. Robertson, "High dielectric constant gate oxides for metal oxide Si transistors," *Reports Prog. Phys.*, vol. 69, no. 2, pp. 327–396, Feb. 2006.
- [24] P. G. de Gennes, "Wetting: statics and dynamics," *Rev. Mod. Phys.*, vol. 57, no. 3, pp. 827–863, Jul. 1985.
- [25] D. Bonn, J. Eggers, J. Indekeu, J. Meunier, and E. Rolley, "Wetting and spreading," *Rev. Mod. Phys.*, vol. 81, no. 2, pp. 739–805, May 2009.
- [26] P.-G. de Gennes, F. Brochard-Wyart, and D. Quéré, *Capillarity and Wetting Phenomena*. New York, NY: Springer New York, 2004.
- [27] P. S. Laplace, "Sur l'action capillaire," in *mécanique céleste - supplément au livre X*, 1805, pp. 349–498.
- [28] T. Young, "An Essay on the Cohesion of Fluids," *Philos. Trans. R. Soc. London*, vol. 95, no. 0, pp. 65–87, Jan. 1805.
- [29] G. Lippmann, "Relations entre les phenomenes electriques et capillaires," *Ann. Chim. Phys.*, vol. 5, no. 11, p. 494, 1875.
- [30] H. Helmholtz, "Studien über electrische Grenzschichten," *Ann. der Phys. und Chemie*, vol. 243, no. 7, pp. 337–382, 1879.
- [31] J. Sondag-Huethorst and L. Fokkink, "Potential-dependent wetting of electroactive ferrocene-terminated alkanethiolate monolayers on gold," *Langmuir*, no. 18, pp. 4380–4387, 1994.
- [32] A. J. Bard and L. R. Faulkner, *Electrochemical Methods: Fundamentals and Applications*, 2nd ed. New York, NY: Wiley, 2001.
- [33] J. Buehrle, S. Herminghaus, and F. Mugele, "Interface profiles near three-phase contact lines in electric fields," *Phys. Rev. Lett.*, vol. 91, no. 8, p. 086101, 2003.

- [34] C. Scheid and P. Witomski, "A proof of the invariance of the contact angle in electrowetting," *Math. Comput. Model.*, vol. 49, no. 3–4, pp. 647–665, 2009.
- [35] K. Adamiak, "Capillary and electrostatic limitations to the contact angle in electrowetting-on-dielectric," *Microfluid. Nanofluidics*, vol. 2, no. 6, pp. 471–480, 2006.
- [36] M. Bienia, M. Vallade, C. Quilliet, and F. Mugele, "Electrical-field-induced curvature increase on a drop of conducting liquid," *Europhys. Lett.*, vol. 74, no. 1, pp. 103–109, Apr. 2006.
- [37] T. B. Jones, "On the relationship of dielectrophoresis and electrowetting," *Langmuir*, vol. 18, no. 11, pp. 4437–4443, 2002.
- [38] T. B. Jones, "An electromechanical interpretation of electrowetting," *J. Micromechanics Microengineering*, vol. 15, no. 6, pp. 1184–1187, Jun. 2005.
- [39] M. Vallet, M. Vallade, and B. Berge, "Limiting phenomena for the spreading of water on polymer films by electrowetting," *Eur. Phys. J. B*, vol. 11, no. 4, pp. 583–591, 1999.
- [40] F. Mugele and J. Buehrle, "Equilibrium drop surface profiles in electric fields," *J. Phys. Condens. Matter*, vol. 19, no. 37, p. 375112, Sep. 2007.
- [41] F. Mugele, "Fundamental challenges in electrowetting: from equilibrium shapes to contact angle saturation and drop dynamics," *Soft Matter*, vol. 5, no. 18, p. 3377, 2009.
- [42] A. Güntherschulze and H. Betz, "Die bewegung der ionengitter von isolatoren bei extremen elektrischenfeldstarken," *Z Phys*, no. 92, pp. 367–374, 1934.
- [43] J. W. Schultze and M. M. Lohrengel, "Stability, reactivity and breakdown of passive films. Problems of recent and future research," *Electrochim. Acta*, vol. 45, no. 15–16, pp. 2499–2513, May 2000.
- [44] M. J. Dignam, "The Kinetics of Growth of Oxides," in *Comprehensive Treatise of Electrochemistry*, J. O. Bockris, B. E. Conway, E. Yeager, and R. E. White, Eds. Boston, MA: Springer US, 1981, pp. 247–306.
- [45] M. M. Lohrengel, "Thin anodic oxide layers on aluminium and other valve metals: high field regime," *Mater. Sci. Eng. R Reports*, vol. 11, no. 6, pp. 243–294, Dec. 1993.
- [46] N. Sato and M. Cohen, "The Kinetics of Anodic Oxidation of Iron in Neutral Solution," *J. Electrochem. Soc.*, vol. 111, no. 5, p. 512, 1964.
- [47] N. Cabrera and N. F. Mott, "Theory of the oxidation of metals," *Reports Prog. Phys.*, vol. 12, no. 1, pp. 163–184, Jan. 1949.
- [48] E. J. W. Verwey, "Electrolytic conduction of a solid insulator at high fields The formation of the anodic oxide film on aluminium," *Physica*, vol. 2, no. 1–12, pp. 1059–1063, Jan. 1935.
- [49] J. W. Diggle, T. C. Downie, and C. W. Goulding, "Anodic oxide films on aluminum," *Chem. Rev.*, vol. 69, no. 3, pp. 365–405, Jun. 1969.
- [50] K. Shlmizu, G. E. Thompson, G. C. Wood, and K. Kobayashi, "Structural ordering in annealed anodic oxide films on aluminium," *Philos. Mag. Lett.*, vol. 61, no. 3, pp. 133–137, Mar. 1990.

- [51] J. L. Whitton, "The Measurement of Ionic Mobilities in the Anodic Oxides of Tantalum and Zirconium by a Precision Sectioning Technique," *J. Electrochem. Soc.*, vol. 115, no. 1, p. 58, 1968.
- [52] K. Ozawa and T. Majima, "Anodization behavior of Al, and physical and electrical characterization of its oxide films," *J. Appl. Phys.*, vol. 80, no. 10, p. 5828, 1996.
- [53] J. Lambert, C. Guthmann, C. Ortega, and M. Saint-Jean, "Permanent polarization and charge injection in thin anodic alumina layers studied by electrostatic force microscopy," *J. Appl. Phys.*, vol. 91, no. 11, p. 9161, 2002.
- [54] P. Skeldon, K. Shimizu, G. E. Thompson, and G. C. Wood, "Barrier-type anodic films on aluminium in aqueous borate solutions: 2 - Film compositions by Rutherford backscattering spectroscopy and nuclear reaction methods," *Surf. Interface Anal.*, vol. 5, no. 6, pp. 252–263, Dec. 1983.
- [55] Y. Sasaki, "p-i-n junction in the anodic oxide film of tantalum," *J. Phys. Chem. Solids*, vol. 13, no. 3–4, pp. 177–186, Jun. 1960.
- [56] K. Chari and B. Mathur, "The conduction properties of anodic Al₂O₃ films," *Thin Solid Films*, vol. 75, no. 2, pp. 157–166, Jan. 1981.
- [57] J. H. Stathis, "Percolation models for gate oxide breakdown," *J. Appl. Phys.*, vol. 86, no. 10, p. 5757, 1999.
- [58] S. Lombardo, J. H. Stathis, B. P. Linder, K. L. Pey, F. Palumbo, and C. H. Tung, "Dielectric breakdown mechanisms in gate oxides," *J. Appl. Phys.*, vol. 98, no. 12, p. 121301, 2005.
- [59] N. F. Mott, "Electrons in disordered structures," *Adv. Phys.*, vol. 16, no. 61, pp. 49–144, Jan. 1967.
- [60] J. G. Simmons, "Conduction in thin dielectric films," *J. Phys. D. Appl. Phys.*, vol. 4, no. 5, pp. 613–657, May 1971.
- [61] D. S. Campbell and A. R. Morley, "Electrical conduction in thin metallic, dielectric and metallic-dielectric films," *Reports Prog. Phys.*, vol. 34, no. 1, pp. 283–368, 1971.
- [62] C. D. Child, "Discharge From Hot Cathode," *Phys. Rev. (Series I)*, vol. 32, no. 5, pp. 492–511, May 1911.
- [63] N. F. Mott and R. W. Gurney, *Electronic Processes in Ionic Crystals*. 1948.
- [64] A. Rose, "Space-Charge-Limited Currents in Solids," *Phys. Rev.*, vol. 97, no. 6, pp. 1538–1544, Mar. 1955.
- [65] M. Lampert, "Simplified Theory of Space-Charge-Limited Currents in an Insulator with Traps," *Phys. Rev.*, vol. 103, no. 6, pp. 1648–1656, Sep. 1956.
- [66] K. P. Cheung, "A physics-based, unified gate-oxide breakdown model," in *International Electron Devices Meeting 1999. Technical Digest (Cat. No.99CH36318)*, 2000, vol. 88, no. 9, pp. 719–722.
- [67] J. W. McPherson, R. B. Khamankar, and a. Shanware, "Complementary model for intrinsic time-dependent dielectric breakdown in SiO₂ dielectrics," *J. Appl. Phys.*, vol. 88, no. 9, p.

- 5351, 2000.
- [68] J. McPherson, J.-Y. Kim, a. Shanware, and H. Mogul, “Thermochemical description of dielectric breakdown in high dielectric constant materials,” *Appl. Phys. Lett.*, vol. 82, no. 13, p. 2121, 2003.
- [69] C. Kittel, *Introduction to Solid State Physics*. New York, NY: Wiley, 2004.
- [70] J. W. McPherson, a. Shanware, H. Mogul, and J. Rodriguez, “Trends in the ultimate breakdown strength of high dielectric-constant materials,” *IEEE Trans. Electron Devices*, vol. 50, no. 8, pp. 1771–1778, Aug. 2003.
- [71] K. F. Schuegraf and C. Hu, “Hole injection SiO₂/sub 2/ breakdown model for very low voltage lifetime extrapolation,” *IEEE Trans. Electron Devices*, vol. 41, no. 5, pp. 761–767, May 1994.
- [72] D. J. DiMaria, E. Cartier, and D. Arnold, “Impact ionization, trap creation, degradation, and breakdown in silicon dioxide films on silicon,” *J. Appl. Phys.*, vol. 73, no. 7, p. 3367, 1993.
- [73] J. Suñé and E. Wu, “Hydrogen-Release Mechanisms in the Breakdown of Thin SiO₂ Films,” *Phys. Rev. Lett.*, vol. 92, no. 8, p. 087601, Feb. 2004.
- [74] A. Gibaud and G. Vignaud, “Specular Reflectivity from Smooth and Rough Surfaces,” in *X-ray and Neutron Reflectivity*, Berlin, Heidelberg: Springer Berlin Heidelberg, 2009, pp. 85–131.
- [75] C. Soles, H.-J. Lee, B. Vogt, E. Lin, and W. Wu, “Structure Characterization of Nanoporous Interlevel Dielectric Thin Films with X-ray and Neutron Radiation,” in *Dielectric Films for Advanced Microelectronics*, 2007, pp. 100–117.
- [76] I. D. Baikie and P. J. Estrup, “Low cost PC based scanning Kelvin probe,” *Rev. Sci. Instrum.*, vol. 69, no. 11, p. 3902, 1998.
- [77] Lord Kelvin, “V. Contact electricity of metals,” *Philos. Mag. Ser. 5*, vol. 46, no. 278, pp. 82–120, Jul. 1898.
- [78] H. B. Eral, D. J. C. M. ’t Mannetje, and J. M. Oh, “Contact angle hysteresis: a review of fundamentals and applications,” *Colloid Polym. Sci.*, vol. 291, no. 2, pp. 247–260, Sep. 2012.
- [79] J. B. Bindell, “Scanning Electron Microscopy,” in *Encyclopedia of Materials Characterization*, Elsevier, 1992, pp. 70–84.
- [80] G. Haugstad, *Atomic Force Microscopy: Understanding Basic Modes and Advanced Applications*, 1st ed. Wiley, 2012.
- [81] S. Magonov and M.-H. Whangbo, *Surface Analysis with STM and AFM*. 1996.
- [82] a. Fattah-alhosseini, “Passivity of AISI 321 stainless steel in 0.5M H₂SO₄ solution studied by Mott–Schottky analysis in conjunction with the point defect model,” *Arab. J. Chem.*, pp. 0–6, Mar. 2012.
- [83] K. L. Levine, D. E. Tallman, and G. P. Bierwagen, “Mott–Schottky analysis of aluminium oxide formed in the presence of different mediators on the surface of aluminium alloy 2024-T3,” *J. Mater. Process. Technol.*, vol. 199, no. 1–3, pp. 321–326, Apr. 2008.

- [84] R. De Gryse, "On the Interpretation of Mott-Schottky Plots Determined at Semiconductor/Electrolyte Systems," *J. Electrochem. Soc.*, vol. 122, no. 5, p. 711, 1975.
- [85] M. J. Carmezim, A. M. Simões, M. O. Figueiredo, and M. Da Cunha Belo, "Electrochemical behaviour of thermally treated Cr-oxide films deposited on stainless steel," *Corros. Sci.*, vol. 44, no. 3, pp. 451–465, Mar. 2002.
- [86] S. R. Morrison, *Electrochemistry at Semiconductor and Oxidized Metal Electrodes*, 1st ed. New York, NY: Plenum Press, 1980.
- [87] K. Gelderman, L. Lee, and S. W. Donne, "Flat-Band Potential of a Semiconductor: Using the Mott–Schottky Equation," *J. Chem. Educ.*, vol. 84, no. 4, p. 685, Apr. 2007.
- [88] J. Kolodzey, S. Member, E. A. Chowdhury, T. N. Adam, G. Qui, I. Rau, J. O. Olowolafe, J. S. Suehle, and Y. Chen, "Electrical Conduction and Dielectric Breakdown in Aluminum Oxide Insulators on Silicon," *IEEE Trans. Electron Devices*, vol. 47, no. 1, pp. 121–128, 2000.
- [89] A. Despic and V. P. Parkhutik, "Electrochemistry of Aluminum in Aqueous Solutions and Physics of Its Anodic Oxide," in *Modern Aspects Of Electrochemistry*, No. 20., vol. 38, no. 2, J. Bockris, R. White, and B. Conway, Eds. New York, NY: Plenum Press, 1989, pp. 401–503.
- [90] B. Benfedda, L. Hamadou, N. Benbrahim, A. Kadri, E. Chainet, and F. Charlot, "Electrochemical Impedance Investigation of Anodic Alumina Barrier Layer," *J. Electrochem. Soc.*, vol. 159, no. 8, pp. C372–C381, Jul. 2012.
- [91] N. B. Hakiki, S. Boudin, B. Rondot, and M. Da Cunha Belo, "The electronic structure of passive films formed on stainless steels," *Corros. Sci.*, vol. 37, no. 11, pp. 1809–1822, Nov. 1995.
- [92] Q. Lu, P. Skeldon, G. E. Thompson, D. Masheder, H. Habazaki, and K. Shimizu, "Transport numbers of metal and oxygen species in anodic tantalum," *Corros. Sci.*, vol. 46, no. 11, pp. 2817–2824, Nov. 2004.
- [93] J. J. Randall, W. J. Bernard, and R. R. Wilkinson, "A radiotracer study of the composition and properties of anodic oxide films on tantalum and niobium," *Electrochim. Acta*, vol. 10, no. 2, pp. 183–201, Feb. 1965.
- [94] J. P. S. Pringle, "The Migration of Oxygen during the Anodic Oxidation of Tantalum," *J. Electrochem. Soc.*, vol. 120, no. 10, p. 1391, 1973.
- [95] K. Shimizu, K. Kobayashi, G. E. Thompson, P. Skeldon, and G. C. Wood, "A novel marker approach for the determination of transport numbers during the growth of anodic oxide films on tantalum," *Philos. Mag. A*, vol. 72, no. 5, pp. 1409–1412, Nov. 1995.
- [96] C. Chaneliere, J. L. Autran, R. a. B. Devine, and B. Balland, "Tantalum pentoxide (Ta₂O₅) thin films for advanced dielectric applications," *Mater. Sci. Eng. R Reports*, vol. 22, no. 6, pp. 269–322, 1998.
- [97] C. Wang, L. Fang, G. Zhang, D. M. Zhuang, and M. S. Wu, "I-V characteristics of tantalum oxide film and the effect of defects on its electrical properties," *Thin Solid Films*, vol. 458, no. 1–2, pp. 246–250, 2004.
- [98] G. Sethi, M. Olszta, J. Sloppy, M. W. Horn, E. C. Dickey, and M. T. Lanagan, "Structure and

- dielectric properties of amorphous tantalum pentoxide thin film capacitors,” *2007 Annu. Rep. - Conf. Electr. Insul. Dielectr. Phenom.*, pp. 815–818, 2007.
- [99] G. Morcan, S. S. Ang, W. D. Brown, L. W. Schaper, and T. G. Lenihan, “Characterization of Flexible Thin Film Tantalum Oxide Capacitors,” in *Dielectric Material Integration for Microelectronics*, 1998, pp. 241–252.
- [100] J. Frenkel, “On Pre-Breakdown Phenomena in Insulators and Electronic Semi-Conductors,” *Phys. Rev.*, vol. 54, no. 8, pp. 647–648, Oct. 1938.
- [101] S. Ezhilvalavan and T.-Y. Tseng, “Conduction mechanisms in amorphous and crystalline Ta₂O₅ thin films,” *J. Appl. Phys.*, vol. 83, no. 9, p. 4797, 1998.
- [102] D. M. Smyth, G. a. Shirn, and T. B. Tripp, “Heat-Treatment of Anodic Oxide Films on Tantalum,” *J. Electrochem. Soc.*, vol. 110, no. 12, p. 1264, 1963.
- [103] X. M. Wu, S. R. Soss, E. J. Rymaszewski, and T. M. Lu, “Dielectric constant dependence of Poole-Frenkel potential in tantalum oxide thin films,” *Mater. Chem. Phys.*, vol. 38, no. 3, pp. 297–300, 1994.
- [104] V. Macagno and J. Schultze, “The growth and properties of thin oxide layers on tantalum electrodes,” *J. Electroanal. Chem. Interfacial Electrochem.*, vol. 180, no. 1–2, pp. 157–170, Dec. 1984.
- [105] L. Zhang, “On the Kinetics of Growth of Anodic Oxide Films,” *J. Electrochem. Soc.*, vol. 145, no. 3, p. 898, 1998.
- [106] N. Khalil and J. S. L. Leach, “The anodic oxidation of valve metals—I. Determination of ionic transport numbers by α -spectrometry,” *Electrochim. Acta*, vol. 31, no. 10, pp. 1279–1285, Oct. 1986.
- [107] F. Di Quarto, C. Gentile, S. Piazza, and C. Sunseri, “A photoelectrochemical study on anodic tantalum oxide films,” *Corros. Sci.*, vol. 35, no. 1–4, pp. 801–808, Jan. 1993.
- [108] O. Kerrec, D. Devilliers, H. Groult, and M. Chemla, “Dielectric properties of anodic oxide films on tantalum,” *Electrochim. Acta*, vol. 40, no. 6, pp. 719–724, Apr. 1995.
- [109] Q. Lu, S. Mato, P. Skeldon, G. E. Thompson, and D. Masheder, “Dielectric properties of anodic films formed on sputtering-deposited tantalum in phosphoric acid solution,” *Thin Solid Films*, vol. 429, no. 1–2, pp. 238–242, 2003.
- [110] G. E. Cavigliasso, M. J. Esplandiu, and V. A. Macagno, “Influence of the forming electrolyte on the electrical properties of tantalum and niobium oxide films: an EIS comparative study,” *J. Appl. Electrochem.*, vol. 28, no. 11, pp. 1213–1219, 1998.
- [111] D. Allen, R. Schad, G. Zangari, I. Zana, D. Yang, M. C. Tondra, and D. Wang, “Pinhole decoration in magnetic tunnel junctions,” *J. Vac. Sci. Technol. A Vacuum, Surfaces, Film.*, vol. 18, no. 4, p. 1830, 2000.
- [112] Asahi Glass Co., “CYTOP Technical Bulletin,” Kanagawa, Japan, 2009.
- [113] W. C. Nelson, P. Sen, and C. C. J. Kim, “Dynamic contact angles and hysteresis under electrowetting-on-dielectric,” *Langmuir*, vol. 27, no. 16, pp. 10319–26, Aug. 2011.

- [114] F. Schreiber, "Structure and growth of self-assembling monolayers," *Prog. Surf. Sci.*, vol. 65, no. 5–8, pp. 151–257, Nov. 2000.
- [115] L. Thomsen, B. Watts, D. V. Cotton, and P. C. Dastoor, "Measuring the Tilt Angle of ODTMS Self-Assembled Monolayers on Al Oxide Surfaces," *Synth. Met.*, vol. 154, no. 1–3, pp. 9–12, Sep. 2005.
- [116] L. Thomsen, B. Watts, D. V. Cotton, J. S. Quinton, and P. C. Dastoor, "Adsorption and orientation kinetics of self-assembled films of octadecyltrimethoxysilane on aluminium oxide surfaces," *Surf. Interface Anal.*, vol. 37, no. 5, pp. 472–477, May 2005.
- [117] P. Thissen, M. Valtiner, and G. Grundmeier, "Stability of phosphonic acid self-assembled monolayers on amorphous and single-crystalline aluminum oxide surfaces in aqueous solution," *Langmuir*, vol. 26, no. 1, pp. 156–64, Jan. 2010.
- [118] J. C. Love, L. a Estroff, J. K. Kriebel, R. G. Nuzzo, and G. M. Whitesides, "Self-assembled monolayers of thiolates on metals as a form of nanotechnology," *Chem. Rev.*, vol. 105, no. 4, pp. 1103–69, Apr. 2005.
- [119] D. K. Schwartz, "Mechanisms and kinetics of self-assembled monolayer formation," *Annu. Rev. Phys. Chem.*, vol. 52, pp. 107–37, Jan. 2001.
- [120] J. Sagiv, "Organized monolayers by adsorption. 1. Formation and structure of oleophobic mixed monolayers on solid surfaces," *J. Am. Chem. Soc.*, vol. 102, no. 1, pp. 92–98, Jan. 1980.
- [121] S. Onclin, B. J. Ravoo, and D. N. Reinhoudt, "Engineering silicon oxide surfaces using self-assembled monolayers," *Angew. Chem. Int. Ed. Engl.*, vol. 44, no. 39, pp. 6282–304, Oct. 2005.
- [122] J. T. Woodward and D. K. Schwartz, "In Situ Observation of Self-Assembled Monolayer Growth J. Am. Chem. Soc. 1996, 118, 7861–7862," *J. Am. Chem. Soc.*, vol. 118, no. 44, pp. 10944–10944, Jan. 1996.
- [123] J. T. Woodward, I. Doudevski, H. D. Sikes, and D. K. Schwartz, "Kinetics of Self-Assembled Monolayer Growth Explored via Submonolayer Coverage of Incomplete Films," *J. Phys. Chem. B*, vol. 101, no. 38, pp. 7535–7541, Sep. 1997.
- [124] J. T. Woodward, A. Ulman, and D. K. Schwartz, "Self-Assembled Monolayer Growth of Octadecylphosphonic Acid on Mica," *Langmuir*, vol. 12, no. 15, pp. 3626–3629, Jan. 1996.
- [125] J. T. Woodward and D. K. Schwartz, "Dewetting Modes of Surfactant Solution as a Function of the Spreading Coefficient," *Langmuir*, vol. 13, no. 26, pp. 6873–6876, Dec. 1997.
- [126] J. T. Woodward, H. Gwin, and D. K. Schwartz, "Contact Angles on Surfaces with Mesoscopic Chemical Heterogeneity," *Langmuir*, vol. 16, no. 6, pp. 2957–2961, Mar. 2000.
- [127] I. Doudevski and D. K. Schwartz, "Concentration Dependence of Self-Assembled Monolayer Island Nucleation and Growth," *J. Am. Chem. Soc.*, vol. 123, no. 28, pp. 6867–6872, Jul. 2001.
- [128] E. L. Hanson, J. Schwartz, B. Nickel, N. Koch, and M. F. Danisman, "Bonding Self-Assembled, Compact Organophosphonate Monolayers to the Native Oxide Surface of Silicon," *J. Am. Chem. Soc.*, vol. 125, no. 51, pp. 16074–16080, 2003.
- [129] H. Y. Nie, M. J. Walzak, and N. S. McIntyre, "Bilayer and odd-numbered multilayers of octadecylphosphonic acid formed on a Si substrate studied by atomic force microscopy,"

- Langmuir*, vol. 18, no. 7, pp. 2955–2958, 2002.
- [130] S. P. Pujari, L. Scheres, A. T. M. Marcelis, and H. Zuilhof, “Covalent surface modification of oxide surfaces,” *Angew. Chemie - Int. Ed.*, vol. 53, pp. 6322–6356, 2014.
- [131] I. Doudevski and D. Schwartz, “Dynamic scaling of the submonolayer island size distribution during self-assembled monolayer growth,” *Phys. Rev. B*, vol. 60, no. 1, pp. 14–17, 1999.
- [132] I. Doudevski, W. Hayes, and D. Schwartz, “Submonolayer Island Nucleation and Growth Kinetics during Self-Assembled Monolayer Formation,” *Phys. Rev. Lett.*, vol. 81, no. 22, pp. 4927–4930, 1998.
- [133] E. Balaur, J. Macak, L. Taveira, and P. Schmuki, “Tailoring the wettability of TiO nanotube layers,” *Electrochem. commun.*, vol. 7, no. 10, pp. 1066–1070, Oct. 2005.
- [134] H. Sato, T. Fujii, E. Tsuji, Y. Aoki, K. Shimizu, P. Skeldon, G. E. Thompson, and H. Habazaki, “Observation of self-assembled layers of alkyl phosphonic acid on aluminum using low-voltage scanning electron microscopy and AFM,” *Surf. Interface Anal.*, vol. 45, no. 10, pp. 1441–1445, Oct. 2013.
- [135] A. Khassanov, H.-G. Steinrück, T. Schmaltz, A. Magerl, and M. Halik, “Structural Investigations of Self-Assembled Monolayers for Organic Electronics: Results from X-ray Reflectivity,” *Acc. Chem. Res.*, vol. 48, no. 7, pp. 1901–1908, Jul. 2015.
- [136] W. Chen, A. Y. Fadeev, M. C. Hsieh, D. Öner, J. Youngblood, and T. J. McCarthy, “Ultrahydrophobic and Ultralyophobic Surfaces: Some Comments and Examples,” *Langmuir*, vol. 15, no. 10, pp. 3395–3399, May 1999.
- [137] L. Gao and T. J. McCarthy, “Contact angle hysteresis explained,” *Langmuir*, vol. 22, no. 14, pp. 6234–7, Jul. 2006.
- [138] G. E. Fryxell, S. V. Mattigod, Y. Lin, H. Wu, S. Fiskum, K. Parker, F. Zheng, W. Yantasee, T. S. Zemanian, R. S. Addleman, J. Liu, K. Kemner, S. Kelly, and X. Feng, “Design and synthesis of self-assembled monolayers on mesoporous supports (SAMMS): The importance of ligand posture in functional nanomaterials,” *J. Mater. Chem.*, vol. 17, no. 28, p. 2863, 2007.
- [139] R. Helmy, R. W. Wenslow, and A. Y. Fadeev, “Reaction of Organosilicon Hydrides with Solid Surfaces: An Example of Surface-Catalyzed Self-Assembly,” *J. Am. Chem. Soc.*, vol. 126, no. 24, pp. 7595–7600, Jun. 2004.
- [140] A. Y. Fadeev and T. J. McCarthy, “Self-Assembly Is Not the Only Reaction Possible between Alkyltrichlorosilanes and Surfaces: Monomolecular and Oligomeric Covalently Attached Layers of Dichloro- and Trichloroalkylsilanes on Silicon,” *Langmuir*, vol. 16, no. 18, pp. 7268–7274, Sep. 2000.
- [141] S. Desbief, L. Patrone, D. Goguenheim, D. Guérin, and D. Vuillaume, “Impact of chain length, temperature, and humidity on the growth of long alkyltrichlorosilane self-assembled monolayers,” *Phys. Chem. Chem. Phys.*, vol. 13, no. 7, pp. 2870–9, Feb. 2011.
- [142] J. B. Brzoska, I. Ben Azouz, and F. Rondelez, “Silanization of Solid Substrates: A Step Toward Reproducibility,” *Langmuir*, vol. 10, no. 11, pp. 4367–4373, 1994.
- [143] J. B. Brzoska, N. Shahidzadeh, and F. Rondelez, “Evidence of a transition temperature for

- the optimum deposition of grafted monolayer coatings,” *Nature*, vol. 360, no. 6406, pp. 719–721, Dec. 1992.
- [144] C. Carraro, O. W. Yauw, M. M. Sung, and R. Maboudian, “Observation of Three Growth Mechanisms in Self-Assembled Monolayers,” *J. Phys. Chem. B*, vol. 102, no. 23, pp. 4441–4445, Jun. 1998.
- [145] S. R. Wasserman, G. M. Whitesides, I. M. Tidswell, B. M. Ocko, P. S. Pershan, and J. D. Axe, “The structure of self-assembled monolayers of alkylsiloxanes on silicon: a comparison of results from ellipsometry and low-angle x-ray reflectivity,” *J. Am. Chem. Soc.*, vol. 111, no. 15, pp. 5852–5861, Jul. 1989.
- [146] N. B. Sheller, S. Petrash, M. D. Foster, and V. V Tsukruk, “Atomic Force Microscopy and X-ray Reflectivity Studies of Albumin Adsorbed onto Self-Assembled Monolayers of Hexadecyltrichlorosilane,” *Langmuir*, vol. 14, no. 16, pp. 4535–4544, Aug. 1998.
- [147] R. Bavière, J. Boutet, and Y. Fouillet, “Dynamics of droplet transport induced by electrowetting actuation,” *Microfluid. Nanofluidics*, vol. 4, no. 4, pp. 287–294, Apr. 2008.
- [148] H. J. J. Verheijen and M. W. J. Prins, “Contact angles and wetting velocity measured electrically,” *Rev. Sci. Instrum.*, vol. 70, no. 9, p. 3668, 1999.
- [149] R. Gupta, D. M. Sheth, T. K. Boone, A. B. Sevilla, and J. Fréchet, “Impact of Pinning of the Triple Contact Line on Electrowetting Performance,” *Langmuir*, vol. 27, no. 24, pp. 14923–14929, Dec. 2011.
- [150] H. Ren, R. B. Fair, M. G. Pollack, and E. J. Shaughnessy, “Dynamics of electro-wetting droplet transport,” *Sensors Actuators, B Chem.*, vol. 87, no. 1, pp. 201–206, 2002.
- [151] F. Li and F. Mugele, “How to make sticky surfaces slippery: Contact angle hysteresis in electrowetting with alternating voltage,” *Appl. Phys. Lett.*, vol. 92, no. 24, p. 244108, 2008.
- [152] S. Chevalliot, S. Kuiper, and J. Heikenfeld, “Experimental Validation of the Invariance of Electrowetting Contact Angle Saturation,” *J. Adhes. Sci. Technol.*, vol. 26, no. 12–17, pp. 1909–1930, Jan. 2012.
- [153] B. D. Rabideau and A. E. Ismail, “Mechanisms of hydrogen bond formation between ionic liquids and cellulose and the influence of water content,” *Phys. Chem. Chem. Phys.*, vol. 17, no. 8, pp. 5767–5775, 2015.
- [154] M. Mibus, C. Jensen, X. Hu, C. Knospe, M. L. Reed, and G. Zangari, “Dielectric breakdown and failure of anodic aluminum oxide films for electrowetting systems,” *J. Appl. Phys.*, vol. 114, no. 1, p. 014901, 2013.
- [155] H. J. J. Verheijen and M. W. J. Prins, “Reversible Electrowetting and Trapping of Charge: Model and Experiments,” *Langmuir*, vol. 15, no. 20, pp. 6616–6620, Sep. 1999.
- [156] F. Mugele and S. Herminghaus, “Electrostatic stabilization of fluid microstructures,” *Appl. Phys. Lett.*, vol. 81, no. 12, p. 2303, 2002.
- [157] A. Quinn, R. Sedev, and J. Ralston, “Contact angle saturation in electrowetting,” *J. Phys. Chem. B*, vol. 109, no. 13, pp. 6268–75, Apr. 2005.
- [158] V. Peykov, A. Quinn, and J. Ralston, “Electrowetting: A model for contact-angle saturation,”

- Colloid Polym. Sci.*, vol. 278, no. 8, pp. 789–793, 2000.
- [159] J. Boland, Yuan-Heng Chao, Y. Suzuki, and Y. C. Tai, “Micro electret power generator,” in *The Sixteenth Annual International Conference on Micro Electro Mechanical Systems, 2003. MEMS-03 Kyoto. IEEE*, 2003, pp. 538–541.
- [160] H. Lo and Y.-C. Tai, “Parylene-based electret power generators,” *J. Micromechanics Microengineering*, vol. 18, no. 10, p. 104006, 2008.
- [161] Y. Sakane, Y. Suzuki, and N. Kasagi, “The development of a high-performance perfluorinated polymer electret and its application to micro power generation,” *J. Micromechanics Microengineering*, vol. 18, no. 10, p. 104011, 2008.
- [162] S. Berry, J. Kedzierski, and B. Abedian, “Irreversible Electrowetting on Thin Fluoropolymer Films,” *Langmuir*, vol. 23, no. 24, pp. 12429–12435, Nov. 2007.
- [163] M. K. Kilaru, J. Heikenfeld, G. Lin, and J. E. Mark, “Strong charge trapping and bistable electrowetting on nanocomposite fluoropolymer: BaTi O₃ dielectrics,” *Appl. Phys. Lett.*, vol. 90, no. 2007, pp. 23–25, 2007.
- [164] a. G. Papathanasiou, a. T. Papaioannou, and a. G. Boudouvis, “Illuminating the connection between contact angle saturation and dielectric breakdown in electrowetting through leakage current measurements,” *J. Appl. Phys.*, vol. 103, no. 3, p. 034901, 2008.
- [165] D. K. Schroder, “Surface voltage and surface photovoltage: history, theory and applications,” *Meas. Sci. Technol.*, vol. 12, no. 3, pp. R16–R31, 2001.
- [166] K. R. McIntosh, S. C. Baker-Finch, N. E. Grant, A. F. Thomson, S. Singh, and I. D. Baikie, “Charge Density in Atmospheric Pressure Chemical Vapor Deposition TiO₂ on SiO₂-Passivated Silicon,” *J. Electrochem. Soc.*, vol. 156, no. 11, pp. G190–G195, 2009.
- [167] S. W. Glunz, D. Biro, S. Rein, and W. Warta, “Field-effect passivation of the SiO₂/Si interface,” *J. Appl. Phys.*, vol. 86, no. 1, p. 683, 1999.
- [168] S. Chevalliot, J. Heikenfeld, L. Clapp, A. Milarcik, and S. Vilner, “Analysis of Nonaqueous Electrowetting Fluids for Displays,” *J. Disp. Technol.*, vol. 7, no. 12, pp. 649–656, Dec. 2011.
- [169] J. Zhao and K. Uosaki, “Dielectric properties of organic monolayers directly bonded on silicon probed by current sensing atomic force microscope,” *Appl. Phys. Lett.*, vol. 83, no. 10, pp. 2034–2036, 2003.
- [170] P. Fontaine, D. Goguenheim, D. Deresmes, D. Vuillaume, M. Garet, and F. Rondelez, “Octadecyltrichlorosilane monolayers as ultrathin gate insulating films in metal-insulator-semiconductor devices,” *Appl. Phys. Lett.*, vol. 62, no. 18, pp. 2256–2258, 1993.
- [171] S. A. Dibenedetto, A. Facchetti, M. A. Ratner, and T. J. Marks, “Charge Conduction and Breakdown Mechanisms in Self-Assembled Nanodielectrics,” *J. Am. Chem. Soc.*, vol. 131, no. 20, p. 7158, 2009.
- [172] M. Baklanov, M. Green, and K. Maex, *Dielectric Films for Advances Microelectronics*, 1st ed. Wiley, 2007.
- [173] J. M. Beebe, B. Kim, J. W. Gadzuk, C. D. Frisbie, and J. G. Kushmerick, “Transition from direct tunneling to field emission in metal-molecule-metal junctions,” *Phys. Rev. Lett.*, vol. 97,

no. 2, pp. 1–4, 2006.

- [174] D. K. Aswal, S. Lenfant, D. Guerin, J. V. Yakhmi, and D. Vuillaume, “A Tunnel Current in Self-Assembled Monolayers of 3-Mercaptopropyltrimethoxysilane,” *Small*, vol. 1, no. 7, pp. 725–729, Jul. 2005.
- [175] I.-C. Chen and S. E. Holland, “Electrical Breakdown in Thin Gate and Tunneling Oxides,” *IEEE J. Solid-State Circuits*, vol. 20, no. 1, pp. 333–342, Feb. 1985.
- [176] L. E. Calvet, R. G. Wheeler, and M. A. Reed, “Electron transport measurements of Schottky barrier inhomogeneities,” *Appl. Phys. Lett.*, vol. 80, no. 10, p. 1761, 2002.
- [177] W. C. Nelson, P. Sen, and C.-J. C. J. Kim, “Dynamic contact angles and hysteresis under electrowetting-on-dielectric,” *Langmuir*, vol. 27, no. 16, pp. 10319–26, Aug. 2011.